NNT : 2017SACLS380

THÈSE DE DOCTORAT

de l'Université Paris-Saclay

Preparée à l'Université Paris-Sud au sein du Département de Physique des Particules, Irfu, CEA Saclay

ÉCOLE DOCTORALE N°576
Particules Hadrons Énergie et Noyau : Instrumentation, Image, Cosmos et Simulation (PHENIICS)
Spécialité de doctorat : Physique des particules

Par
Amélia Mafalda Maia Leite

Development of a buffer gas trap for the confinement of positrons and study of positronium production in the GBAR experiment

Thèse soutenue à Saclay, le 27 octobre 2017

Composition du jury :

M.	Daniel Comparat	Directeur de Recherche Université Paris-Sud	Président du jury
M.	Michael Charlton	Professeur Université de Swansea	Rapporteur
Mme	Martina Knoop	Chargée de Recherche Université d'Aix-Marseille	Rapporteur
M.	Paolo Crivelli	Chercheur ETH Zurich	Examinateur
M.	Pierre Vanhove	Ingénieur-chercheur CEA Saclay	Examinateur
M.	Yves Sacquin	Directeur de recherche CEA Saclay	Directeur de thèse
M.	Dirk van der Werf	Professeur Université de Swansea	Co-encadrant de thèse

Pedra Filosofal

Eles não sabem que o sonho
é tela, é cor, é pincel,
base, fuste, capitel,
arco em ogiva, vitral,
pináculo de catedral,
contraponto, sinfonia,
máscara grega, magia,
que é retorta de alquimista,
mapa do mundo distante,
rosa-dos-ventos, Infante,
caravela quinhentista,
que é cabo da Boa Esperança,
ouro, canela, marfim,
florete de espadachim,
bastidor, passo de dança,
Colombina e Arlequim,
passarola voadora,
pára-raios, locomotiva,
barco de proa festiva,
alto-forno, geradora,
cisão do átomo, radar,
ultra-som, televisão,
desembarque em foguetão
na superfície lunar.

Eles não sabem, nem sonham,
que o sonho comanda a vida,
que sempre que um homem sonha
o mundo pula e avança
como bola colorida
entre as mãos de uma criança.

António Gedeão, Movimento Perpétuo

Contents

List of Figures

List of Tables

Part I

The GBAR Endeavour

1 A brief history of antimatter

"A hole, if there were one, would be a new kind of particle, unknown to experimental physics, having the same mass and opposite charge to an electron. We may call such a particle an antielectron."

Paul Dirac

In 1928, Dirac formulated the quantum theory of electrons, which combines quantum theory and special relativity, to describe the behavior of an electron moving at relativistic speeds. This theory includes what is now known as the Dirac equation - a relativistic wave equation [1, 2]. This equation can have positive energy solutions and negative energy solutions. Dirac had the ingenuity of not mathematically eliminating the negative energies. Instead, he hypothesized that all the negative energy solutions in vacuum are occupied by electrons also known as the Dirac sea and any additional electrons cannot occupy negative energy solutions because of Pauli's exclusion principle. When an electron escapes this sea it creates a "hole" that behaves like a positive-energy particle, whose electric charge would be opposite to that of the electron. These "holes" are empty-negative states in which when an electron "falls into", energy is emitted in the form of electromagnetic radiation - the "hole" annihilates with an electron. Later in 1931, Dirac realized the "hole" could be a particle with the same mass as the electron but with opposite charge, to which he called an antielectron [3].

One year later, Carl Anderson discovered the antielectron while photographing cosmic rays in a Wilson Cloud Chamber experiment with a 1.5 Tesla magnetic field [4,5]. Anderson observed the tracks produced by positive particles that could not be due to protons, since their range and curvature in a magnetic field were close to those an electron, implying a mass comparable to the electron but with opposite charge. The observed positive electron was coined a positron. A picture of a positron passing though a lead plate in a Wilson Cloud Chamber can be seen in figure 1.1.

In 1955, the Bevatron experiment detected about sixty antiprotons at Berkeley [6]. In this experiment GeV protons impinged on a copper target producing particles, among them pions and antiprotons. A combination of magnets was employed to select particles by their charge and momentum, which with a time-of-flight method allowed the determination of the mass and charge.

Antihydrogen ($\bar{\mathrm{H}}$) was first observed in 1996 by the PS2010 experiment, at the Low Energy Antiproton Ring (LEAR), at CERN [7]. Initially, they produced a positron by pair production when an antiproton passed through the Coulomb field of a nucleus

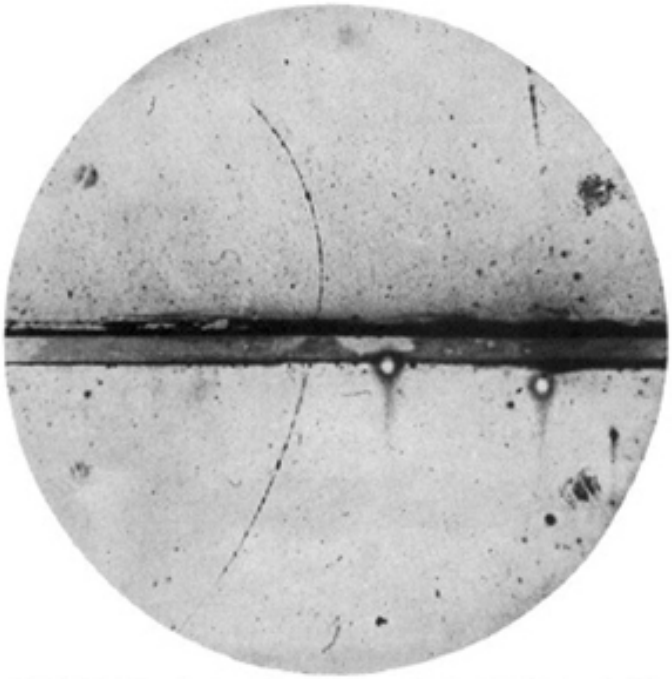

Figure 1.1: A picture of a positron passing through a lead plate in a Wilson Cloud Chamber. A 63 MeV positron, arriving from below, passes through a 6 mm lead plate and emerges as a 23 MeV positron. The length of the latter path is at least 10 times greater than the possible length of a proton path of this curvature. Reprint from [5].

with charge Z, and subsequent capture of the positron by the antiproton, forming antihydrogen.

The CPT (Charge, Parity, and Time reversal) is a fundamental symmetry of the laws of physics and a pillar of Quantum Field Theory. All Lorentz-invariant, local, quantum field theories conserve CPT. This theorem implies that each particle has a corresponding antiparticle with opposite electric charge, magnetic moment, opposite internal quantum numbers, the same total lifetime and inertial mass. According to the Standard Model, in the primordial Universe after the Big Bang, equal amounts of matter and antimatter should have been created. However, if that was the case then all the matter and antimatter would have been annihilated. Yet, today's universe consists of mostly matter which raises the question, what happened to the antimatter? A small violation of CPT could help solve this problem, thus stringent CPT tests are required [8]. The antihydrogen atom is specially suited to a precise CPT test since, according to the CPT theorem, the energy levels of the hydrogen atoms should be identical to those of the antihydrogen atom. Moreover, the hydrogen atom has been extensively studied.

The discovery of the antihydrogen atom and the baryon asymmetry problem encouraged CERN to build the Antiproton Decelerator (AD) [9]. Many experiments (ATRAP [10], ASACUSA [11], ALPHA [12], BASE [13], AEGIS [14] and more recently GBAR [15]) have gathered in the AD hall to look into the mysteries of antimatter. More specifically they perform precision tests of the CPT invariance and the Weak Equivalence Principle. The ATHENA [16] and ATRAP [17] collaborations were the first to

produce and observe about 10^4 cold antihydrogen atoms, using a technique in which cold antiproton and positron plasmas are mixed in nested Penning-Malmberg traps. The ALPHA collaboration has trapped antihydrogen atoms for more than 1000 s [18] and recently observed the $1S$-$2S$ transition in antihydrogen consistent with CPT invariance at a relative precision of about 2×10^{-10} [19]. The most stringent test of CPT invariance with baryonic antimatter was performed by the BASE collaboration, which measured the antiproton-to-proton charge-to-mass ratio with 10^{-12} precision [20].

The positronium atom

The positronium atom (Ps) is a metastable bound state of a positron and an electron and was discovered in 1951 by Martin Deutsch [21]. The first positronium atoms were formed when N_2 gas was exposed to energetic positrons from a β^+ source. A continuous γ-ray spectrum was detected, which is characteristic of the three γ-ray photons decay of positronium (ortho-positronium as will be described below).

The structure of a positronium atom is similar to that of the hydrogen atom, but its reduced mass is half of the electron: $\mu_{Ps} = m_e/2$, implying that the non-relativistic energy levels are roughly half of those of the hydrogen atom:

$$E_n = -\frac{\alpha m_e c^2}{4n^2} \sim -\frac{6.8}{n^2}\, eV\,, \tag{1.1}$$

where n is the principal quantum number, α the fine structure constant and c the speed of light. The positronium atom, in the ground state, can exist in two spin states $S = 0$ and $S = 1$. The first state is a singlet state in which the spins of the positron and electron are anti-parallel. It is denominated as para-positronium (pPs) and has a short lifetime of 125 ps in vacuum. The second state is a triplet state with parallel spins. This state is called ortho-positronium and has a longer lifetime in vacuum of 142 ns. Para-positronium decays predominantly into two γ-rays which are emitted back-to-back with 511 keV energy. The ortho-positronium atom decay preferentially into three coplanar γ-rays. Ground-state positronium has 1/4 probability to be para-positronium and a 3/4 probability to be ortho-positronium.

2 Gravitational Behaviour of Antihydrogen at Rest

"No amount of experimentation can ever prove me right;
a single experiment can prove me wrong."
Albert Einstein

Contents

The Weak Equivalence Principle (WEP) states that the trajectory of a particle is independent of its composition and internal structure, when submitted to a gravitational force. According to Newton's gravitational law, the strength of the gravitational force exerted on a body by some given gravitational field is proportional to the mass of that body, the gravitational mass m_g, via

$$F_g = \frac{GM}{r^2} m_g = m_g g \,. \tag{2.1}$$

F_g is the gravitational force a body with mass M exerts on a second body with mass m_g, $G = 6.674{\times}10^{-11}\,\mathrm{m^3 kg^{-1} s^{-2}}$ is the gravitational constant and r is the distance between the two bodies. Moreover, the resistance to the motion in Newton's second law of mechanics, $F = m_i\, a$, the inertial mass m_i is also the mass of the body. The "equivalence" refers to the fact that a uniform gravitational field is equivalent to a constant acceleration. Thus, a body falling in a gravitational field feels an acceleration $a = g$ that corresponds to the gravitational acceleration, hence the WEP implies that the inertial mass is equivalent to the gravitational mass: $m_g = m_i$.

This fundamental principle has never been directly accurately tested with antimatter, even though it is a cornerstone of General Relativity. There are strong arguments against antigravity, in which matter and antimatter repel each other [22].

Nonetheless, any significant difference between the gravitational acceleration of matter and antimatter would change considerably our understanding of the Universe. The need to introduce dark energy and dark matter to reconcile General Relativity with astrophysical observations may be a hint that our understanding of gravitation is incomplete. In addition, the absence of primordial antimatter in the observable Universe is not understood, hence a different behavior of antimatter under gravity may help solving this puzzle. Finally, from the point of view of experimental physics, the WEP test with antimatter is, in principle, experimentally feasible, thus it should be performed.

The test of WEP with antimatter charged particles was proven to be too great a challenge to undertake; see [23] for an extensive list of experimental problems. Charged particles are susceptible to stray electric and magnetic fields that easily dominate the weak nature of gravitational interactions. Antihydrogen is then a better candidate, not only for being neutral, but also because its matter counterpart has been extensively studied [24], hence precise comparisons could be envisioned. Another candidate is positronium, though its short lifetime poses some experimental difficulties. Moreover, it is composed of both of matter and antimatter, hence it is not a straightforward WEP test. Cassidy *et al.* are tackling the short lifetime problem by exciting it to Rydberg-Stark states [25], which also allows for electrostatic guidance and manipulation of a positronium beam. A different approach is being attempted by Crivelli *et al.*, who intend to measure the gravitational redshift of the 1s-2s transition frequency in positronium [26]. Finally, a WEP test with muonium, the exotic atom composed of an antimuon and an electron, is also being considered [27].

2.1 The GBAR experiment

GBAR (Gravitational Behaviour of Antihydrogen at Rest) is an original experiment that aims to measure the free fall acceleration of neutral antihydrogen atoms in the terrestrial gravitational field, with 1% precision in a first phase [15]. With the present technology the distance traveled by the anti-atoms can be known with high precision (to a few tens of micrometers), as well as the time of flight (to a few nanoseconds using scintillation detectors). The temperature of the antihydrogen atoms, given by the distribution of the initial velocities, is then the main source of error in this experiment. Therefore, to reduce the uncertainty of the initial velocity ultra-cold $\bar{\mathrm{H}}$ are required.

Although, antihydrogen atoms can be Doppler cooled, the minimum attainable temperature is in the millikelvin range [28], which is not enough for the GBAR endeavor. Evaporative cooling could bring the temperature down to a few microkelvin, but the need for high $\bar{\mathrm{H}}$ densities renders this technique unsuitable. J. Walz and T. Hänsch [29] proposed that $\bar{\mathrm{H}}^+$ ions, a bound system of one antiproton and two positrons, can be cooled to microkelvin temperatures, corresponding to velocities of m/s. The advantage of using $\bar{\mathrm{H}}^+$ ions is that these can be sympathetically cooled with matter ions, while the Coulomb repulsion prevents their annihilation. After being cooled, the positron in excess can be photodetached to observe the free fall of the neutral anti-atom.

The milestones required to realize the gravitation experiment can be summarized as follows, and each one will be described in more detail in the following sections:

1. **Production of an intense flux of fast positrons** from the interactions on a thin tungsten target of a 10 MeV electron beam produced by a small linear accelerator.

2. **Moderation of the positrons** down to a few eV by a tungsten target, forming a beam with a flux of $3\times10^8\,e^+/s$.

3. **Positron trapping** using a buffer gas trap.

4. **Accumulation of the positrons** inside a high magnetic field Penning-Malmberg trap and formation of a dense positron plasma with 10^{10} positrons.

5. **Positronium production**: the positrons are bunched and focused into a cavity coated with a porous silica to form a dense ortho-positronium cloud.

6. **Excitation of the positronium atoms** to gain a large factor on the cross section for the production of ions.

7. $\bar{\mathbf{H}}^+$ **production**: the interaction of positronium atoms with the very low energy antiproton beam extracted from the Antiproton Decelerator (AD), followed by the ELENA - the Extremely Low Energy Antiproton ring, produces antihydrogen atoms and ions.

8. **Ion capture and cooling** to $10\,\mu$K.

9. $\bar{\mathbf{g}}$ **measurement**: photodetachment of the excess positron and measurement of the free fall of the antihydrogen atom.

2.1.1 $\bar{H}^+$ production and the ANTION project

Two ingredients are essential to produce $\bar{H}^+$ ions: antiprotons and positronium atoms, and two reactions: antihydrogen production, which then in combination with another positronium atom generates $\bar{H}^+$. While the radiative capture of a positron by an antiproton can produce antihydrogen atoms, Humberston *et al.* [30] proved that the cross section of antiproton collisions with positronium can be five orders of magnitude higher. For that reason GBAR will use the following two step reactions

$$\bar{p} + Ps^* \rightarrow \bar{H}^* + e^- \quad (Hbar) \tag{2.2}$$

$$\bar{H}^* + Ps^* \rightarrow \bar{H}^+ + e^- \quad (Hbar+)\,, \tag{2.3}$$

where $\bar{p}$ stands for antiproton, Ps for positronium and $\bar{H}$ for antihydrogen. The star denotes the possible excitation of the positronium atom, or that of the antihydrogen atom. As stated in the previous chapter, the para-positronium lifetime is too short to be of use, thus henceforth when positronium atoms are mentioned, it refers to ortho-positronium.

The ANTION project is a subproject of the GBAR endeavor that aims to produce and study, for the first time, the antihydrogen ion formed according to these two

reactions. Nevertheless, the first phase of the project involves the measurement of the cross section of the matter counter part of reactions 2.2 and 2.3, namely the charge exchange reaction

$$\mathrm{p} + \mathrm{Ps}^* \rightarrow \mathrm{H}^* + \mathrm{e}^+ \quad (H)\,, \tag{2.4}$$

and the four-body reaction

$$\mathrm{H}^* + \mathrm{Ps}^* \rightarrow \mathrm{H}^- + \mathrm{e}^+ \quad (H\text{-}). \tag{2.5}$$

Herein reactions 2.2, 2.3, 2.4 and 2.5 will be denoted by *Hbar*, *Hbar+*, *H* and *H-*, respectively. Since two positronium atoms are required to form either H^- or $\bar{\mathrm{H}}^+$, the positronium cloud should be very dense. To confine the positronium atoms, the adopted target geometry is a cavity in which one wall is coated with mesoporous SiO_2 that functions as a positron-positronium converter, and the other walls, made of silica, reflect the positronium atoms.

The positrons provided by a linear accelerator will be trapped by a buffer gas trap, built during this thesis and described in Chapter 4, and transfered to a 5T magnetic field multi-ring Penning-Malmberg trap, where they will be accumulated. This trap contains 27 cylindrical electrodes and, due to its ultra-high vacuum conditions, is able to contain a plasma of 10^{10} electrons during approximately 10^4 s [31]. A description of this trap can be found in [32] and [33]. A $\sim 10^{10}$ positron plasma is required to obtain a dense positronium cloud of 10^{12} Ps/cm^3. Once enough positrons are accumulated, a bright positron beam can be formed and accelerated to 4 keV by an elevator, and focused by a set of Einzel lenses into the reaction cavity.

For the matter cross section measurements, a proton gun consisting of a Penning-discharge ion source fed with gaseous hydrogen, will provide microampere-intensity beams. Sets of steering plates and Einzel lenses steer and focus the proton beam into the positronium cloud target.

Currently, CERN is the only facility in the world able to provide low energy antiprotons to experiments. The Antiproton Decelerator (AD) facility supplies intense antiproton pulses with 5 MeV energy. In a number of experiments, a degrader foil is used to reduce the beam energy so that the antiprotons can be accumulated in a Penning-Malmberg trap. Since this method is very inefficient (99.99% of the antiprotons are lost in the process), CERN is constructing a new synchrotron to further decelerate antiprotons to 100 keV - the Extra Low ENergy Antiproton (ELENA) ring. ELENA is expected to deliver antiproton bunches every 110 s containing $\sim 4\times10^6$ $\bar{\mathrm{p}}$ [34].

The antiproton beam provided by ELENA is still too energetic to yield a reasonable amount of $\bar{\mathrm{H}}^+$, hence an additional decelerator will be used to slow down the antiproton beam to 1-20 keV energy. This decelerator is based on electrostatic optics coupled to a pulsed drift tube akin to the one used by ISOLDE at CERN for heavy ions [35]. Briefly, the antiproton beam enters a series of cylindrical electrodes, and in between them lies a 300 mm drift tube that is pulsed from -99 kV to ground while the antiproton beam is inside. This action decelerates the antiprotons.

The values of the cross sections should be compared to the theoretically predicted by GBAR collaborators using a perturbative theory - Continuum Distorted Wave - Final State (CDW-FS). Their work is described in depth in [36,37]. Comini *et al.* show that

the production of $\bar{H}$ atoms is optimal around 6 keV antiproton impact energy. They also state that the production rate can be enhanced by exciting the positronium atoms. $\bar{H}^+$ production is reported to be enhanced at low antiproton energies, and furthermore when the positronium is excited to the $2p$ state and the antiprotons have 1 keV to 2 keV impact energy. However, this state is short-lived (3.2 ns compared to 31 ns in the $3d$ state), posing strong constraints on the laser apparatus. The $3d$ excitation is then suggested over p states. Figure 2.1 shows a comparison of the global $\bar{H}^+$ production cross sections between 100% of Ps($1s$), 30% of Ps($2p$) and 50% of Ps($3d$). For these results it is assumed that 20% of all the antihydrogen atoms produced are in the ground state and that only these contribute to the $\bar{H}^+$ formation. Finally, an important finding reported is that only ground state antihydrogen has sufficiently large cross section to produce $\bar{H}^+$ ions, yet not many are produced in the *Hbar* reaction. For that reason, the excited antihydrogen should undergo radiative relaxation to the ground state before the *Hbar+* reaction occurs. This imposes constraints on the geometry of the reaction cavity given that it should be small enough to form a dense positronium cloud, and at the same time allow the relaxation of hydrogen before colliding with another positronium atom.

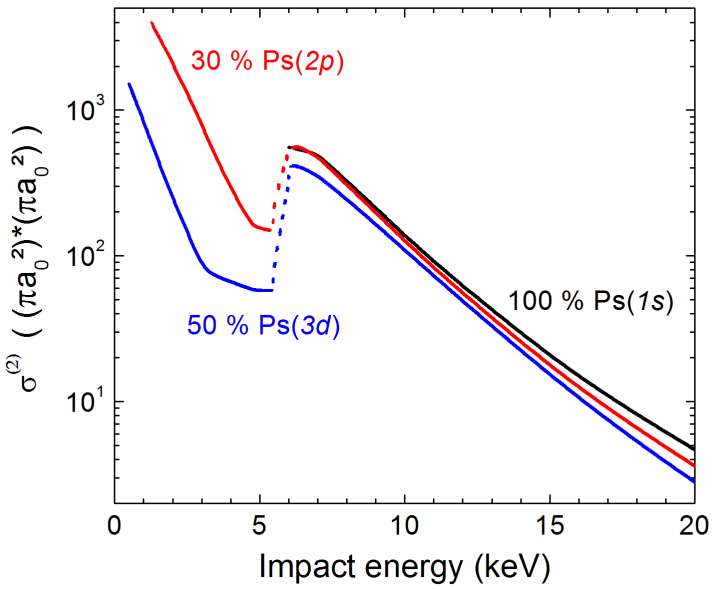

Figure 2.1: Comparison of the global $\bar{H}^+$ production cross sections for different positronium excitation levels. For these results, it was (arbitrarily) assumed that 20% of all the antihydrogen produced were in the ground state for the second reaction, and that only these contributed to the $\bar{H}^+$ formation. Courtesy of P. Comini.

Simulations to evaluate the production rate of H, H^-, $\bar{H}$ and $\bar{H}^+$ for several parameters including the cavity geometry, (anti)proton and positron beam, as well as the excitation laser were performed by the same authors [36]. They propose the use of a 1 mm^2 by 20 mm long cavity for the antimatter cross section measurements with

positronium excitation. This choice takes into account the positronium density and the excited positronium population with time. Comini *et al.* report that at least one $\bar{H}^+$ ion can be produced every two antiproton pulses, and more can be formed at low antiproton energies with the excitation of positronium, if the antiproton transmission through the cavity is improved.

Recently, Rawlins *et al.* [38, 39] computed the cross section of the *Hbar* reaction using the two-center convergent close-coupling (CCC) method. They report enhanced ground state $\bar{H}$ production rates for low $\bar{p}$ energies, when positronium is excited to the states with principal quantum number n = 3. In addition, they suggest that the production rate of the *Hbar+* reaction should be recomputed in the low energy range, if one is to take advantage of the increase in ground state antihydrogen production that a low energy antiproton beam can offer. Yet, this can only be achieved experimentally if a trap is used to cool down the $\bar{p}$.

The laser apparatus for the positronium excitation to the $3d$ state has been developed by collaborators. The $1s$ to $3d$ transition will be executed via a Doppler free two-photon transition with two counter-propagating laser beams of 410 nm. See reference [36] for an in-depth description of this laser apparatus. The $2p$ excitation laser, corresponding to a one-photon transition at 243 nm, is also being assembled by the same collaborators.

In 1997, Merrison *et al.* reported on the production of hydrogen using the charge conjugate reaction $p + Ps \rightarrow H + e^+$ [40]. In this experiment a proton beam with energy in the range 11-16 keV collided with a slow positronium target. The free positrons resulting from this reaction were detected by an electron multiplier array and a scintillation detector (NaI) in coincidence. Heated thin silver foil was employed to produce ortho-positronium with about 3.1% efficiency. The protons were generated by a radio frequency hydrogen discharge reaction, and their current was measured by a Faraday cup. The number of registered coincidence events was 211 ± 46 and the measured cross sections were $\sigma_H = 26(\pm 9)\times 10^{-16}\,\mathrm{cm}^2$, $7.8(\pm 2.3)\times 10^{-16}\,\mathrm{cm}^2$ and $7.6(\pm 4.4)\times 10^{-16}\,\mathrm{cm}^2$ for proton impact energies of 11.3, 13.3 and 15.8 keV, respectively. Figure 2.2 shows the results of Merrison *et al.* along with the predicted cross sections from three different models.

Unlike Merrison *et al.* who detected the positrons resulting from the reaction, the ANTION project intends to directly detect the (anti)hydrogen ions and atoms using microchannel plate detectors (see Chapter 4 for a description of this detector). The (anti)hydrogen ions and atoms will follow the same trajectory as the original antiproton beam. An electrostatic device will be used to separate the neutral particles from the charged particles.

Besides the number of (anti)atoms or ions produced in these reactions, it is crucial to know the time and spatial distributions of the ortho-positronium density inside the cavity, as well as those of the (anti)proton pulse. The density will be inferred by combining the information of scintillation detectors, which will monitor the decay of the positronium atoms, with a detailed GEANT4 [41] simulation of the positronium and proton distribution inside the cavity. At CERN, the detection system will be complemented with micromegas detectors [42] - a particle tracker, to detect the annihilation of the antiprotons in $\bar{H}$ and $\bar{H}^+$.

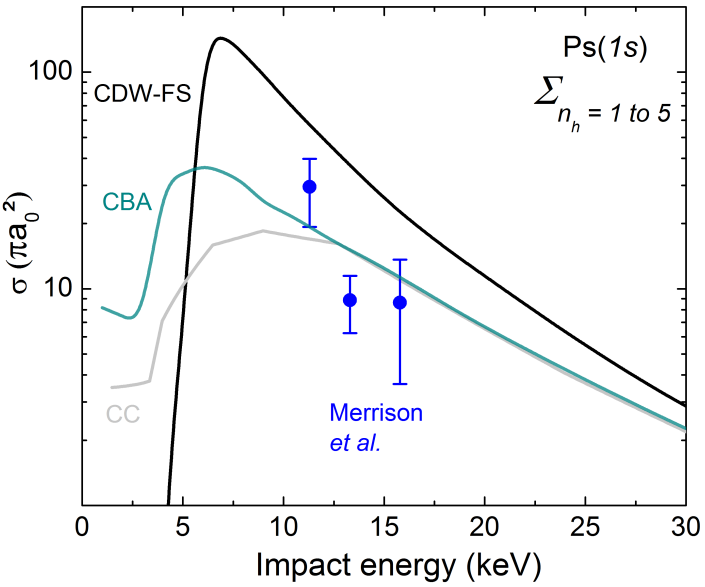

Figure 2.2: Figure from [36] comparing the experimental results of Merrison *et al.* [40] (•) and three different cross section models of the H reaction for positronium in the ground state. In the case of the experimental data points no distinction is made between the hydrogen energy states. The cross sections were evaluated with the hydrogen excited up to the $5d$ state.

In the first phase of the ANTION project, the LINAC positron source at Saclay will be employed (see Chapter 3 for a description of this apparatus). Since this LINAC (4.3 MeV providing a flux of $3\times10^6 e^+/s$) produces less energetic electrons than the one at CERN, the expected positronium density in the cavity is lower - of the order of $10^{10}\,cm^{-3}$, assuming 10^8 positrons are accumulated. Therefore, only the hydrogen production cross section can be measured since a denser positronium cloud is needed for the H^- reaction. Moreover, the positronium will be in the ground state. In a first approach, the goal is to try to reproduce Merrison *et al.* results, i.e select the protons' impact energies 11.3 keV, 13.3 keV and 15.8 keV; later one would like to validate the theoretical cross sections by scanning the impact energy. At CERN a similar study will be performed for the antimatter reactions, while for the GBAR experiment lower impact energies are preferred since the cross sections are higher, according to [37, 43].

2.1.2 $\bar{H}^+$ cooling and the $\bar{g}$ measurement

After being formed, the antihydrogen ions will be electrostatically separated from the antihydrogen atoms and from the antiprotons, and guided to a RF Paul trap, already inside the free fall vacuum vessel. There, the anti-ions will be sympathetically cooled to 10 mK by a Doppler-cooled crystal of $^9Be^+$ and HD^+, or H_2^+ ions, in millisecond time scales. Further cooling is still required, hence an individual $\bar{H}^+$ and a Be^+ ion will be transported to another Paul trap, named precision trap. Here, they will be cooled by Raman side-band cooling [44], reaching 1 neV. A more detailed description can be found in [45]. The $\bar{H}^+$ is now ready to lose the excess positron by photodetachment,

becoming neutral for the free fall measurement.

The gravitational acceleration of $\bar{H}$, $\bar{g} = \frac{\bar{m}_g}{\bar{m}_i} g$, will be measured by determining the time interval between the photodetachment and the impact of $\bar{H}$ on an annihilation plate after its free fall, Δt. The photodetachment laser pulse defines the start time of the free fall, while the stop is defined by the detection of the pions that result from the annihilation of the antiprotons, once the $\bar{H}$ hits the walls of the vacuum chamber.

The equation that describes the free-fall movement is:

$$\Delta z = \frac{1}{2}\bar{g}\Delta t^2 + v_{0,z}\Delta t\,, \tag{2.6}$$

where Δz is the distance between the second Paul trap and the annihilation plate, which is known with precision, and $v_{0,z}$ the initial vertical velocity after photodetachment. The latter term presents the main source of uncertainty. Its origin is the energy of the $\bar{H}$ atom, and from the recoil of the photodetached positron. At 1 neV, 1500 annihilations are necessary to achieve 1% precision on $\bar{g}$ [15].

The $\bar{H}$ annihilates into two 511 keV photons and, in 95% of the cases, the proton-antiproton annihilation produces a set of charged and neutral pions, with 99% of the latter decaying into two high energy gamma rays. The detection of the annihilation products requires both vertex position reconstruction, provided by a charged particle tracker, and accurate timing of the annihilation made possible by scintillator counters surrounding the tracker.

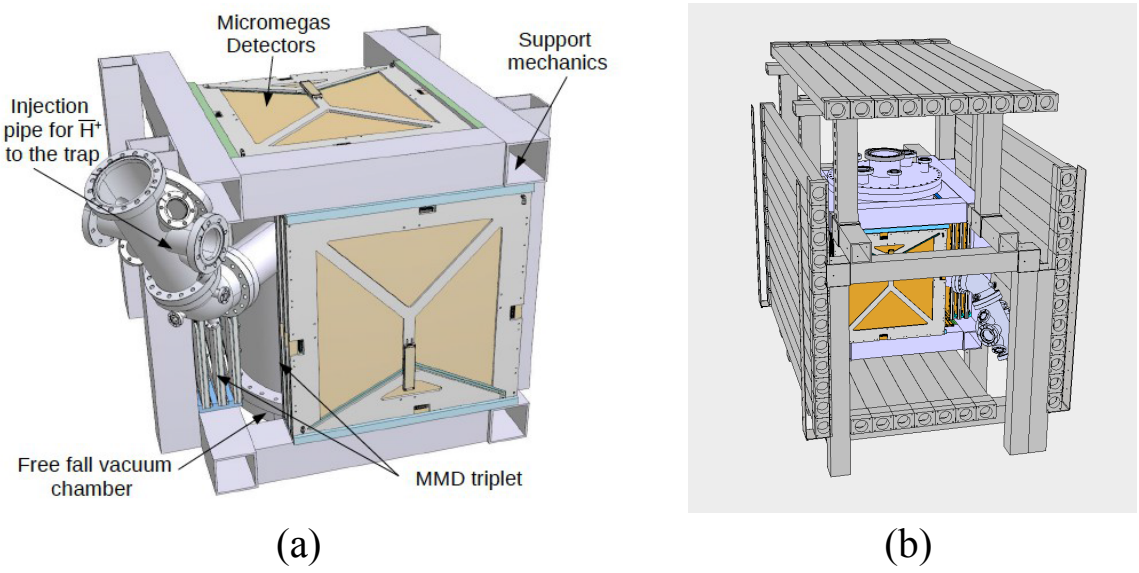

Figure 2.3: A preliminary drawing of the free fall chamber, Micromegas and time-of-flight detectors. (a) 18 50×50 cm^2 Micromegas detectors are arranged in 6 triplets to cover all sides of the vessel. The $\bar{H}^+$ ions enter the chamber from the side into the first Paul trap located in the interior. (b) 44 plastic scintillators and 88 PMTs compose the time-of-flight apparatus, providing a 0.2 ns resolution of the $\bar{p}$ annihilation time and cosmic ray rejection.

The charged particle tracker will consist of a set of planar chambers that allow the measurement of both x and y coordinates with an accuracy of a few hundred microns. To achieve this, micro-mesh gaseous detectors (Multiplexed Resistive XY Micromegas) [42] of dimensions $50\times50\,\mathrm{cm}^2$ with a pitch of $400\,\mu$m have been developed. In order to ensure a good tracking efficiency, each of the 6 faces surrounding the vacuum vessel will be equipped with 3 layers of chambers. This configuration will result in a spatial resolution of the order of 1.5 mm in the vertex reconstruction of the antihydrogen annihilation point. Four walls of scintillator arrays will surround the Micromegas tracker with the purpose of detecting charged tracks and some of the γ-rays from positron and antiproton annihilations, providing the time of the annihilation with a resolution smaller than 0.2 ns. They will also contribute to cosmic ray rejection, being able reduce the background fraction below 0.2%. A drawing of the free fall chamber can be seen in figure 2.3, as well as the tracking and time-of-flight detectors.

2.2 GBAR challenges and competition

Each step of the GBAR endeavor is a scientific achievement in itself. First of all, no other group has ever formed a plasma with 10^{10} positrons, with the present record being $\sim4\times10^9$, which took 4.5 hours to accumulate [46]. In fact, a buffer gas trap has never been used in combination with a LINAC. This thesis aims to prove that such a combination is indeed possible. Furthermore, the production and cross section measurement of the $H-$ and $Hbar+$ reactions have never been executed before and are technically very challenging, namely the focusing of a positron and antiproton beam in a very small cavity with a section of $1\,\mathrm{mm}^2$, the extraction and acceleration of a 10^{10} particle beam from a 5 T magnetic field to a "zero" field region, and in particular the detection of the (anti)atoms and (anti)ions. The feasibility of capturing $\bar{\mathrm{H}}^+$ ions and cooling them to micro kelvin temperature still needs to be proved. Capturing the $\bar{\mathrm{H}}^+$ ions with an energy of several keV and cooling them down to an energy of the order of 10^{-9} eV, implies an energy reduction of 12 orders of magnitude. Nonetheless, the results of simulations are promising suggesting the capture efficiency can be larger than 50%, if the anti-ions' energy spread, ΔE, is smaller than 25 eV [45]. They also show that the ions can be sympathetically cooled in 10 ms for an initial kinetic energy of 18.5 meV (more than 400 K) [47]. Hilico and co-workers are in the process of sympathetic cooling H_2^+ or H^+ ions with these technique with the goal of studying and optimizing this technique before applying it to anti-ions [45]. At last, ultra-high vacuum techniques need to be employed in the traps and in the free fall chamber, since these (anti)ions/atoms are rare and annihilate easily when in contact with any residual gas. Not less important, any stray magnetic fields need to be eliminated (shielding the free fall chamber with mu-metal for example) in order to not perturb the Raman side band cooling and the $\bar{\mathrm{g}}$ measurement.

Two other collaborations are attempting to measure the gravitational acceleration of $\bar{\mathrm{H}}$, at CERN. Recently, the ALPHA collaboration reported a proof-of-concept experiment [48] that measured $|\bar{m}_g/\bar{m}_i| < 75$ with a statistical significance of 5%. While this measurement is significant in the sense that it was the first $\bar{\mathrm{g}}$ measurement, it does not allow to any conclusion specially regarding the sign of the gravitational force.

Moreover, the experimental setup used by ALPHA was not conceived with this measurement in mind, but to perform $\bar{H}$ spectroscopy . For that reason, a new apparatus will be constructed, named ALPHA-g [49], to make this measurement with 1% accuracy. This setup is a vertical adaptation of the ALPHA antihydrogen trap [50], in which cold (<500 mK) $\bar{H}$ atoms are released in a controlled way to execute the free fall. A tracking vertex detector, a Time Projection Chamber (TPC) [51], pinpoints the position of the antiproton annihilation on the walls of the trap. ALPHA-g is particularly well positioned to be the first experiment to achieve 1% accuracy, as all the required techniques to perform this measurement have already been demonstrated by the collaboration, in particular their expertise in trapping antihydrogen.

Another competitor is the AEgIS (Antimatter Experiment: Gravity, Interferometry, Spectroscopy) collaboration [52]. Their goal is to perform the gravity measurement by observing the vertical displacement of a $\bar{H}$ beam with velocity in the range 400 m/s to 600 m/s, as it traverses a Moiré interferometer with two gratings. The antihydrogen beam eventually annihilates on an emulsion detector, that determines the position of the annihilation vertex with a spatial resolution of 1 μm [53]. The vertical shift is given by $\Delta y = F\tau^2/m$, where F is the gravitational force, τ the time of flight between two interferometer gratings and m the $\bar{H}$ mass. A shift of the order of 10 μm is expected. While ALPHA produces antihydrogen by mixing an antiproton plasma with a positron plasma in a Penning-type trap, AEgIS will produce the antihydrogen atoms using the charge exchange reaction *Hbar*, but with positronium excited to Rydberg states (high quantum number states). This not only increases the reaction cross section, as it scales with n^4, but also allows the production of antihydrogen in Rydberg states which, due to their large dipole (scales with the square of the principal quantum number), allows the manipulation of the atoms using electric fields (using the Stark effect) and the production of an antihydrogen beam. The AEgIS collaboration have a head start in comparison to GBAR: they can routinely trap 10^8 positrons and excite positronium to Rydberg states. They are also able to trap antiprotons but have yet to produce an antihydrogen atom. While they have proven the feasibility of the free fall measurement using this technique with antiprotons with 106 keV mean energy [54], they still have a long road ahead to produce a $\bar{H}$ beam with 500 m/s velocity, to obtain the desired 1% accuracy.

2.3 Thesis outline

The main goal of this thesis is to develop some of the tools necessary for the hydrogen cross section measurement, in the framework of the GBAR collaboration. These tools include a buffer gas trap for the trapping and accumulation of positrons, and a Monte Carlo simulation of the time and spatial distribution of the positronium atoms in the reaction cavity. The remainder of this thesis is organized as follows:

- **Part II** is dedicated to positron production and accumulation in the buffer gas trap. In **Chapter 3** the positron source and the beam line present at Saclay are described. **Chapter 4** provides a few theoretical tools necessary to understand the physics of positron traps and an historical overview of the Penning trap, in which this trap is based on. In addition, this chapter includes a detailed description of the trap that was built during the course of this thesis. **Chapter 5** presents the experimental work conducted to commission and optimize the trap. It describes trapping protocols and optimization procedures designed to increase the trap performance, as well as the study of the effect of the buffer and cooling gas and the application of the rotating wall technique.

- **Part III** presents a Monte Carlo simulation developed to evaluate the time and spatial evolution of the ortho-positronium atoms in the reaction cavity. An estimation of the number of hydrogen atoms produced as a function of the proton impact energy is given, according to the theoretically computed cross sections for hydrogen production. In addition, a suggestion is proposed to increase the number of positronium atoms in the cavity. Finally, the background signal that contaminates the ortho-positronium signal is evaluated.

- **Part IV** includes the study of a positron moderator - a material that emits slow positrons upon impact with a positron beam. Firstly, a brief introduction regarding the physics of positron moderation is given, followed by a description of the experimental setup employed in this study. The measurements of the work function and diffusion length of an epitaxially grown layer are reported, as well as the moderation efficiency. While being a small parallel project undertaken during this thesis, it is closely related to GBAR experiment as it can potentially increase the efficiency of positron trapping.

- **Part V** concludes this thesis by summarizing the achieved results and by providing some suggestions for the future progress of the work described.

Part II

A positron bottle Enterprise

3 Positron source and transport

"Any sufficiently advanced technology is indistinguishable from magic."
Arthur C. Clarke

Contents

This chapter describes the pulsed positron beam source at CEA Saclay, which was used in the experiments reported in this thesis. A brief summary of positron sources is firstly given, followed by a description of the positron source at Saclay, and concluding with the characterization of the positron beam.

3.1 Positron sources

There are two ways of producing positrons: β^+ decay and positron-electron pair production, when a γ-ray with energy greater than the energy of an electron and a positron, 1.022 MeV, interacts with the electric field of a surrounding atomic nucleus. Most positron experiments, and in particular table-top positron sources, use a β^+ emitter as a positron source. In an isotope rich in protons, a proton is converted by weak interaction into a neutron, emitting a positron and a neutrino.

The ^{22}Na nuclide combines a relatively long half life of 2.6 years and a high positron yield of $\sim 90\%$. It is, therefore, the most common isotope used in positron experiments. It decays into an excited state of ^{22}Ne, which subsequently de-excites into the ground state emitting a 1275 keV γ-ray:

$$^{22}\mathrm{Na} \rightarrow ^{22}\mathrm{Ne} + \beta^+ + \nu_e + \gamma\,. \tag{3.1}$$

Since the lifetime of the excited neon is only 3.7 ps, the γ-spectrum of ^{22}Na contains two lines corresponding to 511 keV (from the positron annihilation) and 1275 keV (from the ^{22}Ne de-excitation).

Intense γ-radiation sources include nuclear fission, de-excitation of excited nuclear states and bremsstrahlung. Electron linear accelerators (LINAC) produce high energy pulsed electron beams that can be decelerated by impinging the electrons on a target, thus providing high energy bremsstrahlung radiation. Given that the pair production cross section is approximately proportional to Z^2, dense materials, such as tungsten or tantalum, are used to convert the high energy γ-radiation into positrons [55].

The positrons produced by these mechanisms have a broad energy distribution spanning several hundreds of keV or even a few MeV, thus moderators need to be employed to form monoenergetic beams. A description of moderating processes is given in Chapter 7. Typically, metals with negative positron work function, such as tungsten, or solid rare gases, such as neon, are commonly used.

3.2 The positron source at Saclay

The positron source at Saclay is a LINAC based source, with a tungsten target and moderator. It was developed as a prototype of an intense but compact positron source [56] to be used at CERN in the GBAR experiment. This source can be divided into three main parts:

1. **A linear electron accelerator (LINAC)** which produces a 4.3 MeV beam of electrons with an estimated flux of $\sim 3.5 \times 10^{12}\,\mathrm{e}^-$/pulse. A schematic drawing and a picture of the LINAC apparatus is shown in figure 3.1.

2. **A $\mathbf{e^- \rightarrow e^+}$ converter** which consists of a 1 mm thick water cooled tungsten target that decelerates the electrons which emit Bremsstrahlung radiation, followed by pair e^-/e^+ creation inside the target. The converter is shown in figure 3.2.

3. **An annealed tungsten moderator** that slows down the positrons to 3 eV. These particles are subsequently accelerated to a variable energy by a high transmissivity grid. A picture of the moderator is shown in figure 3.3.

The LINAC, of type LINAX5, was bought from the Linac Technologies Company, and produces a 4.3 MeV electron beam with 140 mA peak current and a pulse length of 4 μs at a maximum repetition rate 200 Hz. Electrons generated by a hot cathode are accelerated by five cavities resonant at 3 GHz. The radio frequency waves are provided by a magnetron. In front of the cavity a quadrupole triplet focuses the electron beam onto a tungsten target. Two scintillation detectors (NaI and plastic) monitor the positron flux in strategic locations, i.e. immediately after the concrete bunker enclosing the LINAC, and before the buffer gas trap. A positron flux of the order $3 \times 10^6\,e^+$/s is routinely obtained.

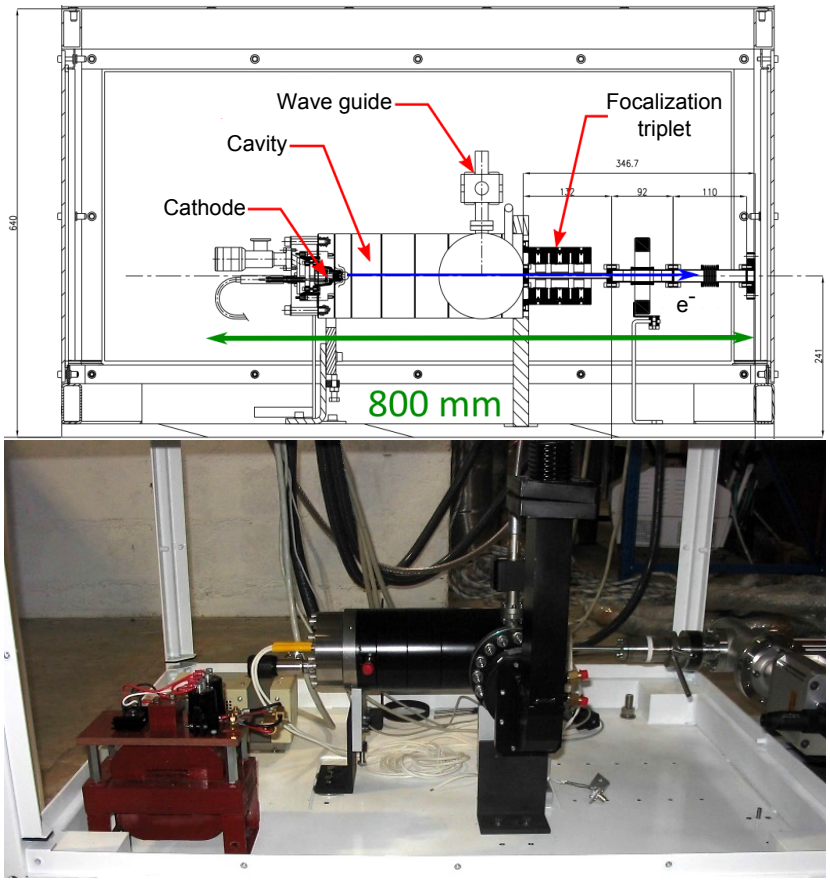

Figure 3.1: Schematic drawing and picture of the electron linear accelerator. It is composed of a hot cathode; five cavities where the RF waves accelerate the electrons to 4.3 MeV; a quadrupole triplet focuses the electron beam onto a tungsten target.

Adiabatic transport of the positron beam

In the presence of a magnetic field the motion of a charged particle can be decomposed into two components: a longitudinal component parallel to the magnetic field $v_{\parallel}$, and a perpendicular component, $v_{\perp}$. The perpendicular component corresponds to a cyclotron motion, in which the cyclotron frequency, Ω_c, is dependent on the magnetic field via $\Omega_c = qB/m$, where q is the electric charge, B is the magnetic field and m is the particle mass. If the transport is adiabatic, the cyclotron radius, $\rho_c = v_{\perp}/\Omega_c$, is small compared to the distance over which the magnetic field varies, $|B/\nabla B|$. Moreover, the time scale of the magnetic field variation is slower than the cyclotron period [57]. This can be expressed by the relationships [58]

$$\rho_c \ll \left| \frac{B}{\nabla B} \right| , \tag{3.2}$$

$$\Omega_c \gg \left| \frac{\delta B}{\delta t} \frac{1}{B} \right| . \tag{3.3}$$

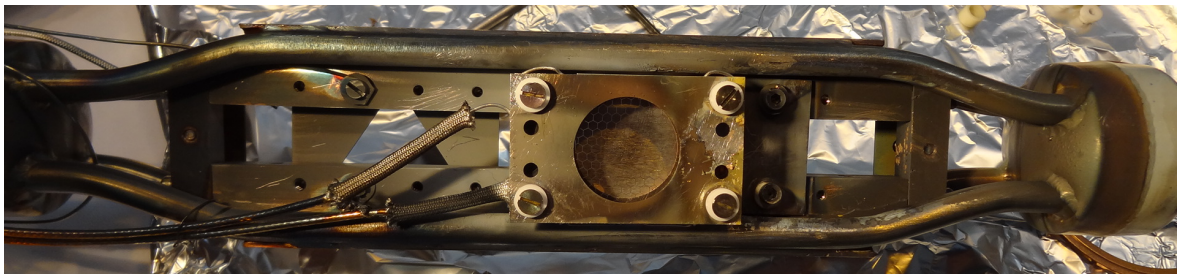

Figure 3.2: Picture of the support of the tungsten target and moderator. The support is inserted in a vacuum vessel in front of the LINAC. On the left there is a beam profiler with a triangular shape, in the center lies the target and the moderator, and on the right a second target without moderator. This support can be translated using a linear drive.

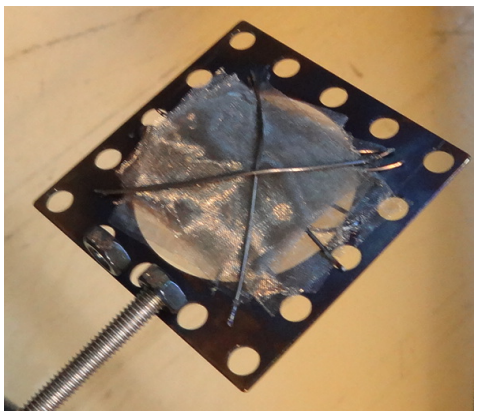

Figure 3.3: Picture of the moderator. Twelve layers of tungsten mesh are stacked to form the moderator.

When the transport is adiabatic, the positron orbit can be described using the guiding center approximation [58], in which the center of the cyclotron orbit follows the magnetic field lines. In this approximation two invariant quantities can be considered, namely the positron orbital magnetic moment

$$\mu = \frac{m v_\perp^2}{2B} = \frac{E_\perp}{B}\,, \tag{3.4}$$

and the positron total energy

$$E_{tot} = E_\parallel + E_\perp\,, \tag{3.5}$$

where $E_\parallel$ and $E_\perp$ are the positron energy parallel and perpendicular to the magnetic field, respectively. The coupling of the parallel and perpendicular energies resulting from these invariant quantities implies that when a positron travels from a region with low magnetic field to a high magnetic field region, its perpendicular energy increases, thus the parallel energy decreases. If the ratio of the magnetic fields in the two regions

is so large that all the parallel energy is converted into perpendicular energy, then the positrons are reflected. This phenomenon is denoted by magnetic mirroring.

At Saclay, the positrons travel 16 m before entering the buffer gas trap along a $\sim$8 mT magnetic guiding system consisting of solenoids wound directly to the vacuum tube, and steering and correcting coils for the elbows and vacuum flanges. This magnetic field was chosen so that the positrons' cyclotron radius, is not larger than 1 mm, allowing for adiabatic transport of the beam [59]. In a $\sim$8 mT magnetic field the cyclotron frequency is 1.4 Grad^{-1}. Assuming a positron has a transversal energy $E_\perp$=1 eV, then the corresponding cyclotron radius is 0.4 mm. If one considers a 30% drop in the magnetic field during a 10 cm magnetic field interruption (a vacuum cross with a target, for example), then the inequality in equation 3.2 is satisfied:

$$\rho_c = 4 \times 10^{-4}\, m \ll \left| \frac{B}{\nabla B} \right| = 0.4\,\mathrm{m}. \tag{3.6}$$

If now one considers that the positron has $E_\parallel = 50$ eV, then it takes 24 ns to go through the 10 cm interruption. Assuming the same change in magnetic field, then the inequality 3.3 is also satisfied:

$$\Omega_c = 1.4 \times 10^9\,\mathrm{s}^{-1} \gg \left| \frac{\delta B}{\delta t} \frac{1}{B} \right| = 1.25 \times 10^7\,\mathrm{s}^{-1}\,. \tag{3.7}$$

Along the positron beam line there are interruptions in the solenoids to insert pumps and targets that monitor the beam, as well as curved sections (elbows). These interruptions distort the magnetic field therefore correcting coils are used. However, as will be demonstrated in the next section, the energy spread of the beam still increases along the beam line.

The radial position, r, of the positron guiding center as it travels between two points with different magnetic fields B(z_0) and B(z) is given by

$$r = r_0 \sqrt{\frac{B(z_0)}{B(z)}}\,, \tag{3.8}$$

where r_0 is the initial displacement of the guiding center from the z-axis.

3.3 Positron beam characterization

The positron beam profile was viewed using a microchannel plate detector (MCP) in combination with a phosphor screen and a CCD camera, located downstream of the buffer gas trap - figure 3.4 (a 100 ms exposure time was used, corresponding to 5 positron bunches). The moderator grid and the stainless steel wires can be seen, suggesting a good transport.

3.3.1 Electrons

Secondary electrons originated in the LINAC and tungsten target/moderator apparatus were observed using the MCP. Figure 3.5a shows a picture of the MCP in which both

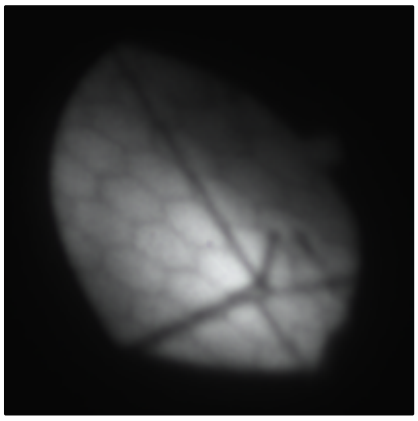

Figure 3.4: Image of the positron beam on a MCP. The picture was taken with a 100 ms exposure time, corresponding to 5 positron bunches. The moderator grid and stainless steel wires used to hold the meshes can be observed.

the positron beam (closer to the center) and an electron beam can be observed (closer to the edge). The front plate of the MCP was set to -100 V. This beam is composed of electrons because the beam intensity decreased as the voltage of the grid in front of the MCP decreased. When the grid was set to -300 V, the electrons could no longer be seen, suggesting that the maximum energy of the electrons is ~ 300 eV.

Figure 3.5a shows that the axial position of the electrons is different from the positrons. In a curved magnetic field, which is the case of an elbow of the beam line, the positrons and electrons move along the curved magnetic field lines and are under the influence of a centrifugal force, directed to the curvature. This force causes a drift, curvature drift, and its velocity is proportional to the square of the particle's parallel velocity, $v_\parallel$ [57]:

$$\vec{v}_{\mathrm{R}_C} = \frac{m v_\parallel^2}{R_C^2} \frac{\vec{R}_C \times \vec{B}}{qB^2} \,. \tag{3.9}$$

Here m is the mass of the positron, q the charge and R_C the curvature radius. Since the electrons have a much higher initial parallel velocity than the positrons, their drift velocity is also higher (six times higher, for $v_{\parallel_{e^-}} = 300$ eV and $v_{\parallel_{e^+}} = 50$ eV). Moreover, due to their opposite charges, electrons and positrons drift in opposite directions. These arguments explain the larger axial drift for electrons. However, the beam line has five of these elbows, thus a simulation of the magnetic transport would be required to evaluate the total axial drift to confirm this hypothesis.

To block the electrons from entering the buffer gas trap, a plate with holes was inserted in front of the beams. Figure 3.5b shows that only the positron beam is allowed to pass through the hole.

At CERN, the LINAC will produce many more electrons than at Saclay, hence this effect will be aggravated. Although, the impact of the electrons in the efficiency of the buffer gas trap is not clear, it can possibly ionize the gas. While the solution of blocking the electrons with a plate with holes is practical and inexpensive, it comes with the disadvantage that some positrons are also blocked, or that the electrons might

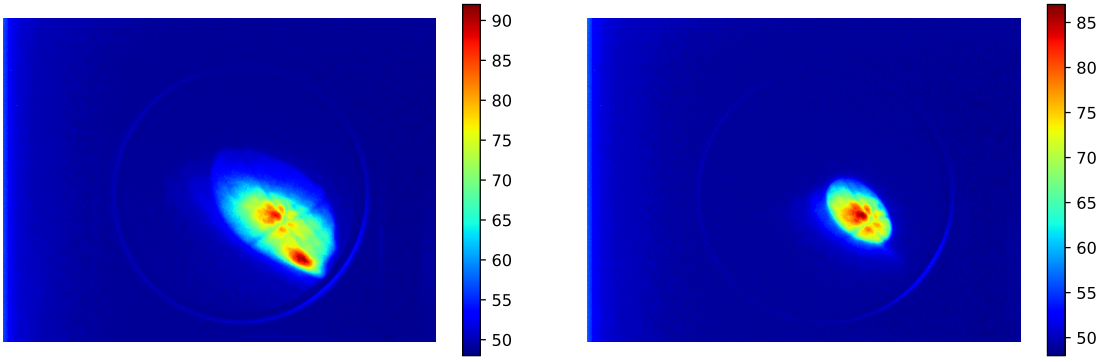

(a) (b)

Figure 3.5: Image of the electron and positron beam on the MCP assembly. In both pictures the front plate of the MCP was set to -100 V. (a) Both the positron beam (closer to the center) and the electron beam can be observed (closer to the edge). (b) The electrons were blocked by a plate containing a hole that allows the positrons to go through.

not be all blocked. An alternative would be to block the electrons using an electrode located before the buffer gas trap.

3.3.2 Positron beam parallel energy distribution

The parallel energy spread of the positron beam was measured using a Retarding Potential Analyzer (RPA), i.e. a voltage V was applied to a grid with high transmissivity allowing particles with $E_{\parallel} > V$ to pass through and annihilate on a target. The γ-rays resulting from the annihilation were detected by a plastic scintillator mounted on a XP2020 photomultiplier. By varying V, the cumulative parallel energy distribution of the positron beam is obtained, as well as the energy dispersion, $\sigma_{\parallel}$, and the mean parallel energy, $\bar{E}_{\parallel}$.

The distribution was measured immediately after the moderator, although the target was located almost 16 m further away. This shouldn't affect the measurement. The data points are plotted in figure 3.6a, along with a complementary error function fit and its negative derivative. The parameters obtained from the fit are $\sigma_{\parallel}$=1.18 $\pm$ 0.02 eV, FWHM = 2.79 $\pm$ 0.03 eV and $\bar{E}_{\parallel}$ = 54.12 $\pm$ 0.01 eV. The energy spread of the moderated positrons is in agreement with other studies of tungsten mesh moderators (FWHM = 2.1 eV [60]).

In this measurement the moderator potential was set to 52.5 V. Knowing that the work function of the tungsten is $\sim$3 eV [61], one would expect that the positrons' maximum energy would be 55.5 eV. The maximum energy obtained was $\sim$56.4 eV (computed by taking the mean of the last few data points), which is reasonable as statistical and systematic errors were not considered.

The parallel energy distribution is expected to vary as the positron beam travels through a non-uniform magnetic field, which can be due to interruptions in the solenoids, but more importantly, because the positrons are generated in a stronger

field than the field present in the beam line. To evaluate the increase of the parallel energy dispersion, the energy distribution measurement at the location of the moderator, in a 133 G magnetic field, is compared to the same measurement but performed downstream the beam line, where the field is of the order of 80 G. Figure 3.6a shows the measured cumulative parallel energy distribution for both cases, and figure 3.6b presents the negative derivative of the fits. The data points were normalized to make the comparison more clear. In the measurement done at the location of the moderator, the positrons were accelerated to 52.5 eV, while in the measurement done downstream the beam line, the positrons were accelerated to 49.5 eV, hence $\bar{E}_{\parallel}$ should not be compared.

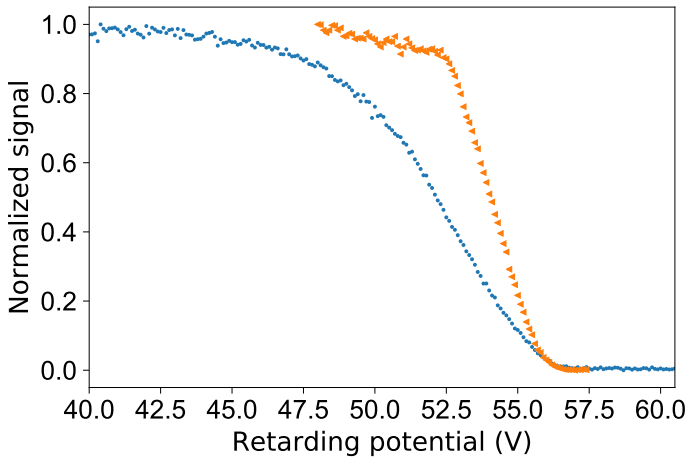

(a)

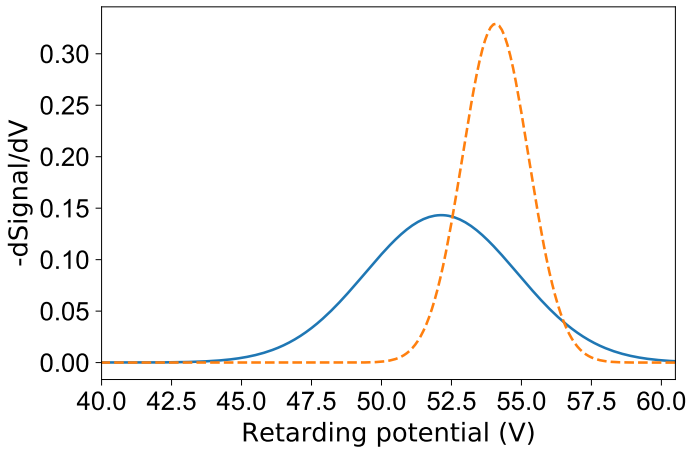

(b)

Figure 3.6: (a) Measured cumulative parallel energy distribution immediately after the moderator (▶) and upstream of the buffer gas trap (●). A complementary error function fit yielded $\sigma_{\parallel}$= 1.18 ± 0.02 eV for the moderator location and $\sigma_{\parallel}$ = 2.72 ± 0.03 eV for the location before the trap. (b) The negative derivative of the fit at the moderator location (- -) and immediately before the trap (—). The data points were normalized to make the comparison more clear.

As expected, the energy distribution measured downstream the beam line is broader, with $\sigma_{\parallel} = 2.72 \pm 0.03\,\text{eV}$ than the one measured in the location of the moderator, $\sigma_{\parallel}$=1.18 $\pm$ 0.02 eV. This behavior is analyzed in more detail in Chapter 5, section 5.1.2, where the positron beam parallel energy distribution was measured at the entry of the buffer gas trap in order to evaluate its impact on the trapping efficiency.

4 Buffer gas trap

"It all started at lunch with Marv."
C. M. Surko

Contents

Unlike other antimatter experiments that routinely produce antihydrogen, GBAR requires antihydrogen ions in order to cool them to around 1 neV energy before the free fall measurement. However, the production yield of $\bar{H}^+$ is very low and is proportional to the square of the positronium density. Hence, a very dense positronium cloud of the order of $10^{12}\,\mathrm{cm}^{-3}$ is required, corresponding to a positron pulse of $\sim 10^{10}$ positrons. To realize such a pulse and to be able to use it at will, positrons produced by a source must be slowed down to electron-volt energies and confined in an "antimatter bottle". A Penning trap is a device akin to this "bottle", in which a combination of an axial magnetic field and an electric field is used to confine charged particles. It was invented by Hans Georg Dehmelt [62] and named after F. M. Penning, as Dehmelt was inspired by Penning's vacuum gauge (cold cathode ionization gauge). In 1989, Dehmelt shared the Nobel Prize in Physics for the development of the ion trap technique.

This kind of trap is commonly found in the fields of atomic physics and non-neutral plasma physics. Precise mass spectrometry is possible with Penning traps since the mass can be determined from one of the motion frequencies of the particles (cyclotron

frequency). This method is employed in the ISOLTRAP experiment that performs high-precision mass measurements on short-lived nuclides with an uncertainty below 10^{-8} [63]. A few significant measurements conducted in a Penning-type trap include the electron mass [64] and the antiproton to proton charge-to-mass ratio [20] with 69 parts per trillion precision. In 2008, Hanneke *et al.* measured the gyromagnetic ratio, γ_e, of an electron to 0.28 ppb, providing a stringent test to the theory of quantum electrodynamics (QED) which predicts γ_e to high precision [65]. In antihydrogen physics, Penning-type traps are paramount for the confinement of antiprotons and positrons plasmas. In 2002, the ATHENA collaboration produced the first low-energy antihydrogen atom by mixing an antiproton plasma with a positron plasma [16].

In this chapter a brief description of the physics at play in a Penning trap is given, so to give a foundation for the working principle of a buffer gas trap. The trap assembly is the core of this thesis as it was built during the course of this thesis and was amply used for the studies reported in this dissertation. For that reason the setup is described in detail, including the hardware and software that allows its operation and diagnosis.

4.1 Ideal Penning trap

In a Penning trap, charged particles are confined axially by an electric field and radially by a magnetic field. To trap positively charged (negative) particles, endcap electrodes are held at a positive (negative) potential relative to a ring electrode. A schematic drawing of a Penning trap is presented in figure 4.1. The uniform axial magnetic field $\mathbf{B} = \mathrm{B}\ \hat{\mathbf{z}}$ forces the particles into circular orbits in the x-y plane. An electrostatic quadrupole potential, Φ, is generated by three electrodes with a hyperboloid shape and has the form

$$\Phi = \frac{V_0}{R^2}\left(2z^2 - x^2 - y^2\right), \tag{4.1}$$

where $\mathrm{V_0}$ is the trap potential and R^2 is equal to $\rho_0^2 + 2\mathrm{z}_0^2$, where ρ_0 and z_0 are the distances from the trap center to the ring and endcap electrodes, respectively. This potential contains a saddle point at the center of the trap, confining the particles in the axial direction.

The equation of motion of a charged particle follows from the Lorentz force,

$$\mathbf{F} = q\left(\mathbf{E} + \dot{\mathbf{r}} \times \mathbf{B}\right) = m\ddot{\mathbf{r}} \tag{4.2}$$

for a particle with mass m, charge q and position $\mathbf{r} = (x, y, z)$. The electric field generated by the Penning trap is of the form

$$\mathbf{E} = -\nabla\Phi = \frac{V_0}{R^2}\left(-4z\hat{\mathbf{z}} + 2x\hat{\mathbf{x}} + 2y\hat{\mathbf{y}}\right). \tag{4.3}$$

The axial motion corresponds to the simple harmonic motion given by

$$\ddot{z} + \omega_z^2 z = 0, \tag{4.4}$$

with an angular oscillation frequency (axial bounce frequency)

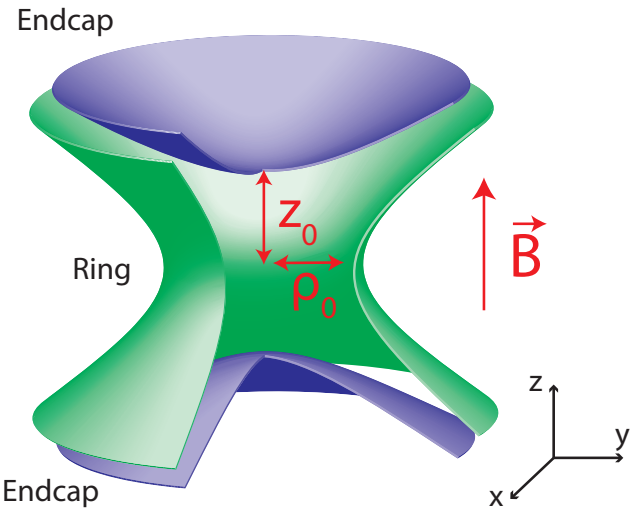

Figure 4.1: Schematic drawing of a section of a Penning trap consisted of three electrodes (two endcaps and one ring) with a hyperboloid shape, forming a quadratic potential. The magnetic field is applied in the direction of the z axis.

$$\omega_z = \sqrt{\frac{4qV_0}{mR^2}}\,. \tag{4.5}$$

If the electric field was not present, the particle would execute a cyclotron motion in the x-y plane with a frequency $\Omega_c = qB/m$, denominated cyclotron frequency. However, the combination of electric and magnetic fields gives rise to a more complex radial trajectory. By defining a complex variable $u = x + iy$, the radial (x,y) equations of motion can be combined in a single equation:

$$\ddot{u} - i\Omega_c\dot{u} - \frac{1}{2}\omega_z^2 u = 0, \tag{4.6}$$

which can be solved by making the substitution $u = u_0 e^{-iwt}$, giving the equation

$$2\omega^2 - 2\Omega_c\omega + \omega_z^2 = 0 \tag{4.7}$$

with the roots

$$\omega_\pm = \frac{1}{2}\left(\Omega_c \pm \sqrt{\Omega_c^2 - 2\omega_z^2}\right)\,. \tag{4.8}$$

The solution to the radial equation of motion is a superposition of two circular motions: the cyclotron motion with the modified cyclotron frequency, ω_+ (also denoted by ω_c), that corresponds to the positive root, and the magnetron motion with the frequency ω_- (often denoted by ω_m), corresponding to the negative root. Equation 4.8 requires that $\Omega_c^2 > 2\omega_z^2$ for the particles to be confined in the trap, which is equivalent to

$$B > \sqrt{\frac{8m}{q}\frac{V_0}{R^2}}\,. \tag{4.9}$$

This establishes a stability limit, i.e. when the electric field is strong enough to overcome the magnetic confinement the particles cannot be radially confined. Typically in a Penning trap the frequencies form the hierarchy

$$\omega_m < \omega_z < \omega_c < \Omega_c \,. \tag{4.10}$$

A positron in a low magnetic field trap typically has the following frequency values in $\mathrm{rad\,s^{-1}}$ units

$$\omega_m = 10^5 < \omega_z = 4 \times 10^7 < \omega_c \sim \Omega_c = 7 \times 10^9 \,,$$

assuming $\mathrm{V_0/R^2} = 10^5\,\mathrm{V/m^2}$ and $\mathrm{B} = 40\,\mathrm{mT}$. The motion of a single charged particle confined in an ideal Penning trap is illustrated in figure 4.2.

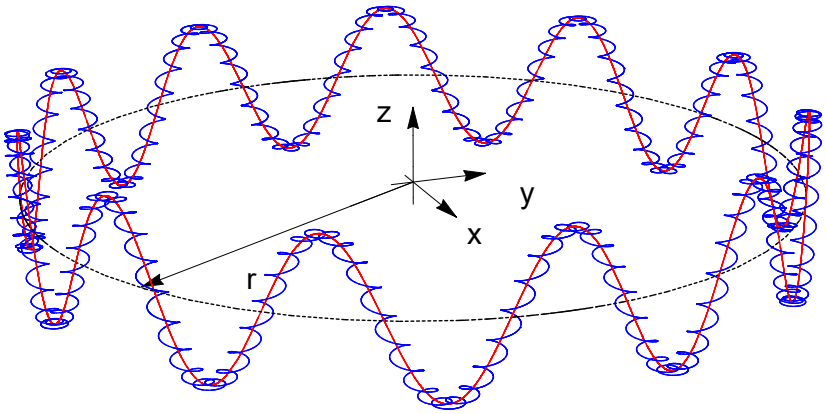

Figure 4.2: Motion of a charged particle in a Penning trap. The motion consists of a slow magnetron drift around the trap center (black), the axial motion (red), and the modified cyclotron motion. The superposition of all three motions is shown in blue.

The Penning trap comes with some practical disadvantages: due to its closed geometry it is hard to access the interior of the trap making it difficult to load and unload particles. Moreover, it limits the use of diagnostics and the introduction of laser beams. Any hole in the electrodes can distort the quadratic potential. Modifications to the trap geometry are possible if the effects on the quadratic potential are taken into consideration.

To overcome these drawbacks, in 1975 Malmberg and deGrassie developed a cylindrical trap, known as Penning-Malmberg trap, and reported the confinement of a non-neutral electron plasma [66]. Later, G. Gabrielse *et al.* showed that a set of cylindrical electrodes with carefully chosen lengths and voltages is able to near reproduce the quadratic potential of a Penning trap [67]. Three, five and seven electrode traps can provide harmonic potentials, with varying degree of harmonicity, if compensation electrodes are employed [68]. Cylindrical Penning traps provide not only easy access, but the electrodes are also easier to machine, which should reduce the trap anharmonicity.

4.2 Buffer gas trap

The trap developed for GBAR is based on a Surko buffer gas trap. Surko and co-workers invented a positron accumulator that slows down a positron beam to electronvolt energies and accumulates them in a trap [69] [70]. Surko's buffer gas trap is a modified Penning-Malmberg trap that consists of a series of cylindrically symmetric electrodes of varying inner diameters. These form three distinct trapping stages with three distinct pressure regions, and confine the positrons axially by producing electrostatic potentials. The positrons are confined radially by a static magnetic field produced by one solenoid enclosing the electrodes. The principle of this trap is that incoming positrons lose their energy through inelastic collisions with a buffer gas that is introduced in the first stage of the trap. As they cool down, they become trapped in successively deeper potential wells, and progressively lower pressure, until the positrons are confined on the lowest pressure region of the trap - stage 3, where the lifetime is longer (figure 4.3).

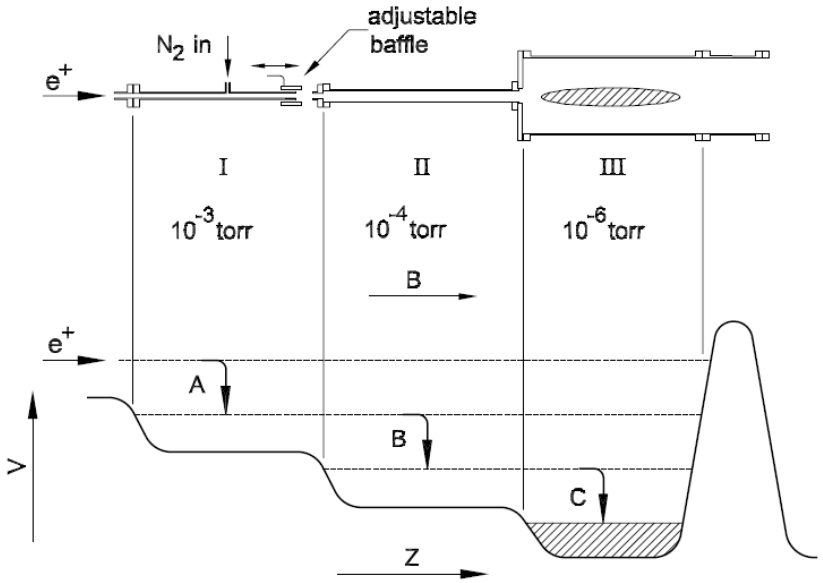

Figure 4.3: Diagram of Surko's three stage positron accumulator [71]. Each stage corresponds to a set of electrodes with successively larger diameter, creating three distinct pressure regions. The electrostatic potential is tuned to maximize the trapping efficiency by setting the step height between stages to $\Delta V \sim$ 9-10 eV.

In order to trap positrons with a few tens of electron-volt energy, they must lose enough energy so that they do not exit the trap once they are reflected by the end potential barrier. The cooling mechanism employed in this type of traps is the inelastic collisions a positron undergoes with the buffer gas. The most efficient buffer gas to date is molecular nitrogen. It has a large electronic excitation cross section, as shown in figure 4.4, near the threshold for electronic excitation of the $a^1\Pi$ level of N_2 at 8.6 eV, while having a small cross section for positronium formation [72]. This feature is rather unique since the positronium formation threshold is below the lowest allowed inelastic electronic transition in most molecules [73]. From figure 4.4 one can deduce that trapping should be negligible for positrons with energy smaller than 8.6 eV.

At 11 eV positronium formation is as probable as electronic excitation, thus there is a $\sim$3 eV window for which efficient trapping can occur. Table 4.1 summarizes the possible reactions of a positron with a nitrogen molecule and their respective threshold energy.

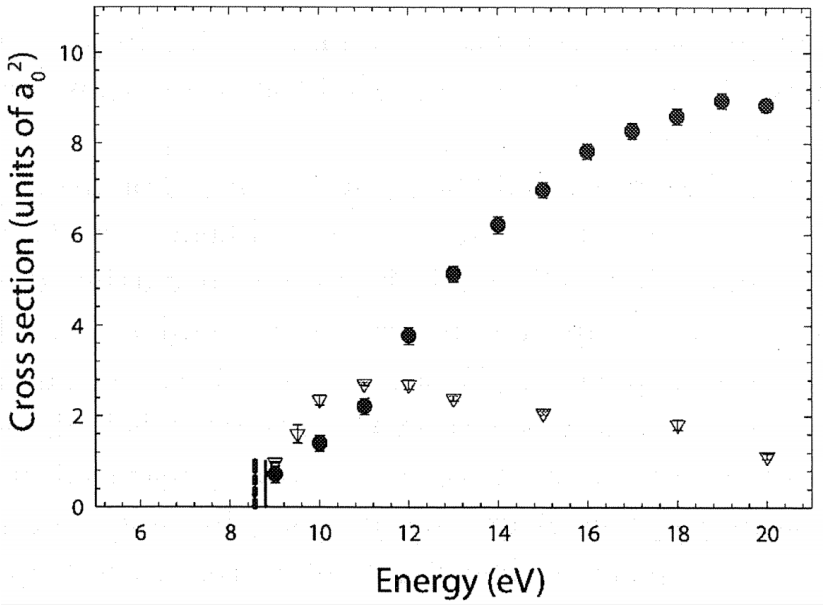

Figure 4.4: Cross sections in atomic units (a_0 is the Bohr radius) for positron impact excitation of the $a^1\Pi$ electronic state of N_2 ($\triangledown$) and positronium formation ($\bullet$). The dashed and solid vertical bars indicate the energy thresholds for electronic excitation and positronium formation, respectively. Figure reprinted from reference [72].

Positronium formation is an important positron loss mechanism since there is competition between electronic excitation and positronium production, between 9 eV and 11 eV. While an elevated nitrogen pressure can increase the trapping efficiency, positronium production is also more likely. Therefore maximizing the trapping rate entails the optimization of the nitrogen pressure and the electrostatic potential along the first and second stage.

The trapping efficiency is further reduced in beams with a large energy distribution. The least energetic positrons might not overcome the potential barrier formed by the first electrode of the first stage, while the most energetic positrons need to undergo more inelastic collisions without forming positronium, which is an unlikely occurrence.

When positrons collide inelastically with a nitrogen molecule, they are radially transported to the electrode's walls, where they annihilate. This is a critical loss mechanism and can be minimized by applying the rotating wall technique. The technique consists of subjecting the positrons to an inward transport by a rotating dipolar electric field, during accumulation, resulting in a lifetime of the same order of the annihilation lifetime (due to annihilation with the buffer gas) [74]. This technique is described in more detail in the following section.

Table 4.1: Positron interactions with a nitrogen molecule and respective threshold energy [72].

	Reaction	Energy threshold
Annihilation	$e^+ + N_2 \rightarrow N_2^+ + 2\gamma_{(511\,keV)}$	-
Elastic scattering	$e^+ + N_2 \rightarrow e^+ + N_2$	-
Rotational and vibrational excitation of N_2	$e^+ + N_2 \rightarrow e^+ + N_2^{rot/vib}$	rot ~ 1 meV, vib ~ 0.3 eV
Electronic excitation of N_2	$e^+ + N_2 \rightarrow e^+ + N_2^\star$	8.6 eV
Positronium formation	$e^+ + N_2 \rightarrow Ps + N_2^+$	8.8 eV
Ionization	$e^+ + N_2 \rightarrow e^+ + e^- + N_2^+$	15.6 eV

4.2.1 Rotating wall technique

In a buffer gas trap the positron lifetime is limited in the presence of the buffer gas that not only increases the annihilation rate, but also the radial transport suffered by a positron when colliding with a gas molecule. Furthermore, if one wishes to increase the trapping rate then a higher buffer gas pressure is needed, which in turn increases the cross field transport. Even if a Penning-Malmberg trap is operated at UHV, the lifetime is still limited by inherent electrostatic and magnetic field asymmetries that break the cylindrical symmetry and apply a torque on the particles, inducing radial expansion. It is possible to counteract these phenomena by applying the rotating wall technique.

A non-neutral plasma is a collection of charged particles whose self-generated electric fields play a significant role in the particle dynamics. Moreover, the collective interaction of these charges with one another gives rise to large potentials that screen out exterior static electric fields. This phenomenon arises when the plasma's Debye length (fundamental length scale),

$$\lambda_D = \sqrt{\frac{\varepsilon_0 k_B T}{nq^2}}\,, \tag{4.11}$$

is small compared to the plasma dimensions where k_B is the Boltzmann constant, T is the plasma temperature, and n its density.

The canonical angular momentum of a plasma, P_θ, and the mean-square radius, $\langle r^2 \rangle$, are related via

$$P_\theta = Nm\,(\omega - \Omega_c/2)\,\langle r^2 \rangle\,, \tag{4.12}$$

where N is the number of charged particles and ω is the rotational angular frequency (about the z-axis) independent of r, for a spatially uniform plasma [75]. For plasmas obeying the drift approximation, in which $\omega << \Omega_c/2$, the canonical angular momentum is negative. The application of a positive torque increases the canonical angular

momentum. Since P_θ is negative, the applied torque leads to a decrease of the magnitude of the angular momentum, and therefore a decrease of the plasma radius.
This is essentially the idea behind the rotating wall technique, in which the expanding plasma is radially compressed with the application of a torque in the same direction as its natural rotation; e.g. the azimuthal $\mathbf{E}\times\mathbf{B}$ drift due to the charges' radial electric field that results in a rotating frequency

$$f_E = \frac{nq}{4\pi\varepsilon_0 B}\,. \tag{4.13}$$

The technique can be implemented by rotating the electric field azimuthally at the plasma rotating frequency f_E. Since it is not practical to rotate the stack of electrodes, as well as the solenoid, a way of realizing this idea is by applying a sinusoidal potential, $V_{\mathrm{RW}}(t)$, to each sector of an azimuthally segmented electrode in quadrature,

$$V_{\mathrm{RW}}(t) = V_r \sin(\omega_r t + \psi_i)\,, \tag{4.14}$$

where ω_r is the rotating wall angular frequency, V_r the amplitude and ψ_i takes the values 0°, 90°, 180° and 270° for each segment. If the applied torque is equal to the total torque resulting from trap asymmetries and the interaction with gas molecules, then the plasma reaches a steady state. More interestingly, if one applies a stronger torque then the plasma is compressed and high density plasmas can be produced. The torque applied to the plasma by the rotating wall, τ_{RW}, heats the plasma by doing work on it [76]:

$$P_{\mathrm{H}} = \omega_{\mathrm{RW}}\tau_{\mathrm{RW}}\,. \tag{4.15}$$

If the confining magnetic field is large, then the emission of cyclotron radiation is a sufficient cooling mechanism, as the cooling time goes with the inverse of the square of the magnetic field:

$$\tau_c = \frac{3\pi\varepsilon_0 m^3 c^3}{e^4 B^2}\,, \tag{4.16}$$

where m is the mass of the charged particles.

In the case of a buffer gas trap, the magnetic field is typically 300 G to 400 G, hence this cooling mechanism is very slow (2887 s to 1624 s) which would turn the rotating wall into a heating source rather than a compression mechanism. As such, a cooling gas with a large vibrational excitation cross section can be inserted into the trap to counteract the heating. In spite of being a good buffer gas, the vibrational and rotational excitation cross sections of N_2 are very small, making it a poor cooling gas (see [77] for a comparison of the positron cooling-rate between N_2, CF_4 and CO). An additional cooling gas, in which the positron annihilation lifetime is long (compared to the typical accumulation time) while the cooling time is short, can be introduced to complement the cooling of the buffer gas. Table 4.2 shows potential candidates for cooling gas. One can compare the positron annihilation time with the cooling time for each gas species and notice that the cooling time of N_2 is two orders of magnitude higher than the other gases. SF_6 and CF_4 are the preferred gases for positron cooling in a buffer gas trap at room temperature due to their large vibrational excitation cross section [73].

Table 4.2: Positron annihilation time (τ_a) and cooling time (τ_c) for some molecular gases at 2.7×10^{-8} mbar. The trapping efficiencies normalized to N_2 (ε) are shown, as well as the maximum measured compression rates $\dot{n}/n_{max}$ using the rotating wall technique. This table is reproduced from [71].

Gas	τ_a (s)	τ_c (s)	ε	$\dot{n}/n_{max}$ (s^{-1})
SF_6	2190	0.36	0.07	10
CF_4	3500	1.2	-	10
CO_2	3500	1.3	0.16	4
CO	2400	2.1	0.68	<0.2
N_2	6300	115	1	<0.2

A rotating electric field was first implemented to counteract the radial expansion of an ion plasma (10^9 Mg^+) [78]. A steady-state balance between the radial expansion and the heating was maintained showing that a plasma can be confined indefinitely (weeks). By increasing the drive frequency, a compression up to 20% of the Brillouin density limit (maximum plasma density, $n_B = \varepsilon_0 B^2/2m$) was demonstrated to be feasible. The same technique was later applied to electron [79] and positron plasmas [80], and it was discovered that compression was more efficient when the rotating wall frequency is coupled to the plasma Trivelpiece-Gould modes (see [81] for a theoretical description of these modes).

Danielson and Surko discovered a new regime coined "strong-drive" in which compression is achieved in a broadband of rotating wall frequencies, without the need to couple to these plasma modes [82]. Unlike the "weak-drive" case in which compression is observed for discrete frequencies that correspond to the plasma modes, the "strong-drive" mechanism works above a minimum V_{RW} amplitude and strong compression is achieved over a wide range of frequencies. The plasma rotation frequency, f_E, follows closely the applied rotating wall frequency. This method is extremely flexible as it allows to tune the plasma density by choosing the appropriated frequency. Nowadays the "strong-drive" rotating wall is ubiquitous in electron and positron plasma experiments that apply the rotating wall technique.

The studies described in this thesis were not performed with a positron plasma, but in the so called single particle regime, using a positron cloud with low density such that the particles are assumed to be non-interacting. In this regime, the principle of the rotating wall technique is different from the one applied in the plasma regime. Cassidy *et al.* [83] and Greaves and Moxom [84] have successfully compressed a positron cloud with a rotating electric field in which the compression occurs for rotating wall frequencies centered on the axial bounce frequency, ω_z, in an harmonic well. Isaac [85, 86] modeled the effect of an axially asymmetric rotating dipole electric field on the motion of a charged particle and took into account the cooling mechanism of the inserted gas by introducing a Stokes viscous drag term, $\mathbf{F} = -\kappa\mathbf{v}$, where κ is a drag coefficient. The model adds a rotating dipole term to the quadratic potential of an

ideal Penning trap

$$\Phi_r = \frac{m}{q} V_r z r \cos(\theta + \omega_r t)\,, \tag{4.17}$$

where ω_r is the rotating wall angular frequency, V_r the amplitude, that acts by coupling the axial bounce, ω_z, to the magnetron motion, ω_m. Greaves and Moxom reported that a symmetric rotating wall was not able to compress a positron cloud, but compression was successful with an axially asymmetric rotating field [84]. The proportionality on z introduces this asymmetry. The solution of the equations of motion suggest that this system is equivalent to a damped harmonic oscillator with a single driving frequency ω_r - ω_m. The rotating wall then acts by coupling the magnetron motion to the bounce motion (z). By driving the latter it is possible to decrease the magnetron radius, where the compression rate, Γ, is given by

$$\Gamma = \frac{\kappa}{4}\left(1 - \sqrt{\frac{(\omega_r - \omega_0)^2}{\delta^2 + (\omega_r - \omega_0)^2}}\right)\,, \tag{4.18}$$

where $\omega_0 = \omega_z + \omega_m$ and δ, the frequency response width, is linearly dependent on the applied rotating wall amplitude:

$$\delta = \frac{V_r}{\sqrt{(\omega_+ - \omega_m)\,\omega_z}}\,. \tag{4.19}$$

The oscillator is in resonance for the drive frequencies $\omega_r = \pm\omega_z + \omega_-$, with $+\omega_z$ corresponding to compression of the positron cloud and $-\omega_z$ to expansion.
The lower sideband frequency, $\omega_r = \omega_z - \omega_m$, is inactive as it does not produce a resonant response. Maximum compressions is achieved when $\omega_r = \omega_0$.

A sinusoidal potential applied to an electrode with a finite number of segments can produce an approximate rotating dipole potential. The potential of a four segment rotating wall can be obtained by solving the Laplace equation $\nabla^2\Phi = 0$. It can be shown [87] that the solution is of the form

$$\Phi(r,\theta) = \frac{1}{2}a_0 + \sum_{n=1}^{\infty}\left(\frac{r}{r_0}\right)^n \left(a_n \cos(n\theta) + b_n \sin(n\theta)\right)\,, \tag{4.20}$$

where a_n and b_n are the coefficients of the Fourier series approximation to the boundary conditions $\phi(r_0,\theta)$:

$$a_n(t) = \frac{q}{\pi}\int_0^{2\pi} V_{RW}(\theta,t)\cos(n\theta)d\theta\,, \tag{4.21}$$

$$b_n(t) = \frac{q}{\pi}\int_0^{2\pi} V_{RW}(\theta,t)\sin(n\theta)d\theta\,. \tag{4.22}$$

The dipolar nature of the electric potential produced by the rotating wall technique can be visualized in figure 4.5.

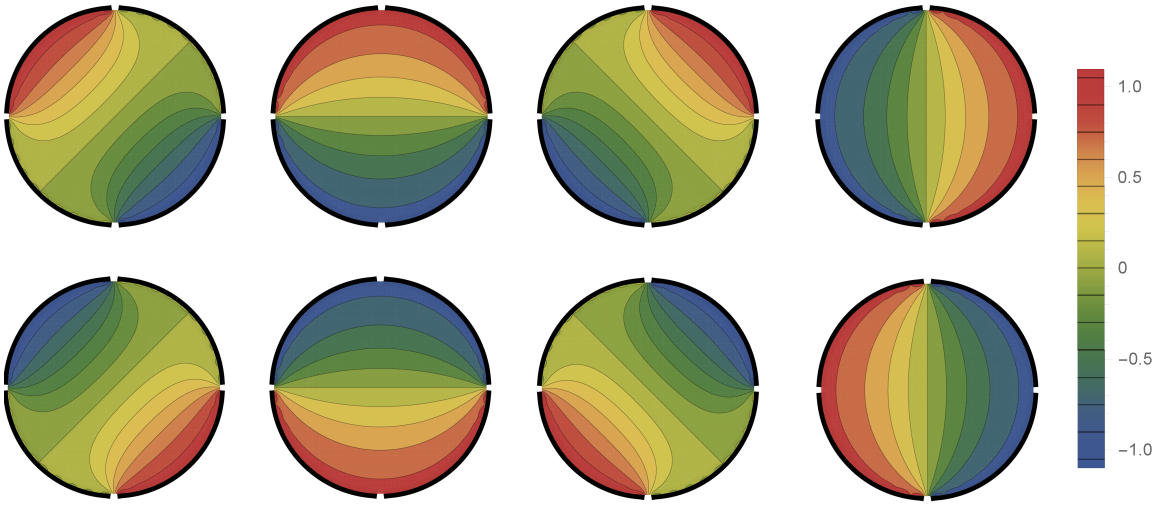

Figure 4.5: Dipolar electric potential produced by a four segment rotating wall for different times. The equipotential lines are shown. The sinusoidal potential applied to each electrode segment is offset by 90°.

4.3 Apparatus description

The positron accumulator developed during this thesis was based on Swansea's positron accumulator [88]. Unlike Surko's trap, the first and second stage are separated from the third stage - see figure 4.6. This separation allows for an extra pumping station between stage 2 and 3. Surko's trap has two pumping stations: one before the first stage and another after the third stage. The positron trapping region is then reduced to the two first stages with higher nitrogen pressure, $\sim 10^{-3}$ mbar and $\sim 10^{-4}$ mbar respectively, while the third stage functions as a positron accumulator with a much lower pressure of $\sim 10^{-7}$ mbar. The addition of a pumping station allows the use of smaller radius electrodes, compared to Surko's third stage electrodes, making the apparatus more compact and less expensive given that the vacuum vessels and solenoids are smaller. A more detailed description of the vacuum system is given in 4.3.1.

The first electrode set forming the first stage, comprises 15 cylindrical electrodes of length 24 mm and 16 mm inner diameter. One of the electrodes contains a Teflon inlet (for electrical insulation) for the buffer gas, see figure 4.7, which is admitted into the center of the first stage via an stainless steel tube from the vacuum flange. The second set (second stage) is comprised of 5 cylindrical electrodes of length 49 mm and 41 mm inner diameter. The fourth electrode of the second stage is divided in two and one of the halves is divided into four segments, allowing the implementation of the rotating wall technique. A close-up of the rotating wall electrode is shown in figure 4.7. The cooling gas is inserted from the vacuum flange in cross II.

After being trapped in the second stage, the positrons are transported and stacked in the third stage, where the lifetime is longer. For that purpose, the third stage was designed to bear two separate harmonic wells, each with its own rotating wall. In the stacking technique the positrons are first captured in the first well, after being transported from the second stage, and then are transfered to the second well.

This procedure is then repeated multiple times until the desired number of accumulated positrons is achieved. This scheme can in principle minimize possible perturbations provoked by the re-trapping and merging of the new positrons with the ones already present in the well.

The set of electrodes comprising the third stage contains two 49 mm long electrodes at each edge of the set, and twelve 18.4 mm electrodes all with 41 mm inner diameter. The dimensions of these electrodes are chosen so that each harmonic well is formed with five identical electrodes with an aspect ratio (length/radius) of 0.9. Madsen [89] studied various electrode dimensions and configurations with the goal of minimizing the potential deviation from an harmonic well. He reported that this aspect ratio is a good compromise between the harmonicity of the well and the number of electrodes.

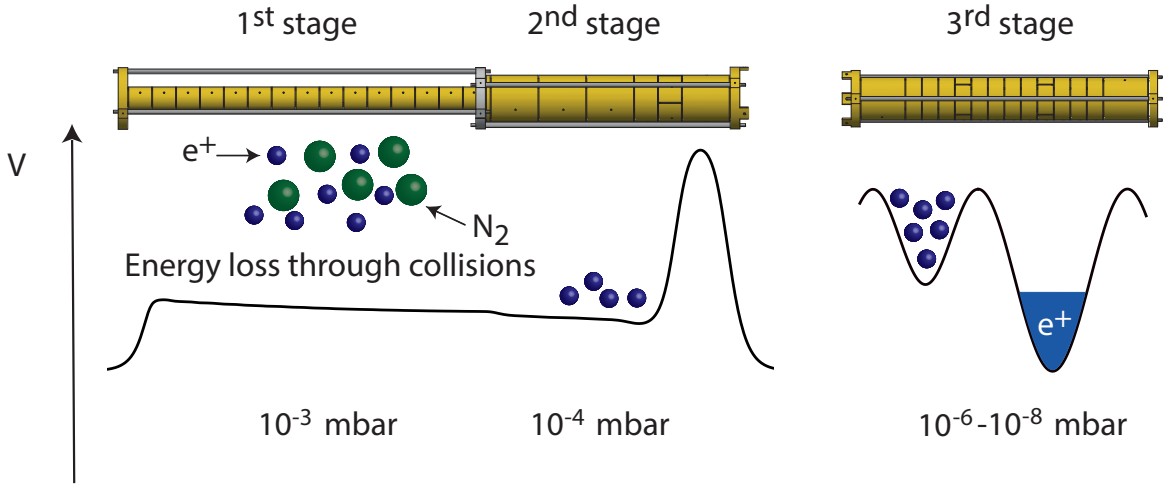

Figure 4.6: Illustration of the accumulation technique. The positrons coming from the LINAC enter the buffer gas trap and lose energy by inelastic collisions with the buffer gas (N_2). After undergoing a few collisions they become trapped in the first stage. Further collisions with the buffer gas and cooling gas (SF_6) are needed to confine the positron in the second stage, where the pressure is lower. Once the positrons are trapped in the second stage they can be transported to the first well in the third stage, and then stacked in the second well. The procedure is repeated until the number of desired positrons are confined in the lowest pressure region.

The aluminum grade (6082) electrodes are gold-plated to reduce the electric patch effects [90]. Because each electrode can have a different bias voltage, the electrodes are electrically insulated by 2 mm radius sapphire balls which fit into 0.5 mm indents machined into the electrodes. These balls also ensure a precise distance between each electrode.

The first and second stage electrodes are inserted in one solenoid, and the third stage in another one. Several coils are placed along the trap to guarantee a smooth magnetic transport. A more detailed description of the magnetic field along the trap is given in 4.3.2.

Eight different voltages are applied in the first and second stages: three in the first stage and five in the second stage; the remaining electrodes in the first stage are biased by potential dividers (resistor chain, 1 MΩ each) that provide successively lower

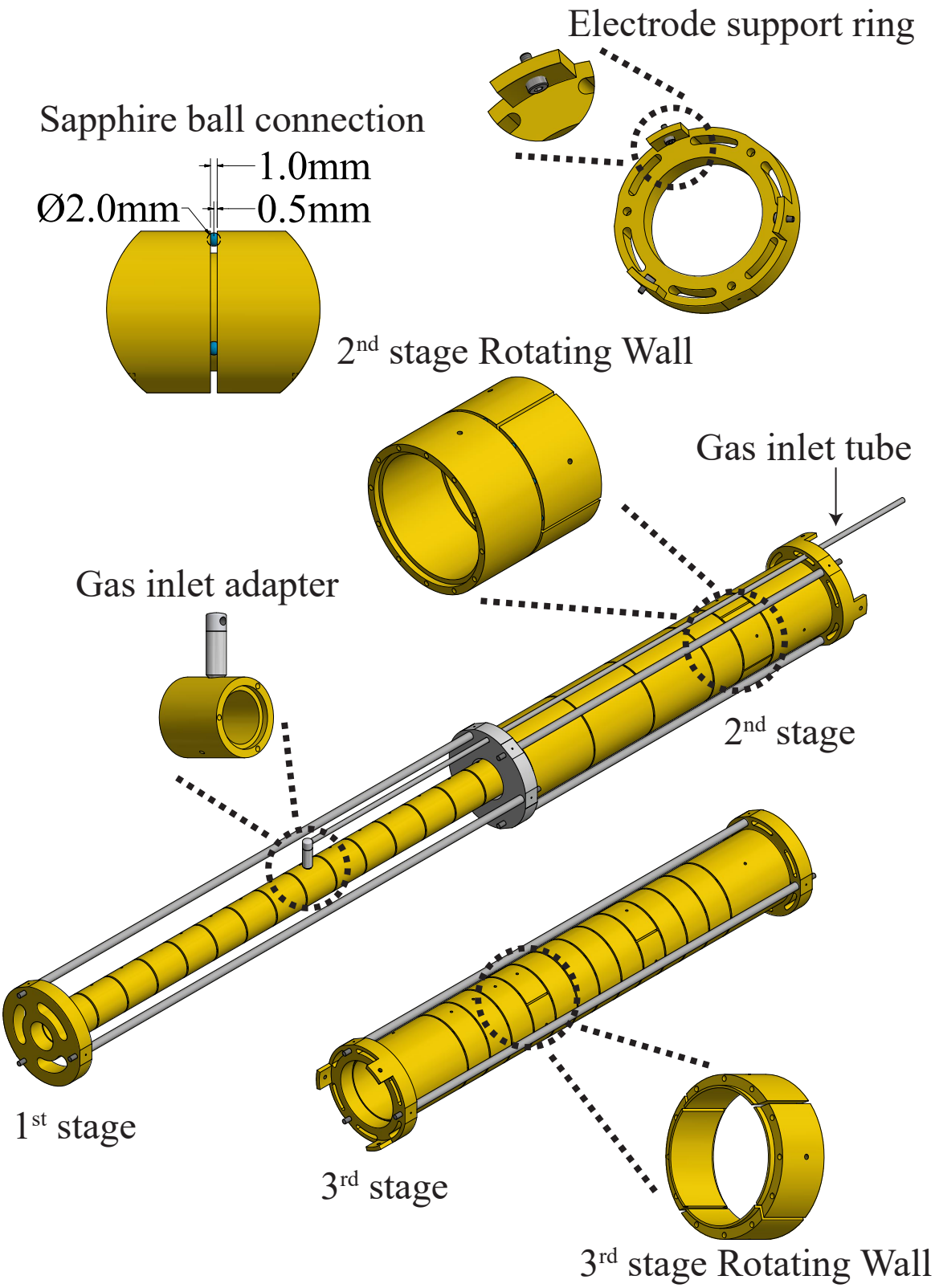

Figure 4.7: Detailed view of the buffer gas trap electrodes.

voltages in equal incremental steps forming a potential ramp. Three fast switches are used to rapidly increase or decrease the potentials of the last electrode of the second stage (1.75 V/ns fall time), and the first (0.23 V/ns rise time) and last electrode (0.96 V/ns fall time) of the third stage. The axial electrical potential of a typical trapping experiment is shown in figure 4.8, as well as the applied magnetic field.

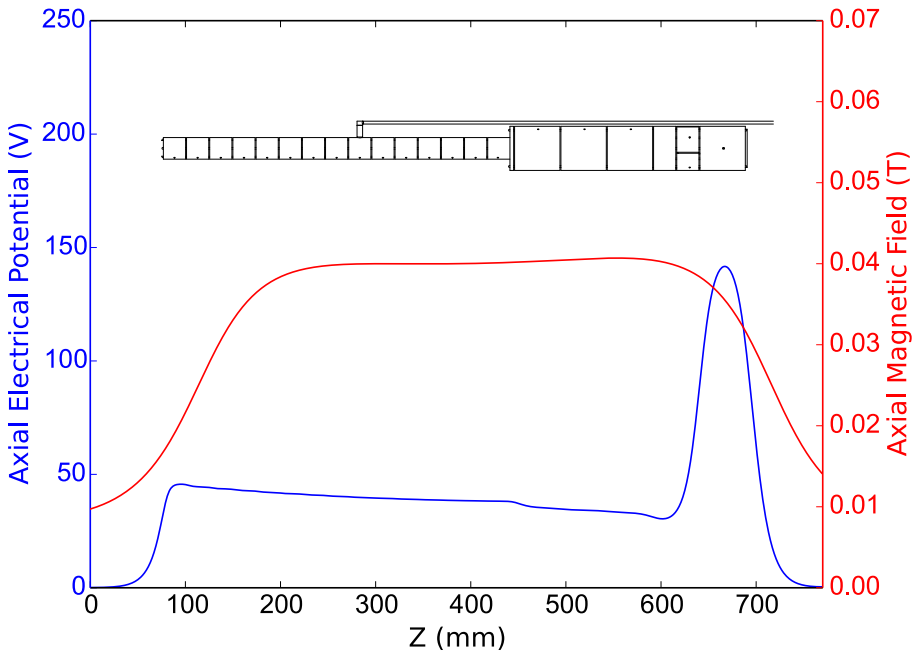

Figure 4.8: The axial electrical potential and applied magnetic field in the first and second stage. The electric potential was computed using SIMION.

4.3.1 Vacuum System

The vacuum system is a key ingredient in any experiment that aims to study antimatter. However, in this case the interest is not only to minimize the pressure inside the vacuum vessels - to extend the lifetime of the positrons, but also to manipulate the pressure along the trap since the trapping and cooling mechanisms rely on the interactions of positrons with specific gases. As previously described, this trap consists of three stages with different pressures, in which the buffer gas is added in the first stage and the cooling gas is added in the second and third stages. The latter requires a much lower pressure to allow a large storage time. Downstream of the accumulator there are two extra pressure stages with the goal of reducing the pressure to $\sim 10^{-9}$ mbar so that the following experimental apparatus (the ANTION chamber) is not contaminated by the added gases, allowing for a higher quality vacuum environment.

In order to be able to achieve different pressure gradients, the first and second stages are pumped by two *Oerlikon* MAG W 600 turbomolecular pumps (pumping speed of 550 l/s for N_2), backed by an *Edwards Vacuum* XDS10 scroll pump. The small diameter electrodes in the first stage, compared to those of the second stage, result in two distinct pressure regions when the buffer gas is admitted to the system.

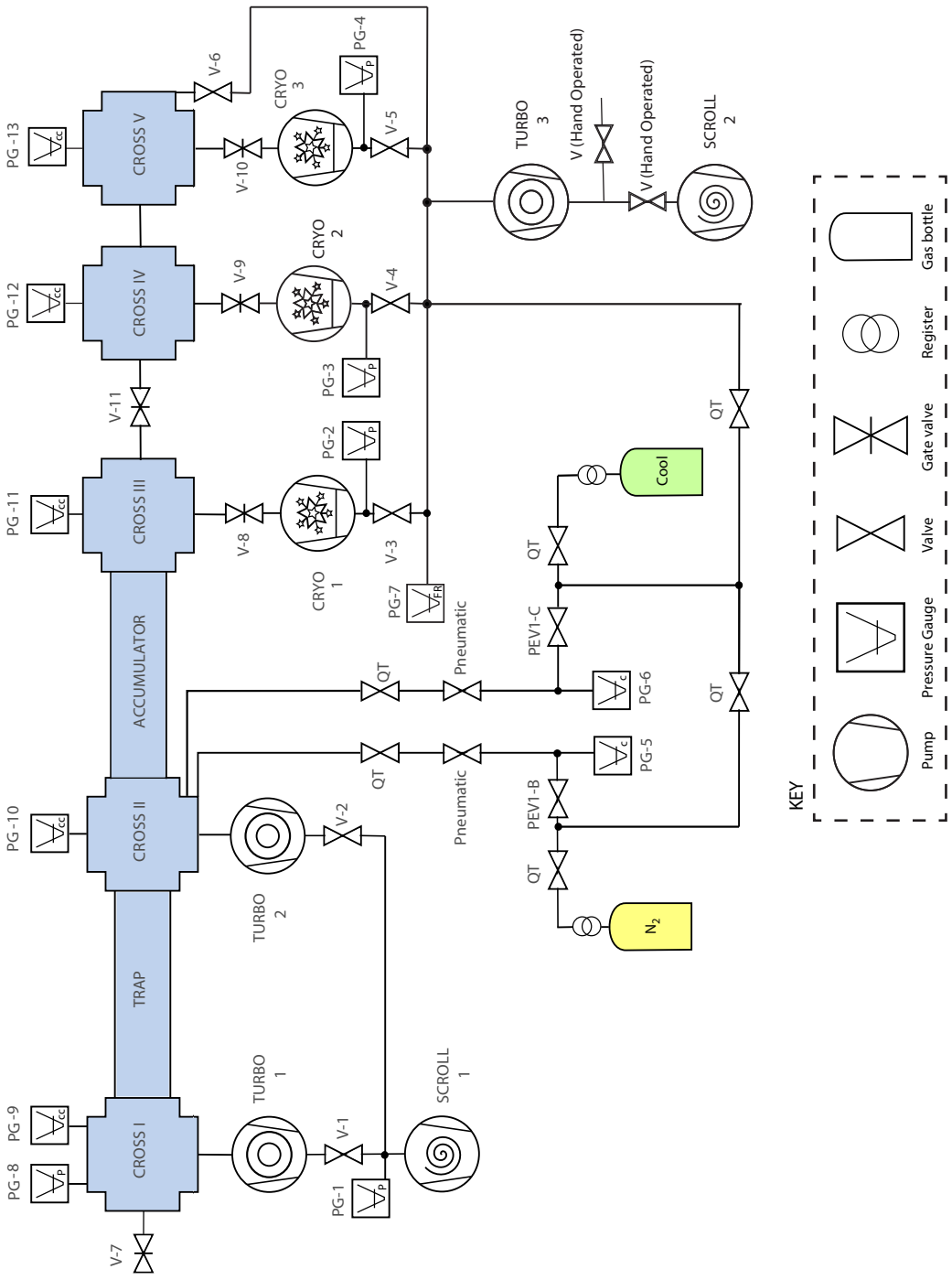

Figure 4.9: Diagram of the vacuum system. Key: PG - Pressure gauges numbered from 1 to 13, marked with its corresponding type: C - capacitance gauge; CC - cold cathode gauge; FR - full range gauge; P - Pirani gauge; valves: V - pneumatic valve; QT - quarter turn valve; PEV1 - piezo-electric valves for the buffer gas (B) and the cooling gas (C).

The first stage has a cross sectional area of 201 mm^2, while the second stage cross sectional area is 1320 mm^2. The cross sectional area of the third stage is identical to the second stage and in the downstream crosses there are 3 cryopumps powered by two *Sumitomo* compressors. An *Edwards* 300 turbopump functions as a rough pump for the cryopumps, and also pumps the buffer and cooling gas line. A summary of the pumps used in the buffer gas trap can be seen in Table 4.3. Figure 4.9 shows a diagram of the vacuum system.

The pressures are monitored by thirteen *Pfeiffer Vacuum* gauges: capacitance gauges work at high range pressures from 10^{-2} mbar to 10^{3} mbar, Pirani gauges are used for mid range pressures from 10^{-4} mbar to 10^{2} mbar, Penning (cold cathode ion) gauges operate at a lower range from 10^{-11} mbar to 10^{-3} mbar, and full range gauges that combine the pirani and cold cathode gauges. The gauges are read by three MaxiGauges, that in turn are connected to a *National Instruments* module (see subsection 4.3.4 for further details) in which a LabView program is used to monitor and act on the state of the valves according to the pressure in the vacuum vessels

The buffer and cooling gases are introduced in the trap through a system of pipes and valves. The flux is regulated by *Key High Vacuum* PEV-1 piezoelectric valves remotely controlled by a Labview PID software. This mechanism is described in more detail in subsection 4.3.4.

Table 4.3: Summary of the vacuum pumps used in the buffer gas trap, their location and pumping speeds for N_2.

Pump	Manufacturer	Model	Location	Pumping speed (l/s)
Turbo 1	Oerlikon Leybold	MagW 600	Cross I	550
Turbo 2	Oerlikon Leybold	MagW 600	Cross II	550
Cryo 1	SHI Cryogenics	Marathon CP-8	Cross III	1500
Cryo 2	SHI Cryogenics	Marathon CP-8	Cross IV	1200
Cryo 3	SHI Cryogenics	APD 8	Cross V	1500
Turbo 3	Edwards	nEXT300D	Back line	300

Since the pressure gauges are directly connected to the crosses, it is not possible to measure the pressures in each stage of the trap, yet these values are essential parameters to optimize the trapping rate or lifetime. An estimation of the pressure can be done by using simple equations that resemble Kirchhoff's circuit laws, in which the voltage difference is replaced by the pressure difference and the resistance is given by the inverse of the conductance, C (l/s). For these computations a molecular flow regime is assumed since the pressure is expected to be smaller than 10^{-3} mbar, so the conductance is independent of the pressure and is determined by the geometry of the system. The conductance for air at 20° C, in some typical vacuum elements, is given by [91]

Aperture	$C = \frac{\pi D^2}{4}\,,$
Long pipe	$C = \frac{12.1 D^3}{L}\,,$
Short pipe	$C = \frac{11.6 A}{1 + L/D}\,,$

where D the pipe diameter and L the length, both in centimeters. The total conductance C_T for n vacuum components connected in series is given by

$$\frac{1}{C_T} = \frac{1}{C_1} + \frac{1}{C_2} + \ldots + \frac{1}{C_n}\,. \tag{4.23}$$

If a pump is present and connected to the system by an aperture with conductance C, then the effective pumping speed, S_{eff} is given by

$$\frac{1}{S_{\text{eff}}} = \frac{1}{S} + \frac{1}{C}\,, \tag{4.24}$$

where S is the nominal pumping speed (l/s). The throughput (mbar l/s) - quantity of gas per unit time, between two vacuum vessels, one connected to a pump, can be computed as

$$Q = C \times (P_1 - P_2) = P_2 \times S_{\text{eff}}\,, \tag{4.25}$$

where P_1 and P_2 are the pressures in each vessel.

Assuming the pressure in the center of the first stage is 10^{-3} mbar and using the equations given above, the pressure along the accumulator can be estimated and is presented in table 4.4. The measured pressures in each cross are shown as well, for comparison.

Based on the table 4.2 one can estimate the positron lifetime in all three stages. For the pressures shown in table 4.4, and assuming only nitrogen is present, the lifetime in the first stage should be 0.2 s, in the second stage 2.1 s and in the third stage 24 s.

A Residual Gas Analyzer (RGA) of *Stanford Research Systems* is located in cross V. This device characterizes the vacuum environment by detecting the gases present in the vacuum chamber, as well as their pressure. The working principle is based on a mass spectrometer, in which gas molecules are ionized and mass filtered before being detected. It can also be used as a leak detector in combination with helium.

4.3.2 Magnetic Field

The positrons are radially confined by the magnetic field created by the solenoids surrounding the electrodes, and guided by the coils positioned along the trap. There are seven coils and three solenoids. Four coils are positioned on either side of the chambers that precede stages 1 and 3. After the third stage, a large coil encases the narrow pumping restriction in order to compress the positron beam, avoiding the annihilation of positrons in the case the beam is too large to fit inside the vacuum tube.

Table 4.4: Estimated and measured pressure along the accumulator when the buffer gas is present.

Location	Calculated pressure (mbar)	Measured pressure (mbar)
Cross I	1×10^{-5}	1×10^{-5}
1^{st} stage	1×10^{-3}	-
2^{nd} stage	8×10^{-5}	-
Cross II	9×10^{-6}	5×10^{-6}
3^{rd} stage	7×10^{-6}	-
Cross III	2×10^{-7}	1×10^{-7}
Cross IV	6×10^{-9}	1.8×10^{-9}
Cross V	2×10^{-10}	3×10^{-10}

Two other coils were placed at the end of the trap to ensure a good transport to the following apparatus, the first of which also contributes to the compression of the beam in the pumping restriction. The first, second and third stages were inserted inside two solenoids which are set at a higher magnetic field. The axial component of the magnetic field along the trap was computed in *Mathematica* and can be seen in figure 4.10.

The coils and solenoids are powered by *Delta Elektronika* 1500 W and 3000 W DC power supplies, which can be remotely turned on or off, and are interlocked with the water cooling system that refrigerates the coils/solenoids.

The transport of positrons along the accumulator can be considered adiabatic as the changes in the magnetic field are very slow compared to the period of the cyclotron motion (10^{-9}-10^{-10} s).

4.3.3 Detection and diagnostics

To understand what is happening inside the buffer gas trap and to characterize the positron beam, it is essential to implement some detection and diagnostic tools. Scintillator detectors were placed in convenient locations to detect the γ-rays that result from the annihilation of positrons with electrons. This is useful to estimate the number of trapped positrons, as well as the number of positrons that enter the trap and are not lost due to magnetic mirroring. A microchannel plate detector (MCP), in cross IV, combined with a phosphor screen and a camera is installed to provide useful information about the shape of the positron beam as well as the energy distribution. Five retractable stainless steel plates with three circular apertures with different diameters, placed in the remaining crosses, are used for alignment purposes. Although not employed during this thesis, the plates also allow the use of the Hole Masking technique, [92], in which the radial width of the positron beam can be determined with a

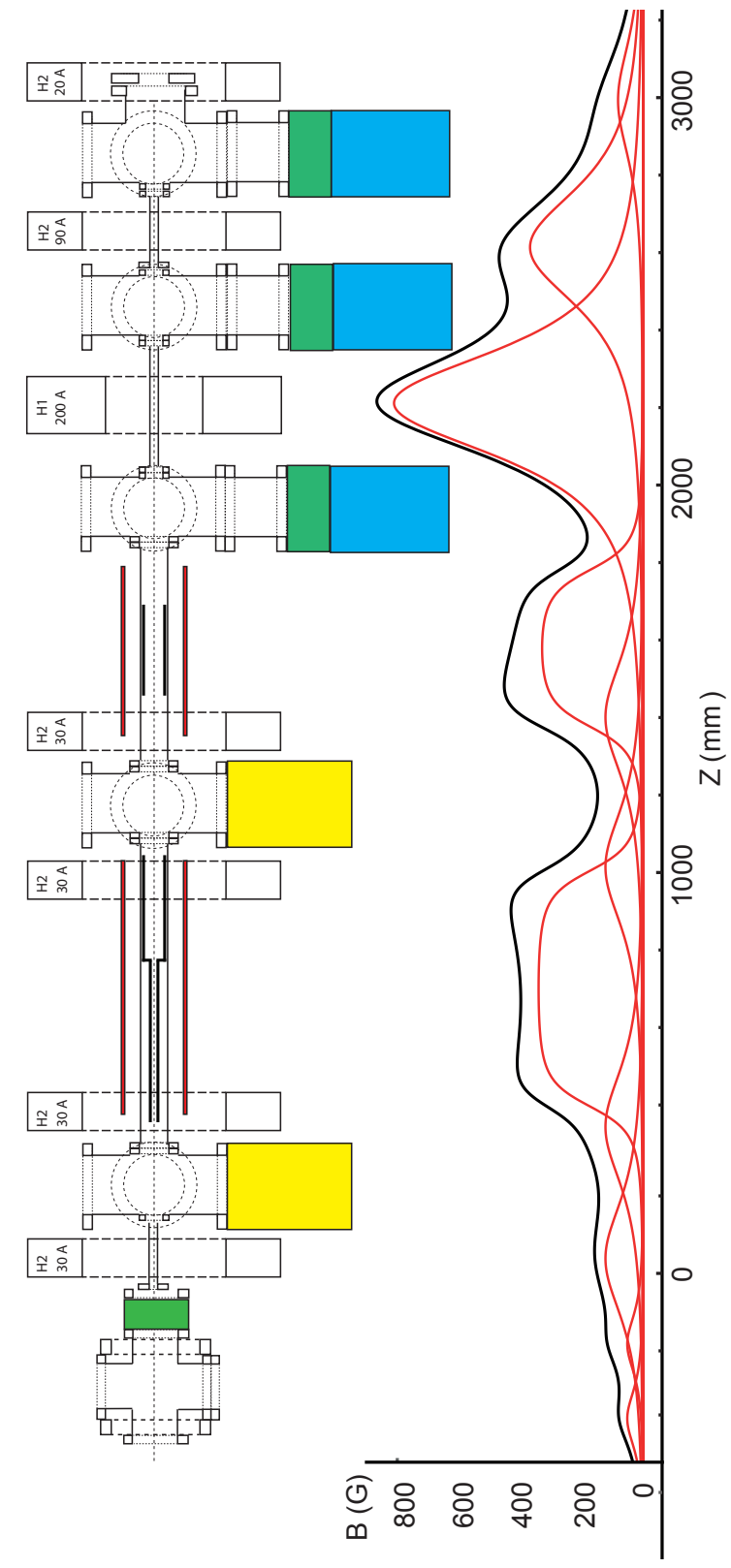

Figure 4.10: Schematic overview of the vacuum chambers and accumulator electrodes together with the magnetic coils (H1 and H2) and solenoids. The black solid line corresponds to the total magnetic field and the red solid lines the magnetic field for each coil, using the currents displayed.

plate with a circular aperture in combination with a scintillator detector. This method can be useful in determining the size of the cloud before and after the first and second stages, without the need for additional expensive MCPs. The plate in cross I is also used to block the electrons that travel from the LINAC.

Caesium Iodide detectors

Scintillation detectors are based on the luminescence property of certain materials when struck by a nuclear particle or radiation. The light signal can be converted into an electrical pulse by a photomultiplier or a photodiode. This type of detectors are suited for the detection of γ-rays resulting from the annihilation of a positron. For the experiments performed with the buffer gas trap two 40 mm×50 mm caesium iodide detectors doped with thallium, CsI(Tl), were employed along with PIN photodiodes and preamplifiers. Because of their large light output (56 γ/keV [93]) they are extremely suitable for the detection of γ-rays.

The CsI(Tl) crystal is a slow scintillator as its decay constant is of the order of a few microsenconds, while the pulse length can be a few nanoseconds [93]. This is not a problem for the experiments realized with the buffer gas trap, when the aim is to know the number of trapped positrons and the time resolution is not an issue. The detector was calibrated in order to know the correspondence of the detected signal to number of annihilated positrons. This was done by cross calibrating the signal measured by the CsI detector with the charge of a positron beam impinging on an aluminium plate, or valve, measured with the assistance of a Amptek A250CF CoolFET charge sensitive preamplifier. This preamplifier has a high sensitivity of 4 V/pC. The fraction of secondary electrons, liberated upon the positron beam impact on the plate, was estimated by applying a positive bias (+40 V) to the plate while measuring the preamplified signal. The calibration was performed for the CsI detector on top of the cross containing the MCP, yielding

$$\mathrm{N}(1\,\mathrm{V}) = (4.6 \pm 0.6) \times 10^5\ e^+.$$

Microchannel Plate detector

A microchannel plate is an electron multiplier that outputs a two dimensional electron image, preserving the spatial resolution of the incoming particles/radiation while having a gain of more than 10^7. It can either be used as an imaging device when used in combination with a phosphor screen, or just as a particle/radiation detector when the current is measured.

The plate consists of an array of millions of lead glass channels fused together. Both faces of the plate are coated with a metal, nichrome or inconel, so that an electric field can be applied along the channels which are semi-conducting. Each channel is fundamentally a continuous dynode. When an incident particle strikes a channel wall, secondary electrons are emitted and accelerated by the applied electric field, thus provoking an electron avalanche upon impact with the channel wall. This process generates several thousand electrons depending on the MCP's gain, which in turn depends on the potential difference between the front and the back of the MCP and

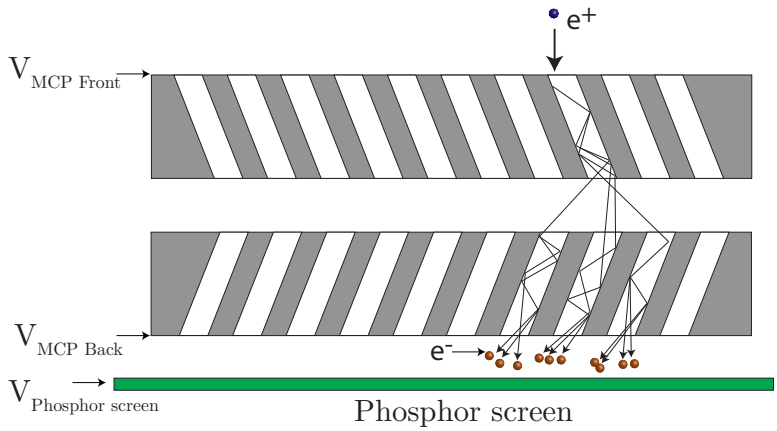

Figure 4.11: Schematic drawing of the operation of a microchannel plate detector in combination with a phosphor screen.

the length to diameter ratio of the channel, as well as the incident particle impact energy. The channel structure preserves the incident beam profile, providing a high spatial resolution limited by the channel dimensions and spacing (usually of the order of 10 μm). Moreover, MCPs are immune to magnetic fields of this order of magnitude, and have a short response time (<100 ps) [94]. Figure 4.11 shows a schematic drawing of the operation of a MCP.

The MCP is a *Chevron*™ assembly with an active area of 40 mm diameter and 10 μm pore size, purchased from *Photonis USA*. The gain can be as high as 10^7. The detector is combined with with a P20 phosphor screen that emits visible green light (peak at 555 nm) with a short 80 μs decay time. The assembly is controlled by three voltages: the voltage applied to the front of the MCP controls the positrons' impact energy that influence the MCP's gain, the bias applied to the back of the MCP controls the gain directly and, finally, the bias applied to the phosphor screen guides the electrons into it leading to the emission of photons. The images formed on the phosphor screen are reflected by a mirror placed at 45°. A 12 bit CCD low noise cooled camera (pco.1300 camera) placed outside the vacuum takes pictures of the phosphor screen. A drawing of the MCP assembly is presented in figure 4.12.

A 90% transparency grid is located in front of the MCP providing a flat electric field in front of the input surface. It also allows the application of a retarding potential converting the MCP into a retarding potential analyzer.

4.3.4 Measurement and Automation

To realize experiments with the buffer gas trap, a precise control of the buffer and cooling gas pressures is required, in addition to the manipulation of the potentials applied to the electrodes and the timing and sequence of events. Furthermore, since the buffer gas trap will be used by the GBAR collaboration at CERN, it requires a high level of automation and should be remotely operated during beam time, as people cannot access the experimental zone. For that reason, *National Instruments* hardware modules were employed to control and monitor the buffer gas trap apparatus, as well as its Labview programming language. The kernel of the hardware and software control

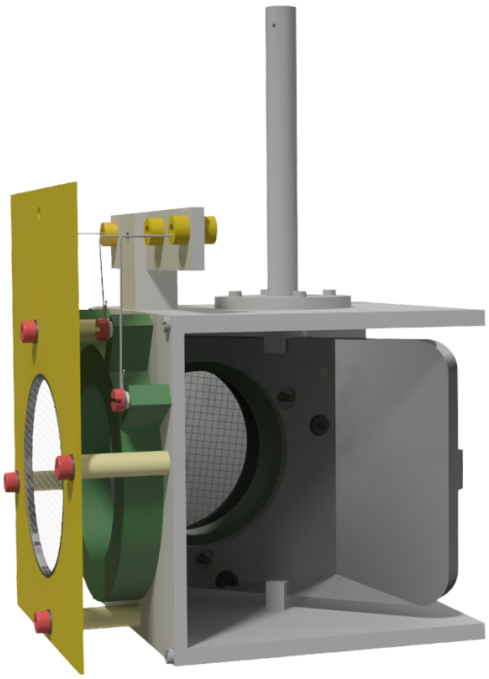

Figure 4.12: Drawing of the MCP assembly including the MCP holder (green), which is portrayed thicker for clarity, a grid mount in yellow and a mirror with 45°orientation. The manipulator is connected to a retractable linear drive.

is a PXI chassis that is connected to two CompactRIOs and several PXI modules. A CompactRIO Controller includes a Real-Time processor for communication and signal processing, and an FPGA (Field Programmable Gate Array) for implementing high-speed control. The first one called CompactRIO I, controls and monitors all hardware related to the vacuum; the second - CompactRIO II, is responsible for the control of the coils and solenoids, the water cooling interlocks, and the control and monitoring of the amplifiers that supply the electrodes.

CompactRIO I - Vacuum

The pressure in several points of the buffer gas trap is an essential parameter for the experiments, as it influences the positron annihilation rate and cooling time. As such the pressure is monitored closely by several *Pfeiffer Maxigauge* controllers that can also remotely turn on/off the pressure gauges. The vacuum valves, scroll pumps, cryopumps and helium compressors can also be remotely controlled and monitored, with the exception of the scroll pumps. The control of the valves is interlocked with the Maxigauge relay system so that one can only open a valve if certain pressure conditions are met. These criteria are software encoded. The control and monitoring is done by several modules belonging to the CompactRIO I.

Buffer and cooling gas PID system

The amount of buffer gas and cooling gas present in the trap is controlled by a simple PID (Proportional Integral Derivative) algorithm provided by LabView that consists

on a control loop feedback mechanism. This algorithm varies the bias applied (NI 9260 module) to the piezo-electric valves (here named PEV1-A and PEV1-B corresponding to the buffer and cooling gas valves) in order to bring the system pressure close to the desired one. The feedback is given by pressure gauges P5 (buffer gas) and P6 (cooling gas) that are monitored every second.

The PID controller continuously calculates an error value $e(t)$, which corresponds to the difference between the desired and the measured pressure, and applies a correction based on proportional, integral, and derivative terms.

$$V(t) = Pe(t) + I\int_0^t e(\tau)d\tau + D\frac{de(t)}{dt} \tag{4.26}$$

where P, I and D denote the proportional, integral and derivate coefficients. The proportional coefficient, P, accounts only for the difference between the desired pressure and the present values of the error. The controller response is then proportional to the error, being faster with a higher proportional gain. However, large gains can also lead to instabilities. The integral coefficient, I, accounts for past values of the error such that the integral of the error accumulates over time. For example, if the current output is not sufficiently strong, the controller will respond by applying a stronger action. This term is responsible for applying slow changes. Finally, the derivative coefficient, D, is multiplied by the rate of change of the error over time, allowing a faster response to rapid changes. This term helps in minimizing the overshooting by acting quickly as the pressure approaches the set point value.

The front panel of the PID program is shown in figure 4.13. The PID coefficients were varied until an optimal setting was achieved.

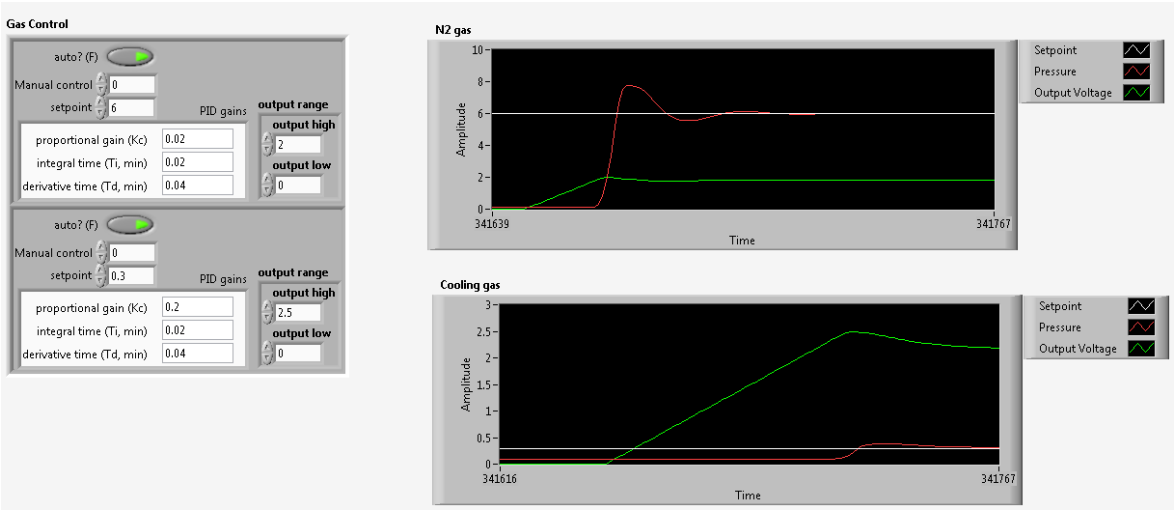

Figure 4.13: The front panel of the LabVIEW program that monitors and adjusts the buffer and cooling gas pressure. It allows for two operation modes: manual (auto OFF) in which the pressure is manually set, and automatic (auto ON) where the PID system adjusts the pressure to the desired one. The voltage range applied to the piezo-electric valves can be limited to prevent overflowing the system with gas. Two plots show the requested pressure, the actual pressure and the output voltage as a function of time for the buffer and cooling gas.

CompactRIO II - Electrodes, Coils and Water

Several modules in the CompactRIO II are used to control or monitor the electrodes, coils and solenoids, and the water flow used for cooling. The *Delta Elektronika* power supplies that provide current to the coils and solenoids can only be turned on if the coils' cooling water is flowing and their temperature is under 60°C. Thermal protectors of *thermik* are placed in each coil and solenoid. If the temperature of the coils/solenoids reaches 60°C, then the thermal protector will switch off, signaling the *National Instruments* modules. The same principle applies to the monitoring of the cooling water, but in this case the circuit opens when the water flow stops. Two other modules monitor the voltage and current, and provide an interlock to the *Delta Elektronika* power supplies.

The interface of the remote control and monitoring of the valves, pumps, coils, etc. is programmed in LabView. Figure 4.14 shows the panel used to control the pressure and the magnetic field in the buffer gas trap. The blue boxes correspond to the vacuum chambers and tubes that are surrounded by the coils and solenoids. The last chamber corresponds to the ANTION apparatus. Moreover, by clicking on the drawing of the valves, pumps and compressors one can turn them on as long as the safety conditions, encoded in the FPGA, are met. Also encoded are other safety features that turn off the cold cathode pressure gauges if the pressure is above a certain threshold, and some valves are only allowed to open if a minimum pressure is achieved.

A NI PXIe-7820R card (reconfigurable input/output module combined with a FPGA) produces TTL signals with a time resolution of 12.5 ns. These are responsible for triggering four PXI 6733 cards with 16 analogue outputs each, with a range -10 V to +10 V, which in combination with amplifiers, bias the electrodes. This card can also provide trigger signals to other equipment such as the camera and the Cesium Iodide signal acquisition card (PXIe-6366), the wave generators used in the rotating wall technique and the three switches.

A trap, accumulation, dump routine that characterizes the normal behavior of a buffer gas trap, consists on a sequence of commands that set each electrode bias and applied triggers, during a precise time step. These routines have been fully automated by a Labview program named Sequence Editor (see figure 4.16). The first four sets of triggers correspond to output digital triggers, while the last two sets correspond to digital input triggers. If an input trigger is selected, then the following commands are only executed once the trigger is received. The digital triggers are produced or received by the above mentioned PXIe-7820R card. For each sequence step, the electrodes' voltage can be specified, as well as the number of points in a voltage ramp, and a plot of the applied voltages is shown. The length of each step is adjustable to a 12.5 ns precision.

Besides being extremely practical to operate the trap, this framework is also very flexible. One can easily create multiple sequences with small variations that allow for the optimization of the potentials, the duration of the steps and the rotating wall parameters.

Low noise amplifiers, built by Dr. Aled Isaac of Swansea University, scale the voltages 14 times providing potentials between -140V and +140V. The amplifiers are capable of rise/fall rates (10% - 90%) of 11 V/μs. Electrodes 3 to 13 of the first stage are

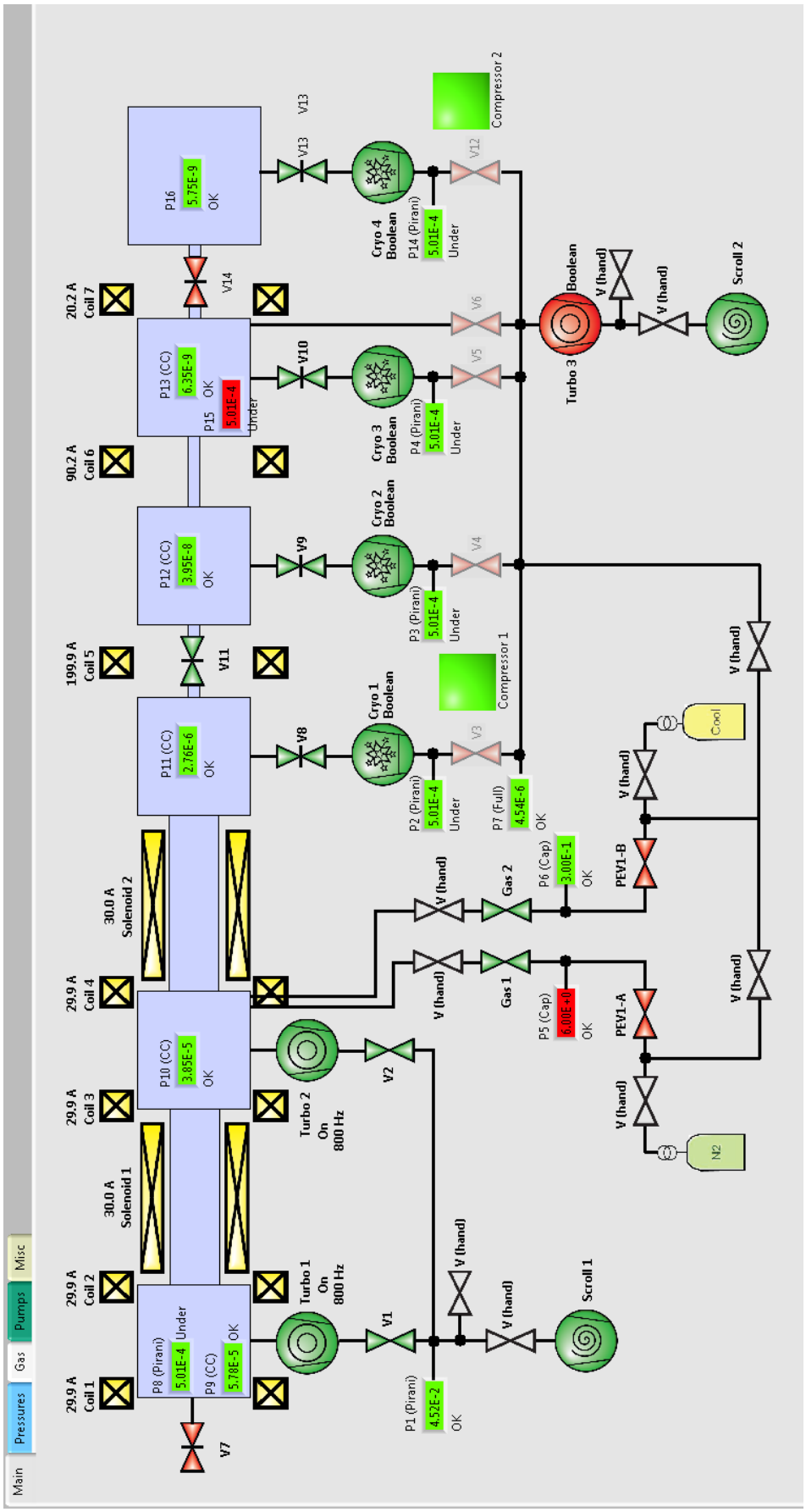

Figure 4.14: The front panel of the LabVIEW program that allows the monitoring of the pressure and the control of the vacuum pumps, valves and coils/solenoids' power supplies.

biased by a linear potential divider. All the other electrodes are controlled individually. The electrodes are monitored using the card NI9205 plugged into the CompactRIO II. To produce the Rotating Wall electric fields the amplifier voltage is superposed with the sinusoidal voltages generated by a Wavefactory 1946 - a two channel multifunction synthesizer. The two channels have a phase difference of 90° and each one is connected to a power splitter, followed by a RC circuit. In the end four sinusoidal voltages with a phase 0°, 90°, 180° and 270° are applied to the four segments constituting the rotating wall. A schematic diagram of the setup that controls the electrodes' bias is shown in figure 4.15.

4.3.5 Data acquisition

The data acquisition is done by measuring the CsI detector voltage with a NI PXIe-6366 digitizer card with 2 Mega samples per second per channel and 16-bit resolution. The trigger is provided by the above mentioned NI PXIe-7820R card. Both the digitized CsI signal and the MCP picture are saved for each routine for offline analysis.

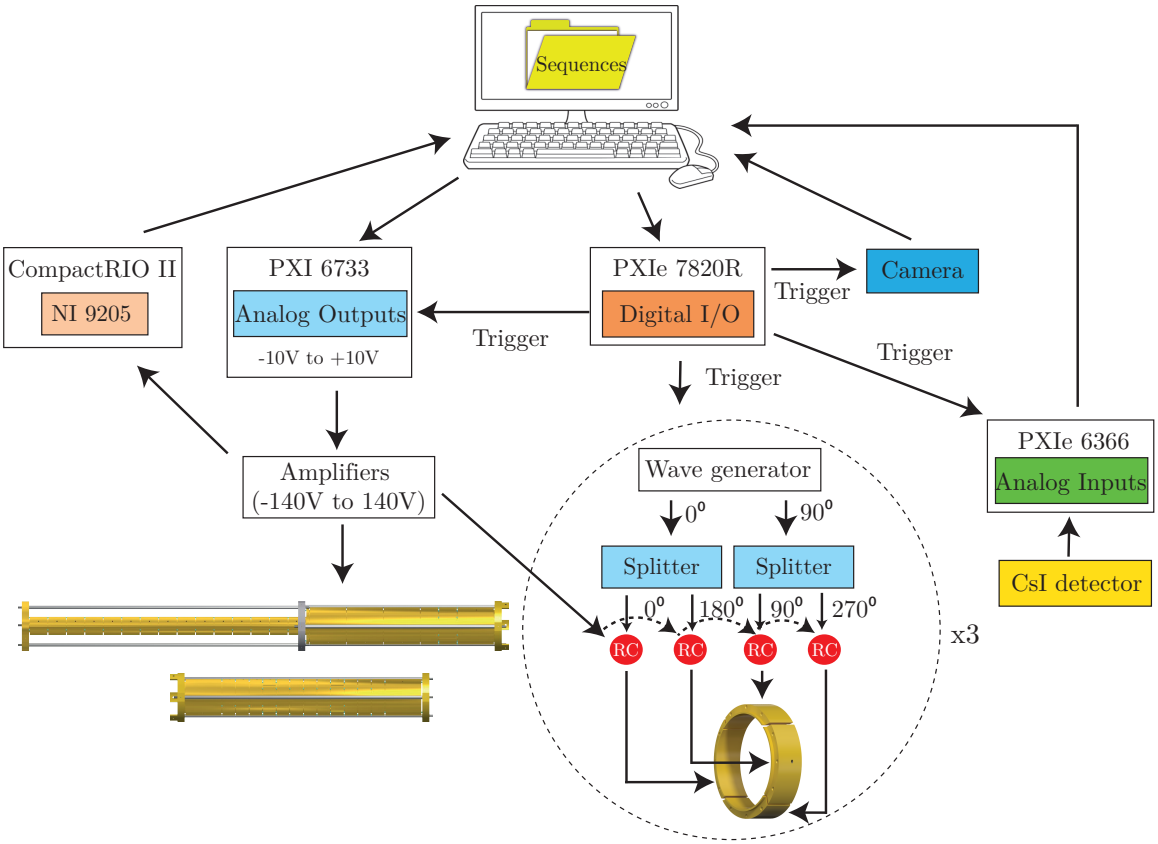

Figure 4.15: Schematic overview of the setup that controls the electrodes' bias. A Labview program named Sequence Editor edits sequences of commands that are timely executed by diverse cards. Three PXI 6733 cards output analog signals from -10 V to +10 upon being triggered by the PXIe 7820R card. These signals are amplified fourteen times and connected to the respective electrode. They are monitored by the card NI 9205 in CompactRIO II. Three wave generators, triggered by a PXIe 7820R card, produce sinusoidal voltages in quadrature. The sinusoidal voltages are phase split and superposed to the amplifiers' voltage in an RC circuit before feeding each rotating wall. The signal of the caesium iodide detector is digitized by the PXIe 6366 card and analyzed by a Labview program.

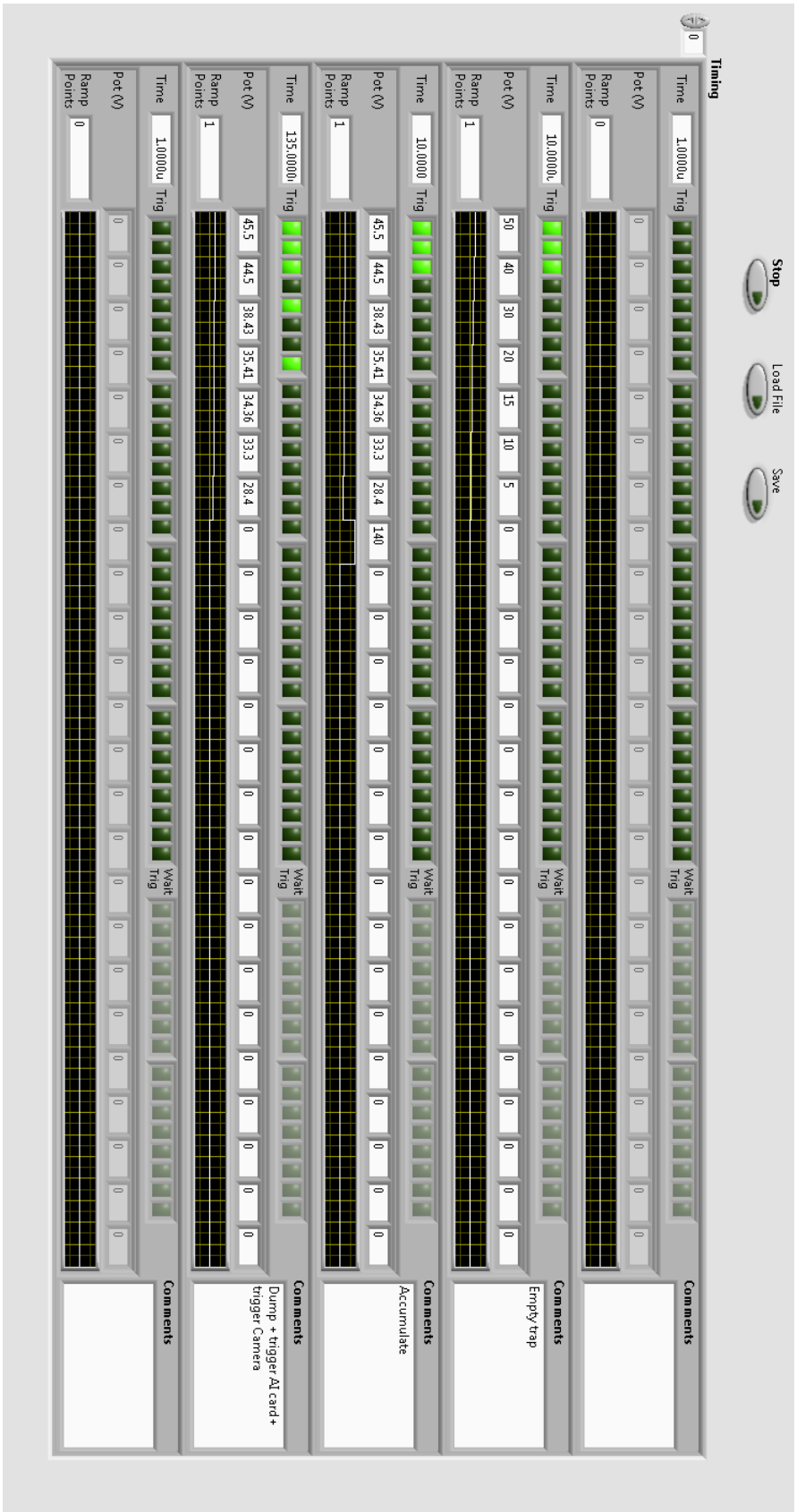

Figure 4.16: Sequence editor Labview program.

4.4 Conclusion

This chapter described the three stage buffer gas trap that was built during this thesis, with the purpose of cooling and accumulating the positrons produced by the LINAC apparatus. A few theoretical tools were also discussed, which will allow the understanding of the positron accumulation results, explained in chapter 5.

The construction of the trap involved assembling a vacuum system including vacum chambers, pumps, pressure gauges and valves. The two stacks of electrodes comprising the first, second and third stage were assembled, cabled and inserted into the vacuum chambers. *National Instruments* modules were employed to control and monitor the trap, namely the buffer and cooling gas pressures, the electrostatic potential formed by the electrodes, the magnetic fields produced by the coils, the data acquisition, safety interlocks, etc. Moreover, software was written which, in combination with the installed hardware, allows the remote operation of the trap.

The buffer gas trap is now fully operational. Some work is still required to increase even further the automation capabilities. This includes the development of software that allows automatic optimizations, namely the pressures of the buffer and cooling gases as a function of the rotating wall parameters or the trap potentials. Regarding the data analysis, software needs to be developed to perform online fitting of the pictures taken by the CCD camera, as well as fitting of the accumulation data to efficiently retrieve the trapping efficiency and the lifetime of the positrons.

The following chapter is dedicated to the description of the commission and optimization work carried out to characterize the behavior of the trap and to enhance the number of accumulated positrons.

A picture of the buffer gas trap can be seen in figure 4.17.

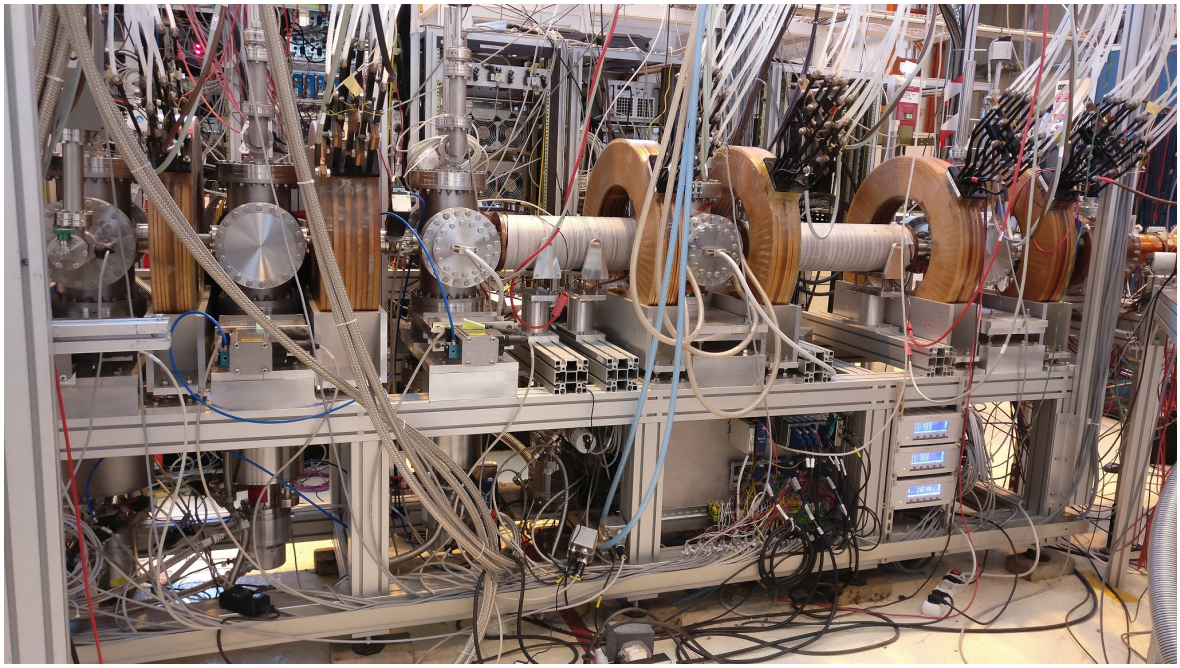

Figure 4.17: The buffer gas trap currently working at Saclay.

5 Buffer gas trap accumulation experiments

"Our knowledge can be only finite, while our ignorance must necessarily be infinite."
Karl Popper

Contents

The studies described in this chapter were executed with the goal of maximizing the number of accumulated positrons in a buffer gas trap, in order to produce a dense positronium cloud for the measurement of the hydrogen cross section. This chapter is divided in three sections: trapping, accumulation and characterization of the formed positron beam. At first, the trapping protocol is described and the effect of the buffer and cooling gas is shown, as well as the application of the rotating wall technique. Secondly, the positron transport technique from the second to the third stage is studied, as well as the accumulation of many positron stacks in the third stage. Finally, the positron beam ejected out of the trap is characterized, i.e. its time distribution and radial profile are discussed.

5.1 First and second stage trapping

This section is dedicated to the experiments performed in the first and second stage of the buffer gas trap, corresponding to the trapping stage. Most of the described measurements had the goal of optimizing the number of trapped positrons. Hence, the buffer and cooling gas optimization results are shown, as well experiments conducted to optimize the rotating wall. The optimization procedures also provided hints of how these parameters affect the trapping and cooling of positrons. Finally, the positron cloud formed in the second stage is ejected out of the trap and its energy distribution is analyzed.

5.1.1 Positron trapping technique

The first and second stage of the buffer gas trap aim to slow down the positrons provided by the LINAC. Before initiating the trapping experiments, the first and second stages are filled with the buffer and cooling gases. The electric potential responsible for the axial confinement, is formed by biasing each electrode. The first electrode (E_0) corresponds to the entry barrier, and the last one (E_5) to the exit barrier. These are responsible for trapping the positrons, forcing them to be reflected in between the barriers. The remaining 14 electrodes of the first stage are kept at the same potential, forming a flat region, by applying the same bias to the electrode High (second electrode of the first stage) and Low (last electrode of the first stage). The second stage electrodes are biased with progressively lower voltages to form a potential well. The bottom of the well is formed by an electrode divided in half and one of the halves is a rotating wall electrode. Table 5.1 shows the typical bias applied to each electrode forming the axial electrostatic potential shown in figure 5.1, computed with the SIMION software.

The trapping technique is divided into three phases: trapping, close injection and ejection. In the first phase, the positrons arrive at the trap entry with a mean longitudinal kinetic energy of $\sim 50\,\mathrm{eV}$ and overcome the entry potential barrier formed by electrode E_0. As the positrons travel through the first and second stage, they undergo inelastic collisions with the buffer gas. One collision is enough to trap the positrons between the potential barriers formed by electrodes E_0 and E_5. The positrons that do not slow down, are able to pass over the entry potential barrier, exiting the trap, thus they will not be trapped. Those that are confined in the trap, undergo further

Table 5.1: Typical potentials applied to the first and second stage electrodes during trapping and ejection. These potentials were optimized with a magnetic field at the moderator position of 133 G.

Electrodes	E_0	High	Low	E_1	E_2	E_3	E_4	E_5
Trapping Potential (V)	45.5	39.5	39.5	35.41	34.36	33.3	28.85	140
Ejection Potential (V)	100	39.5	39.5	35.41	34.36	33.3	28.85	0

collisions and migrate into the deepest part of the well, in the second stage. Given that the LINAC is operated at 200 Hz, positron bunches arrive at the trap every 5 ms. This procedure is repeated as long as the trap is open, i.e. the entry potential is kept below ~ 50 V. The rotating wall technique is applied continuously during the trapping phase to make sure that the radial transport to the electrodes' walls is minimized, as gas is present. Before the positrons are ejected, the entry potential is raised to 100 V to avoid that more positrons enter the trap and mix with the already cooled positron cloud. In the ejection phase, the exit gate is quickly lowered from 140 V to 0 V, in 80 ns, by a fast switch.

Two destructive detection techniques were employed during these experiments. A 20 mm diameter MCP combined with a phosphor screen and a CCD camera, were used to obtain a two dimensional density profile of the positron cloud, and a CsI detector to measure the number of trapped positrons.

During the trapping phase, the number of accumulated positrons increases with time, until it reaches an equilibrium point in which the number of trapped positrons compensates the ones lost to outward radial transport and annihilation. This regime is denominated saturation. The positron trapping rate R, which is the number of trapped positrons per second, can be defined as $R = I_0\,\varepsilon$, where I_0 is the intensity of the incoming beam and ε the positron trapping efficiency. The number of trapped positrons with time is dependent on the trapping rate and on the annihilation rate via

$$\frac{dN}{dt} = R - \frac{N}{\tau}\,, \tag{5.1}$$

where τ is the positron lifetime in the trap. At any given moment the number of positrons inside the trap is given by

$$N(t) = R\,\tau\left(1 - e^{-t/\tau}\right)\,. \tag{5.2}$$

The trapping rate and the lifetime are parameters essential to characterize the efficiency of the trap and the competing loss mechanisms at play. In order to determine these parameters, the sequence trap-close injection-ejection is repeated for several accumulation times, i.e. the time in which the trap is left open to receive the positron bunches is varied. The annihilation signal of the ejected positrons is monitored by a CsI detector. With this procedure an accumulation curve, such as the one in figure 5.2, is acquired. The data points are fit to the equation 5.2, yielding the desired parameters;

in this case R = 7.97 ± 0.08 arb./s and τ = 647 ± 7 ms.

In this thesis, the CsI signal is given in arbitrary units when the absolute number of trapped positrons is not required for the understanding of the results. The reason being that, for some experiments, the CsI had to be moved to a different location because, due to the large amount of positrons, the detector saturated; or the detector had to be positioned closer to the annihilation site because the signal was too weak.

5.1.2 Positron beam parallel energy distribution

As was demonstrated in section 3.3.2, the parallel energy spread of the positron beam varies as the positrons propagate through regions of varying magnetic field. The first and second stage are in a region in which the magnetic field is 450 G - 460 G. When the positrons enter the strong magnetic field of the trap, the parallel energy spread $\sigma_{\parallel}$ increases significantly. This results in a reduction of the trapping efficiency as was explained in section 4.2. To evaluate the energy spread as a function of the magnetic field difference between the region where the positrons are formed (target and moderator) and the buffer gas trap, and to optimize the trapping efficiency, the parallel energy distribution of the positron beam was measured for two different moderator magnetic fields: 133 G and 333 G, henceforth referred as B_{133G} and B_{333G}, respectively. These measurements were performed using the Retarding Potential Analyzer (RPA) technique described in section 3.3.2. In this case, the RPA consisted of three electrodes of the third stage and the MCP was the target. The annihilation signal was measured by a CsI detector.

Figure 5.3 shows the integral of the parallel energy distribution, fitted to an exponentially modified Gaussian and the negative derivative of the fit for B_{133G}. The data points of the B_{333G} measurement are shown as well as the error function fit. In the B_{133G} case, the positrons were formed in a region in which the magnetic field is 70% lower than the trap field, giving rise to a large deviation from the Gaussian distribution. This occurs because the parallel and the transversal energies are coupled by the conservation of the magnetic moment and the total energy, as was shown in Chapter 3. In that case, it can be shown that when the positrons propagate from a low magnetic field to a high magnetic field, a tail forms on the left side of the distribution [95]. On the contrary, the B_{333G} data points present a distinct Gaussian behavior. The fit of the B_{133G} data points yielded a parallel energy spread of
$\sigma_{\parallel}$ = 3.59 ± 0.03 eV and a mean parallel energy $\bar{E}_{\parallel}$ = 45.695 ± 0.002 eV; while the fit of the B_{333G} data yielded $\sigma_{\parallel}$ = 1.42 ± 0.05 eV and $\bar{E}_{\parallel}$ = 48.77 ± 0.03 eV. Figure 5.3c shows a comparison between both measurements.

The vertical lines in figure 5.3 were added to indicate the barrier height of the first stage, corresponding to 45.1 V and 47 V (potentials computed with SIMION) for B_{133G} and B_{333G}, respectively. The intersection of these lines with the error function fit gives the fraction of positrons that are able to enter trap. For B_{133G} this fraction is 46%, and for B_{333G} is 90%, suggesting a higher trapping efficiency. Moreover, as expected, the energy spread is larger if the magnetic field difference between the positron source and the buffer gas trap is larger. This results in a smaller amount of positrons that are available to be trapped, since a larger portion of the positrons are too slow to overcome the potential barrier (those to the left of the dashed vertical line). Added to that, a

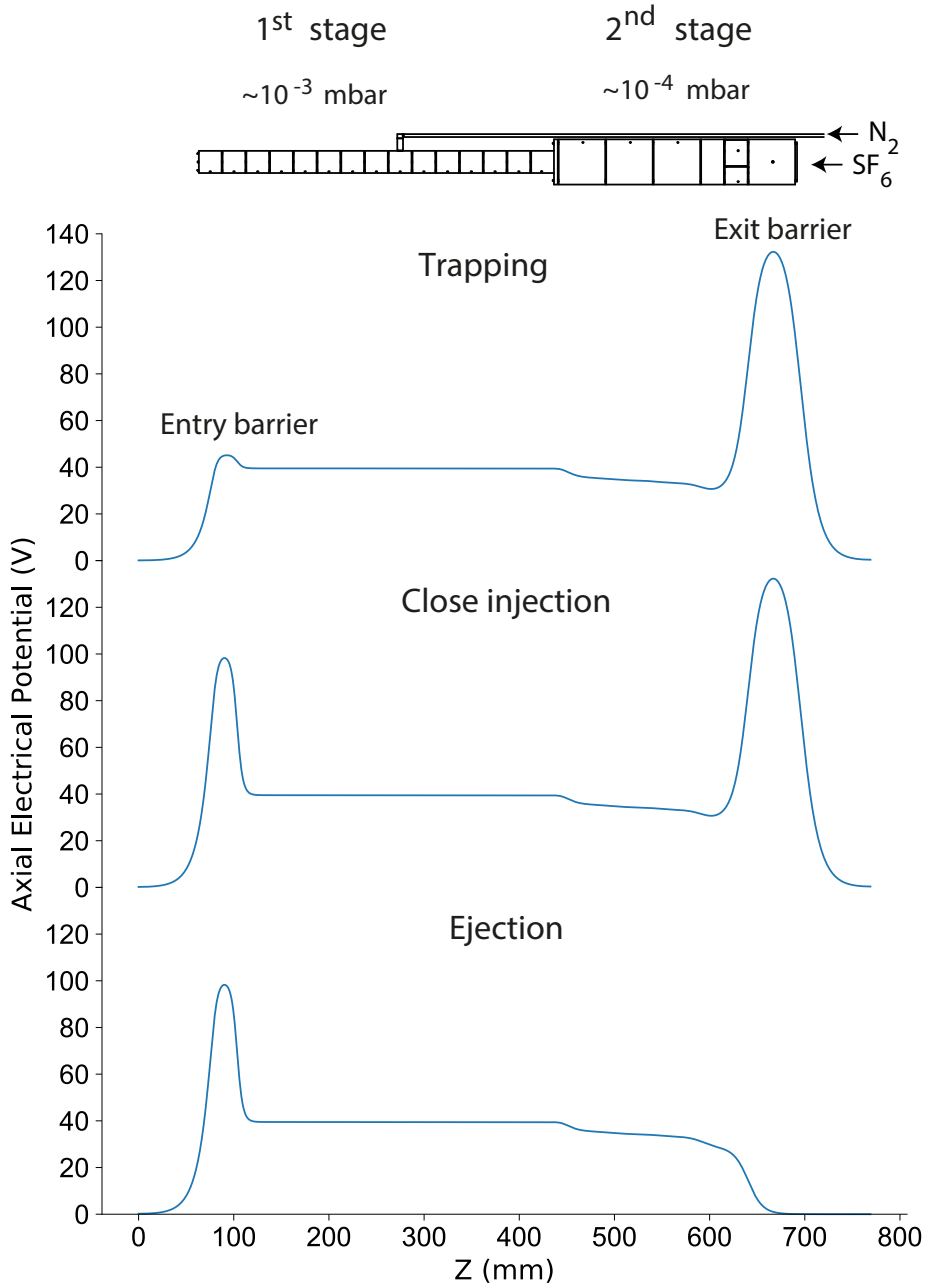

Figure 5.1: Schematic diagram of the axial electrical potential of the first and second stage during the trap-close injection-ejection sequence. Nitrogen gas is introduced by a tube located in the middle of the first stage, and cooling gas is introduced at the end of the second stage. In the trapping phase the positrons that undergo an inelastic collision with the buffer gas, become trapped between the entry barrier and the exit barrier. To prevent incoming positrons to enter the trap when the trapped positrons are ejected, the entry barrier is raised to 100 V. The positrons are expelled when the exit barrier is lowered from 140 V to 0 V in 80 ns.

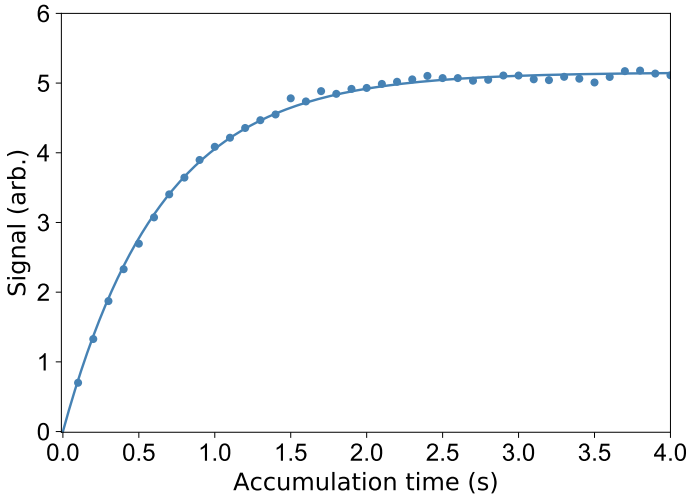

Figure 5.2: A typical accumulation curve in the first and second stage: the positron annihilation signal, measured by a CsI detector, as a function of the accumulation time. The data points were fitted to the equation 5.2, yielding R = 7.97 ± 0.08 arb./s and τ = 647 ± 7 ms.

larger fraction of positrons are very energetic leading to an increase of the probability of positronium formation.

According to the two adiabatic invariants given by equations 3.4 and 3.5, $\bar{E}_{\parallel}$ should decrease if the magnetic fields ratio B/B_0 is larger than 1, where B is the magnetic field in the first stage and B_0 the magnetic field in the moderator. This effect was also observed, being $E_{\parallel}$ smaller for B_{133G} ($\bar{E}_{\parallel}$ = 45.695 ± 0.002 eV) than for B_{333G} ($\bar{E}_{\parallel}$ = 48.77 ± 0.03 eV).

Figure 5.3c shows that for the moderator at 333 G the annihilation signal is 30% smaller than the signal corresponding to the moderator at 133 G. This can be explained by considering equation 3.8 in Chapter 3, which models how the positron beam radius varies with varying magnetic field. From this equation one can deduce that the radius of the positron beam is larger at the entry of the buffer gas trap when the moderator's magnetic field is 333 G compared to 133 G: $r(B_{333G}) \sim 1.6 \times r(B_{133G})$.

The positron beam size was measured in the vacuum cross before the buffer gas trap (cross I) by incrementally lowering an aluminium plate, perpendicular to the beam direction, blocking the positron beam. The positrons that were not blocked by the plate, were able to travel into a target, where they annihilated. The annihilation signal was measured by a CsI detector. This measurement was performed for several plate positions and the data points are plotted in Figure 5.4, along with an error function fit. The derivative of the fit provides the positron beam profile, yielding σ = 2.4 ± 0.1 mm and FWHM = 5.60 ± 0.08 mm. This measurement was executed when the magnetic field in the moderator was 50 G. For B_{133G}, equation 3.8 predicts that the FWHM should be 9.1 mm and 14.5 mm for B_{333G}.

Upstream of the buffer gas trap there is a pumping restriction of 20 mm diameter, while the diameter of the electrodes of the first stage is 16 mm. Since the FWHM of the positron beam for the moderator at 333 G is 14.5 mm, then part of the positron

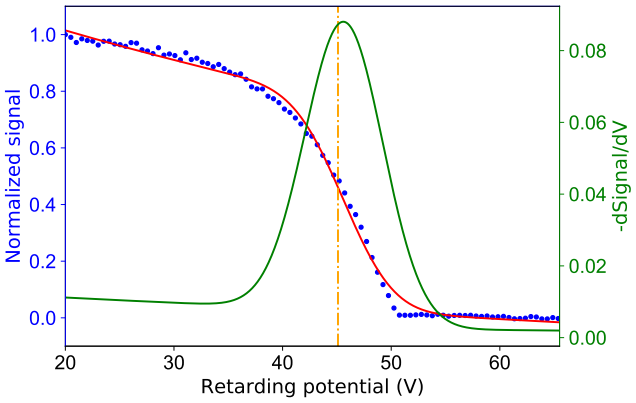

(a)

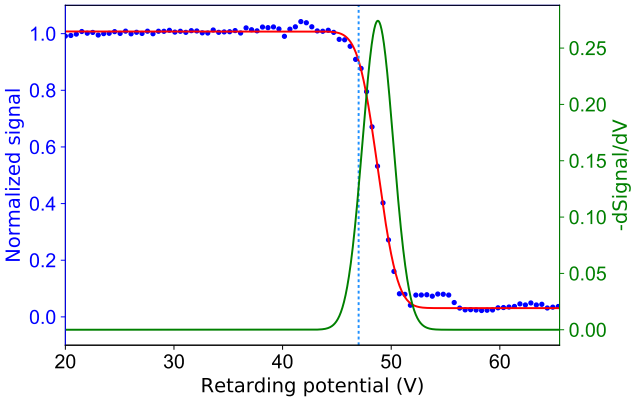

(b)

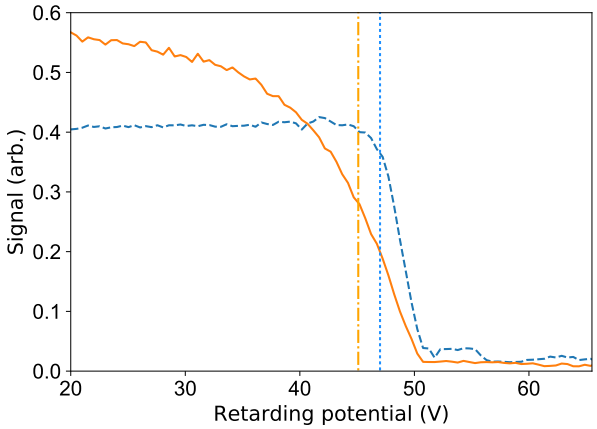

(c)

Figure 5.3: Positron beam parallel energy distribution at the entry of the buffer gas trap. Normalized cumulative parallel energy distribution (•), exponentially modified Gaussian fit / error function fit (—) and negative derivative of the fit (—) for B_{133G} (a) and B_{333G} (b). The fit of B_{133G} yielded $\sigma_{\parallel} = 3.59 \pm 0.03\,\text{eV}$, $\bar{E}_{\parallel} = 45.695 \pm 0.002\,\text{eV}$; the fit of B_{333G} yielded $\sigma_{\parallel} = 1.42 \pm 0.05\,\text{eV}$, $\bar{E}_{\parallel} = 48.77 \pm 0.03\,\text{eV}$. (c) Comparison between (—) B_{133G} and (- -) B_{333G}. The vertical lines indicate the barrier height of the first stage corresponding to 45.1 V and 47 V (potentials computed with SIMION) for B_{133G} and B_{333G}, respectively.

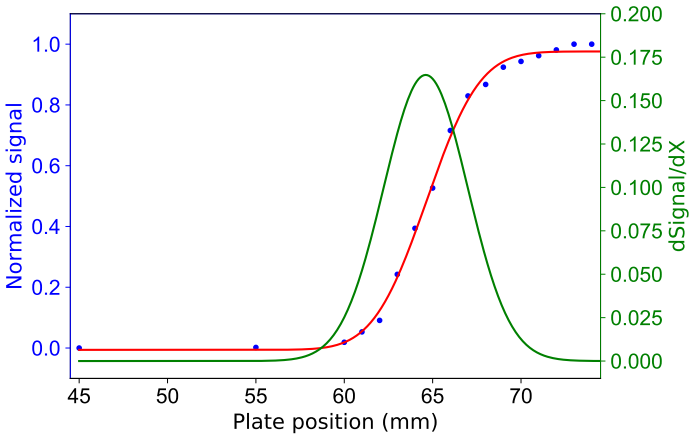

Figure 5.4: Positron beam dimensions at the entry of the buffer gas trap. σ = 2.4 ± 0.1 mm and FWHM = 5.60 ± 0.08 mm. This measurement was executed when the magnetic field in the moderator was 50 G.

beam is annihilated before entering the trap, thus the observed 30% loss.
A strong annihilation signal was observed when positioning the CsI detector near to the pumping restriction and near the first electrode, confirming this hypothesis. Increasing the magnetic field in the region of the pumping restriction, and at the entry of the buffer gas trap, would solve this problem but an additional power supply was not available at the time of writing.

Given that the trapping efficiency is dependent on the energy spread, which is dependent on the difference between the magnetic fields in which the beam is created and the trapping field, the trapping potentials were optimized for both moderator magnetic fields. The optimization of the potentials was carried out, in a first phase, by varying all the electrodes' bias in incremental steps and by the same amount.
A trap-close injection-ejection sequence was executed for each step, in order to monitor the relative number of trapped positrons. In a second phase, the bias of each electrode was varied individually around the optimized values encountered in the first phase. The optimal trapping potentials for B_{333G} are shown in table 5.2, and for B_{133G} in table 5.1. A comparison between both axial electrical potentials is presented in figure 5.5. As will be shown later, the pronounced difference in the well configuration results in a different axial bounce frequency, thus a different rotating wall frequency for which the compression is resonant.

To evaluate how the energy spread of the incoming positron beam affects the trapping efficiency, an accumulation curve was done for the two moderator magnetic fields, each with its optimal trapping potentials. These curves can be viewed in figure 5.6, in which a trapping efficiency of 11.7 ± 0.1% was obtained for B_{333G} and 9.1% ± 0.4% for B_{133G}. The trapping efficiency was computed using the expression

$$\varepsilon = \frac{R}{I_0 \, f_{linac}}, \tag{5.3}$$

where R corresponds to the trapping rate, I_0 to the CsI signal of one positron bunch and f_{linac} to the LINAC frequency (200 Hz). As expected, the trapping efficiency is

Table 5.2: The potentials applied to the first and second stage electrodes during trapping and ejection. These potentials were optimized with a magnetic field at the moderator position of 333G G.

Electrodes	E_0	High	Low	E_1	E_2	E_3	E_4	E_5
Trapping Potential (V)	47.5	39.5	39.5	35.41	34.36	32.3	29.3	140
Ejection Potential (V)	100	39.5	39.5	35.41	34.36	32.3	29.3	0

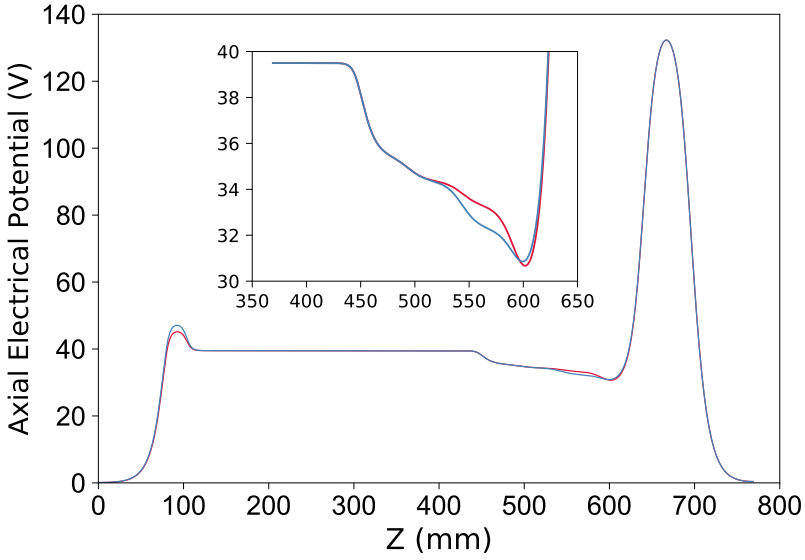

Figure 5.5: Axial electric potential computed using SIMION for (—) B_{133G} and (—) B_{333G}.

higher if the magnetic field ratio, B/B_0, is closer to one. Yet, one would expect the efficiency to be much higher for 333 G since its energy spread is 40% smaller. This might indicate that the dominant effect affecting the efficiency is not the energy spread, but some other parameter such as the buffer gas pressure or the rotating wall settings.

5.1.3 Buffer gas pressure effect

To study the the trapping rate and lifetime as a function of the buffer gas pressure, an accumulation curve was measured for different values of nitrogen pressure measured by the pressure gauge P9. This measurement is shown in figure 5.7. The study was performed with the moderator at 333 G, but before optimizing the potentials of the first and second stage. The rotating wall technique was not applied and no SF_6 gas was present. Each curve was measured until saturation was achieved, which occurs in a smaller accumulation time for higher nitrogen pressure. As the nitrogen pressure increases, the trapping rate increases, while having the adverse, but expected effect, of decreasing the positron lifetime. This decrease is dominated at this point by radial

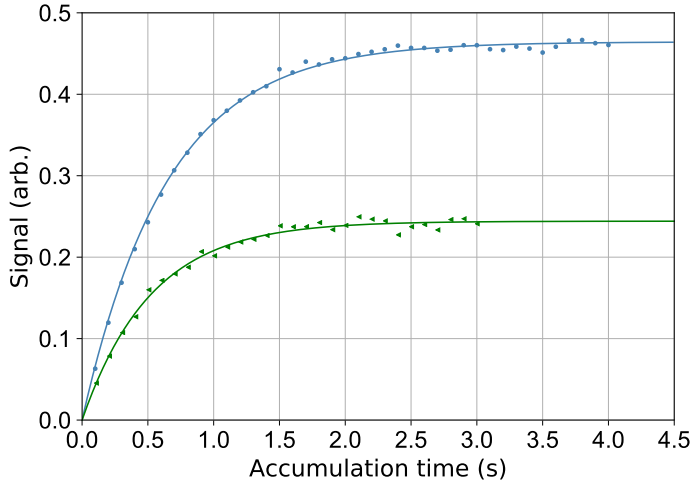

Figure 5.6: Accumulation curve fitted to equation 5.2 for (◀) B_{133G} and (●) B_{333G}. The fits yielded $R_{133G} = 0.47 \pm 0.01$ arb./s, $\varepsilon_{133G} = 9.1\% \pm 0.4\%$, $R_{333G} = 0.731 \pm 0.007$ arb./s and $\varepsilon_{333G} = 11.7 \pm 0.1\%$, respectively.

transport. This claim is supported by the fact that the lifetime for these pressures should be longer than the one measured, and as will be demonstrated, the lifetime can be increased by applying the rotating wall.

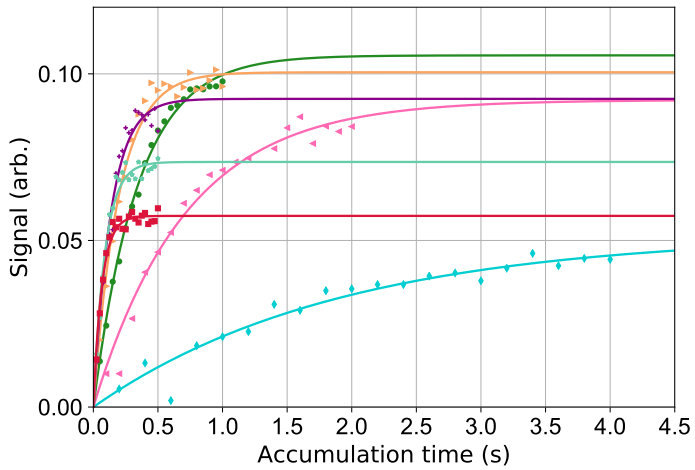

Figure 5.7: Number of particles in the trap as a function of accumulation time, $N(t)$, for different N_2 pressures measured by the pressure gauge P9: ♦ 0.24×10^{-5} mbar, ◀ 0.83×10^{-5} mbar, ● 1.8×10^{-5} mbar, ▶ 3×10^{-5} mbar, + 4.3×10^{-5} mbar, * 5.5×10^{-5} mbar, ■ 6.9×10^{-5} mbar. The data were fitted to the equation 5.2.

The trapping rate and the lifetime can be understood by fitting the data points in figure 5.7 to equation 5.2. To better understand the behavior of the trapping rate with the buffer gas pressure it is interesting to plot R as a function of the pressure. This curve can be observed in figure 5.8a. The error bars arise from the fitting, and the data points were fit to

$$R = I_0\, f \left(1 - e^{-D\,P}\right) , \tag{5.4}$$

in which f is the branching ratio given by the ratio of the cross section for electronic excitation of N_2 to that of other processes [88], such as the competing positronium formation process. D depends on the total scattering cross section of positron-N_2 collisions. The term $1 - e^{-D\,P}$ corresponds, therefore, to the probability of a positron to undergo a collision with a N_2 molecule before exiting the trap.

The positron loss rate, λ, is plotted in figure 5.8b, and its inverse, the lifetime, is plotted in figure 5.8c. The loss rate is expected to be proportional to the nitrogen pressure via

$$\lambda = 1/\tau = B P\,, \tag{5.5}$$

where B is constant at a fixed temperature and is related to the effective number of electrons in the N_2 molecule available for annihilation, Z_{eff}. Another loss mechanism at play is the radial transport to the electrodes' walls. At high pressures, the trap loss rate shows a deviation from the expected linear behavior, suggesting there might be another loss term more important at these pressures. At the time of this measurement a pumping restriction with 16 mm diameter (an orifice) was present between the second and the third stage. The ejected positrons must pass through this orifice, and the third stage, to reach the MCP where they annihilate and the scintillation signal is detected. For high pressures, the positron cloud radius is possibly so large that the positrons hit the wall of the pumping restriction, resulting in another loss mechanism. This effect also explains the reason why the trapping rate seems to saturate for pressures higher than $6{\times}10^{-5}$ mbar.

The maximum number of positrons that can be trapped at a certain pressure is given by the parameter N_∞, defined as $R\,\tau$. From equation 5.4 and 5.5 one would expect it to behave as

$$N_\infty = \frac{I_0\, f\, \left(1 - e^{-D\,P}\right)}{B\,P} . \tag{5.6}$$

At low pressures N_∞ should approach $I_0\, f\, D/B$, while for high pressures it behaves as $1/P$. Figure 5.9 shows a plot of N_∞ as a function of the nitrogen pressure. For high pressures it follows the expected behavior, tending to lower N_∞ values. Yet, for low pressures it does not seem to follow the expected behavior. Clarke *et al.* [88], referring to the trap from which this one was based on, suggested there might be another unidentified loss mechanism, also dependent on the nitrogen pressure, and represented by a term of the form $EP/(EP + F)$. This term should in principle parametrize the transfer efficiency of the positrons from the first stage to the second stage, where $E\,P$ is the capture probability of the second stage and F is a constant. N_∞ can then be written as

$$N_\infty = \frac{I_0\, f\, E}{B} \left(\frac{1 - e^{-D\,P}}{E\,P + F}\right) . \tag{5.7}$$

Figure 5.9 was fit to this equation and it suggests that this trap also demonstrates the same behavior as Clarke's.

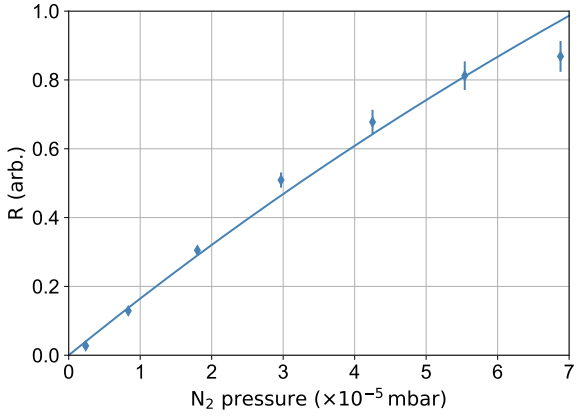

(a)

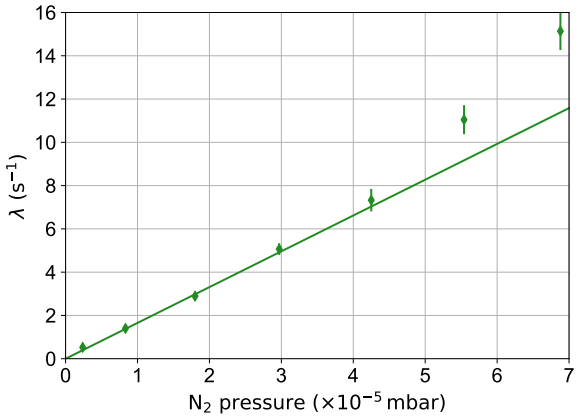

(b)

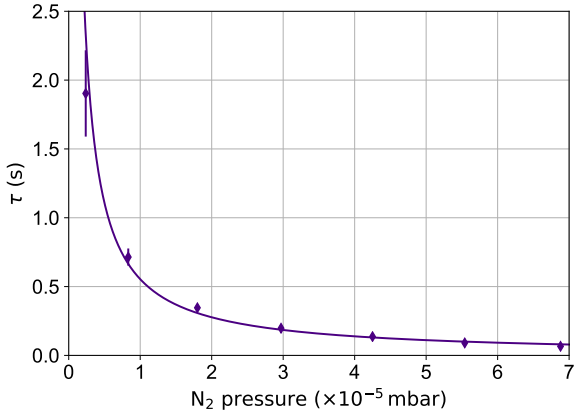

(c)

Figure 5.8: (a) Accumulation rate, R, as a function of the buffer gas pressure in units of 10^{-5} mbar. The data points were fitted to the equation 5.4, yielding $I_0 f = 3 \pm 3$ arb. and $D = 0.05 \pm 0.05\,\mathrm{mbar}^{-1}$. (b) Trap loss rate, λ, as a function of the buffer gas pressure fitted to equation 5.5. The last two points were not fitted. Fitted parameter $B = 1.8 \pm 0.09\ \mathrm{s}^{-1}\ \mathrm{mbar}^{-1}$. (c) Lifetime as a function of the buffer gas pressure. Fitted parameter $B = 2.0 \pm 0.1\ \mathrm{s}^{-1}\,\mathrm{mbar}^{-1}$.

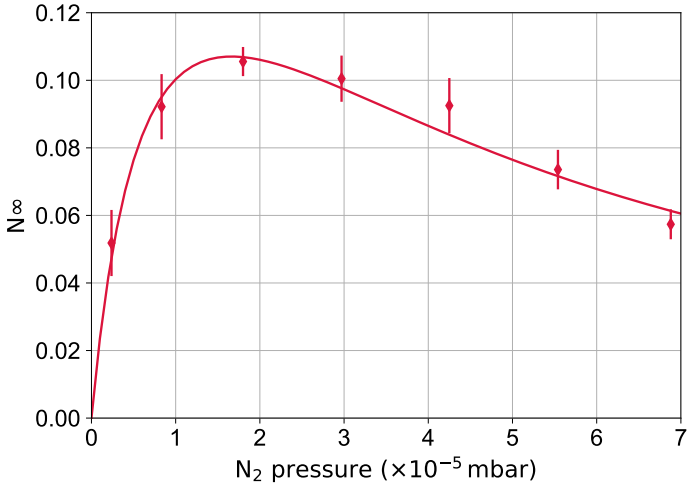

Figure 5.9: N_∞ as a function of the buffer gas pressure. The data points where fitted to equation 5.7.

During the trapping phase, the lifetime is not the most important parameter since the positrons are not kept in the second stage for a long time, as the pressure is very high. Indeed, the goal is to optimize the number of trapped positrons, and thus maximize the trapping rate regardless of the lifetime. Therefore, it would be interesting to repeat this measurement while applying the rotating wall technique, which would allow the use of higher nitrogen pressures without the loss of positrons to both the orifice wall and the electrodes' wall. This measurement would result in a curve akin to the one shown in figure 5.8a, yet saturation (region in which the trapping rate stabilizes) would be reached at much higher pressures. The optimal pressure would then correspond to the one immediately before saturation. Knowing the optimal pressure, one could chose the best accumulation time from the corresponding accumulation curve: the accumulation time immediately before saturation is reached.

5.1.4 Cooling gas effect

The cooling gas is added to the second stage when the rotating wall technique is applied, to counteract the heating of the positrons. However, an additional gas has also the effect of decreasing the lifetime of the positrons due to their annihilation with the SF_6 molecules, or due to radial transport. The study described in this section aims to show the effect of the cooling gas pressure on the number of trapped positrons and positron lifetime. The rotating wall was not employed in this study.

Accumulation curves were obtained for a set of different SF_6 pressures, measured by the pressure gauge P10 (the correction factor of 2.5 was taken into account), and keeping the nitrogen pressure constant to 5.5×10^{-5} mbar, measured in P9. These curves are presented in figure 5.10 (a few curves were removed for clarity). One can observe that the cooling gas does not have a significant effect on the trapping rate. This is more obvious in figure 5.11a, in which the trapping rate, R, is shown as a function of the SF_6 pressure. Given that the rotating wall technique was not being employed, the loss rate is increased by the presence of the extra gas, as can be observed in figure 5.11b.

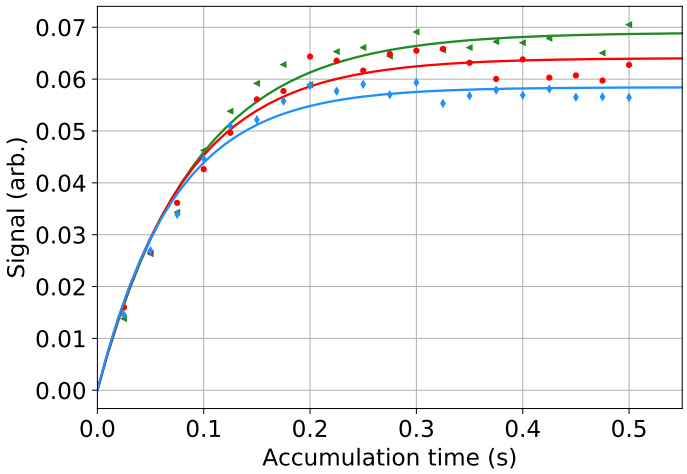

Figure 5.10: Cooling gas effect. The caesium iodide detector signal as a function of the accumulation time for different SF_6 pressures measured by the pressure gauge P10: ◀ 2.8×10^{-6} mbar, ● 8×10^{-6} mbar, ◆ 1.4×10^{-5} mbar. The data was fitted with equation 5.2.

In these measurements, the loss rate given by equation 5.5 has an additional term to account for the SF_6 gas:

$$\lambda = C\, P_{SF_6}\,, \tag{5.8}$$

C, much like B, is related to the effective number of electrons in the SF_6 molecule available for annihilation, and the radial transport.

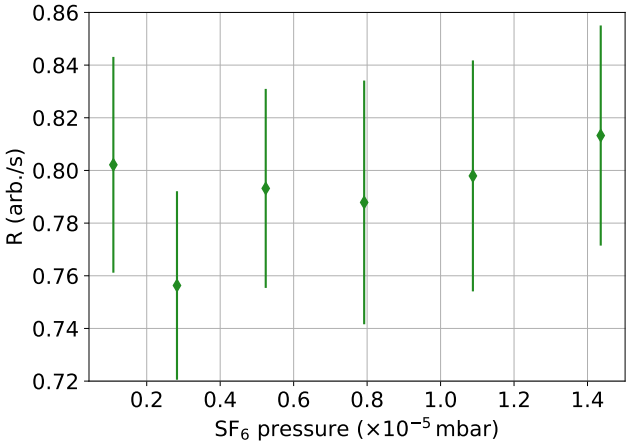

(a)

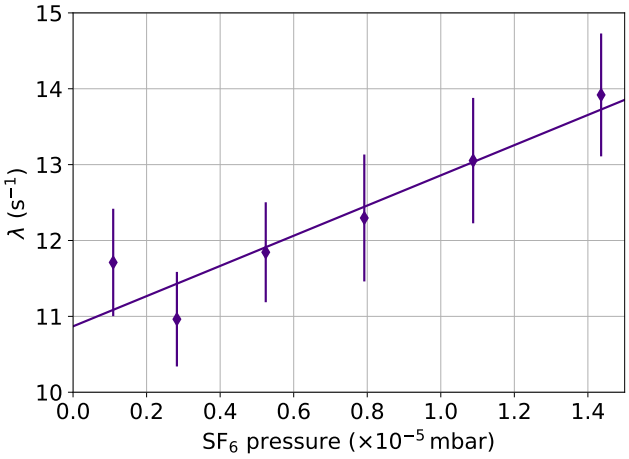

(b)

Figure 5.11: The positron trapping (a) and loss rate (b) as a function of the SF_6 gas pressure measured in pressure gauge P10. The error bars result from the fit. The loss rate was fit to equation 5.8, in which P_{N_2} is a constant.

It would be interesting to repeat this measurement while applying the rotating wall, in order to optimize the cooling gas pressure. One would observe that a small quantity of SF_6 gas would not be enough to counteract the rotating wall heating, resulting in an expansion of the positron cloud and in the loss of positrons to the electrodes' walls. On the other hand, too much SF_6 would diminish the positron lifetime and increase the radial transport, leading to the same result as in the previous case. For that reason, a balance between the amount of SF_6 gas and the rotating wall frequency needs to be established, to operate the rotating wall in optimal conditions.

5.1.5 Rotating Wall experiments

This section describes the experiments performed to evaluate the effect of the rotating wall on counteracting the radial expansion of the positrons in the second stage, as well as the compression of the positron cloud.

To realize the first goal, two accumulation curves were obtained: in the first one the rotating wall technique was not employed (no cooling gas was added), and in the second one the rotating wall was on during the trapping phase, with a 0.3 V amplitude and a frequency of 7.3 MHz. The nitrogen pressure, measured in pressure gauge P9, was 5.5×10^{-5} mbar and the cooling gas pressure, measured in pressure gauge P10, was 8×10^{-6} mbar. These curves can be observed in figure 5.12, along with the fit to equation 5.2, yielding $R = 7.48 \pm 0.08$ arb./s and $\tau = 86 \pm 1$ ms when the rotating wall was off and no cooling gas was added, and $R = 7.97 \pm 0.08$ arb./s and $\tau = 647 \pm 7$ ms when the rotating wall was on and SF_6 gas was inserted. The difference between the two curves is striking owing to the sevenfold lifetime when the rotating wall is used. While the trapping rate remains largely unaffected, the lifetime is greatly increased, even when adding a second gas. From the measurements in the previous section, the lifetime when both cooling and buffer gases are present is 81 ms, which means that employing the rotating wall technique resulted in a eightfold increase in the lifetime.

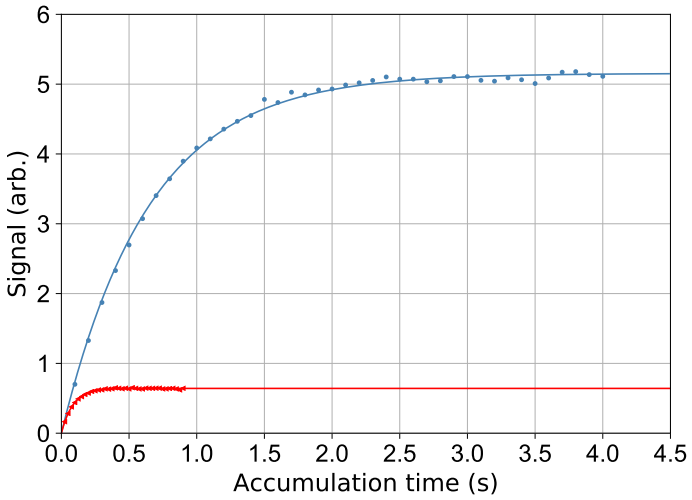

Figure 5.12: Rotating wall effect on the trapping rate and positron lifetime. The rotating wall parameters used are 0.3 V amplitude and 7.3 MHz frequency. The CsI signal is shown as a function of the accumulation time when the rotating wall was off (◀) and on (●). The data points were fitted to equation 5.2, yielding $R = 7.48 \pm 0.08$ arb./s and $\tau = 86.0 \pm 0.1$ ms for the first case, and $R = 7.97 \pm 0.08$ arb./s and $\tau = 647 \pm 7$ ms for the latter.

Given the cooling and buffer gas pressures applied in these measurements and using the tools presented in section 4.3.1, one would expect the positron annihilation lifetime to be approximately 930 ms. The measured lifetime is therefore 282 ms shorter than predicted. Several hypothesis might explain this fact: the rotating wall frequency and amplitude are not optimized thus it cannot fully counteract the radial transport;

the cooling gas pressure is not optimal for this rotating wall settings leading to heating of the cloud; the trap materials are out-gassing leading to positron loss when they collide with these molecules; the electrode stack is not well aligned with the magnetic field lines. Some of these hypothesis can be verified by attempting to optimize the rotating wall settings and the cooling gas pressure, as it was described in the previous section. The out-gassing hypothesis can be tested by baking the apparatus more thoroughly and then repeating this measurement.

The rotating wall technique only works if applied in the same direction as the magnetron motion. This results from the fact that the rotating dipolar electric field couples to the magnetron frequency of the positrons. Figure 5.13 shows a picture of the positron cloud after impinging on a MCP and phosphor-screen, when the rotating wall was applied in the same direction as the magnetron motion 5.13c and in the opposite direction 5.13b. Compression is observed in the first case, while in the latter the cloud has expanded. One can also observe that both positron clouds have an elliptical shape, suggesting there is an asymmetry in the magnetic field between the second stage and the third stage (later in this chapter it will be shown that this effect does not occur when the positrons escape the third stage). The origin of this asymmetry could possibly be a magnetic material located near the transition between the two stages.

To optimize the rotating wall frequency, the cloud radius and number of trapped positrons were monitored while scanning the frequency. For each frequency the sequence trap-close injection-ejection was executed and the rotating wall was employed during 100 ms, corresponding to the trapping phase. Afterwards, the positrons were ejected into a MCP and the phosphor screen image was registered by a CCD camera, while a CsI detector registered the annihilation signal. These images were analyzed by fitting a two dimensional Gaussian function, yielding σ_x and σ_y. The radius was defined as $(\sigma_x + \sigma_y)/2$ and the calibration 1 pixel to 32 μm was applied. The MCP is located in a zone in which the magnetic field is approximately equal to second stage (figure 4.10), hence the radius of the cloud is not expected to differ significantly from the beam formation region.

Figure 5.14a shows the positron cloud radius as a function of the rotating wall frequency for rotating wall peak-to-peak amplitudes of 0.3 V and 0.4 V. Figure 5.14b shows the respective CsI signal. The cloud radius becomes smaller as the rotating wall frequency approaches the central frequency, $f_0 = f_z + f_m$. Figure 5.14a suggests that the central frequency is $\sim$7.34 MHz corresponding to a radius $\sim$0.5 mm. As expected the central frequency is independent of the rotating wall amplitude.

Another interesting feature of 5.14a is that the curve broadens with increasing rotating wall amplitude. This behavior agrees with Isaac's model [86] which predicts that the frequency response grows linearly with the rotating wall amplitude, as is shown in equation 4.19.

The rotating wall frequency, f_0, can be estimated by fitting the potential well with a quadratic function in order to obtain the axial bounce frequency, f_z. However, as can be seen in figure 5.15b, the potential is quite anharmonic. Thus an alternative way is to integrate the potential as a function of the positron energy via

$$\frac{1}{f_z(E)} = \sqrt{\frac{2m}{q}} \int_{z_1}^{z_2} \frac{dz}{\sqrt{E - \phi(z)}}\,, \tag{5.9}$$

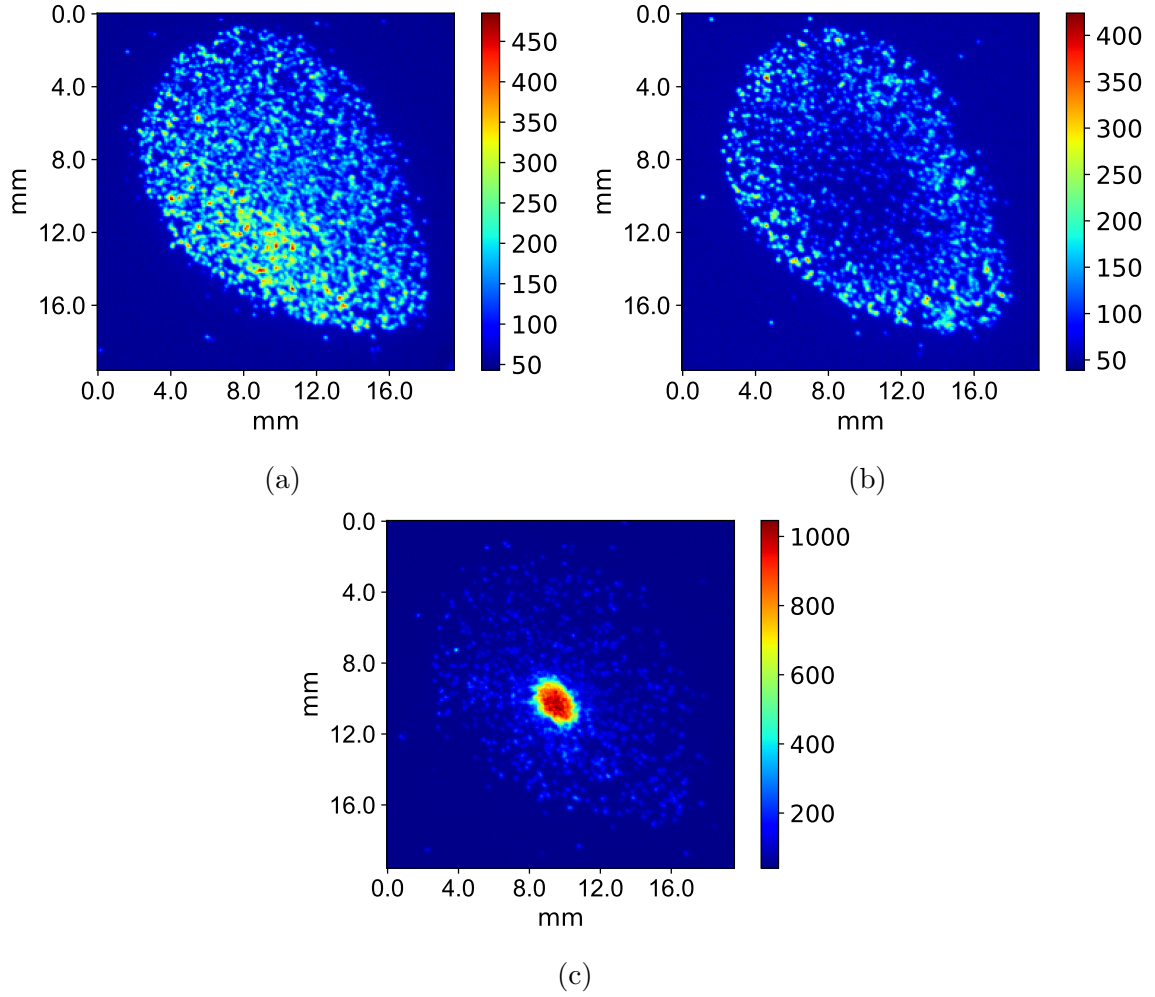

Figure 5.13: Effect of the rotating wall direction of rotation. (a) Rotating wall off. (b) Rotating wall in reverse direction, to that of the magnetron, results in the expansion of the positron cloud. (c) Rotating wall in forward direction results in the compression of the positron cloud. The color bars indicate the pixel intensity.

where E is the total energy and ϕ the axial electric potential. The integration limits, z_1 and z_2, correspond to the axial positions in which $E = \phi$. To compute the magnetron frequency f_m (equation 4.8 in Chapter 4) it was assumed that the magnetic field in the bottom of the well of the second stage is of the order of 460 G. Figure 5.15a shows a plot of f_0 as a function of the positron kinetic energy. The red horizontal bar corresponds to f_0 in the range between 7.2 MHz and 7.5 MHz, and the green band correspond to the respective kinetic energy. From the rotating wall frequency that resulted in maximum compression, $f_{\mathrm{RW}} = 7.34$ MHz, the mean axial kinetic energy can be estimated to be 480 meV. Deller *et al.* [96] reported that a positron cloud confined in a similar well of the Swansea trap, has a mean kinetic energy of $\sim$400 meV. Figure 5.15b shows in orange the respective integration region.

Figure 5.16 shows three images of a positron cloud captured by the CCD camera. For each image a sequence trap-close injection-ejection was executed, with the trapping

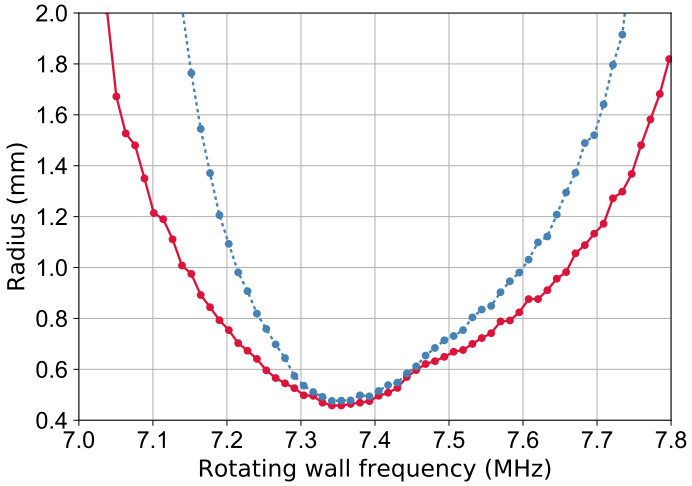

(a)

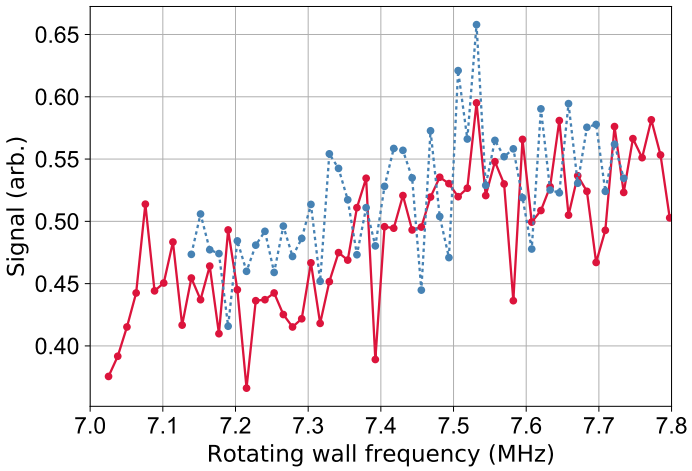

(b)

Figure 5.14: Rotating wall frequency scan for two amplitudes: (- -) 0.3 V, (—) 0.4 V. (a) The positron cloud radius defined as a function of the rotating wall frequency. Maximum compression, corresponding to minimum radius, is observed for $f_{\mathrm{RW}} = 7.34\,\mathrm{MHz}$, for both amplitudes. (b) The CsI signal as a function of the rotating wall frequency. The lines connecting the data points are drawn to help the eye.

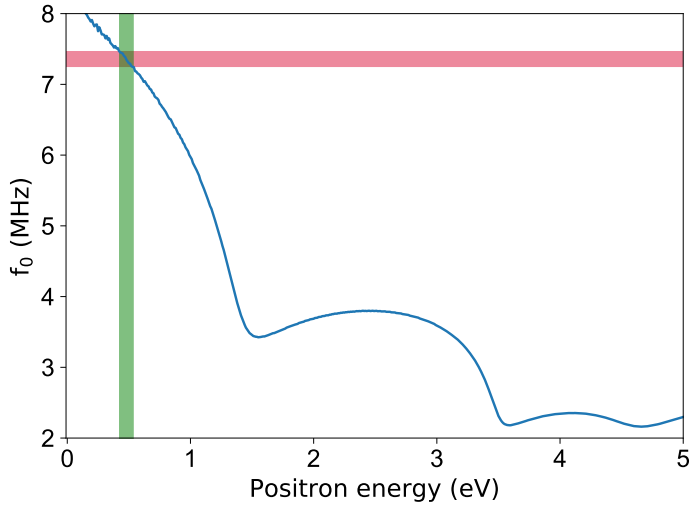

(a)

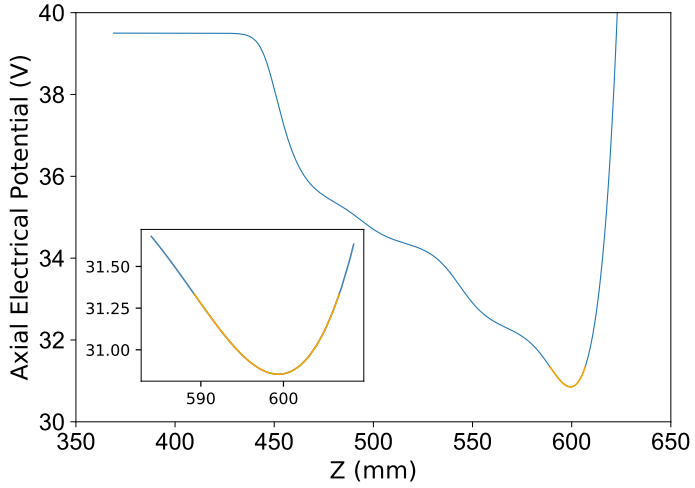

(b)

Figure 5.15: Estimation of the central frequency frequency, f_0. (a) Central frequency f_0 as a function of the positron kinetic energy. The red horizontal bar corresponds to the resonant range between 7.2 MHz and 7.5 MHz, and the respective energy range is given by the vertical green bar. (b) The resonance frequency obtained experimentally $f_0 = 7.34$ MHz corresponds to a positron cloud with mean kinetic energy 480 meV. The axial electrical potential of the second stage well is shown (—) as well as the integration region for this energy (—).

phase lasting 100 ms. The rotating wall was employed throughout the trapping procedure and with an amplitude of 0.3 V. The images were rotated by 45°, and the top and right plots correspond to the intensity curve of the x and y cross-section through the maximum of the 2d Gaussian fit. The σ_x and σ_y resulting from fit are also shown. In figure 5.16a the applied rotating wall frequency, f_{RW}, was 8 MHz, while in figure 5.16b it was $f_{\mathrm{RW}} = 7.15$ MHz and in figure 5.16c, $f_{\mathrm{RW}} = 7.34$ MHz which corresponds to maximum compression. One can observe that as the rotating wall frequency approximates the resonant frequency, the beam profile approximates a Gaussian distribution.

Trapping positrons for 100 ms forms a positron cloud with roughly 3000 positrons. It is possible to estimate the Debye length using the computed mean kinetic energy of the positron cloud (480 meV), knowing that the cloud length, L, is approximately 17 mm and its radius $r = 0.44$ mm. The Debye length is therefore $\lambda_D \sim 9$ mm. Given that $\lambda_D \sim 0.5 \times L$ and $\lambda_D \sim 21\ r$, one can conclude that the positron cloud is significantly below the plasma threshold ($\lambda_D << L, r$ [97]). It is, therefore, safe to assume that the positron cloud is in the single particle regime.

5.1.6 Parallel energy distribution

The parallel energy distribution of the positrons trapped in the second stage was measured with the moderator magnetic field equal to 133 G, hence the applied potentials correspond to those described in table 5.1. The measurement was performed using the RPA technique described in Chapter 3, but using the electrodes of the third stage as a retarding potential analyzer. Their voltage, V_3, was varied from 10 V to 30 V, so that only the positrons with $E_{\parallel} > V_3$ can overcome this potential barrier and annihilate on the MCP. The configuration of the axial electrical potential during this measurement is shown in figure 5.18. The positron annihilation signal was measured by the caesium iodide detector.

The integral of the energy distribution of the positrons after 100 ms accumulation with N_2 pressure $5.5{\times}10^{-5}$ mbar can be seen in figure 5.18. The complementary error function fit yielded $\sigma_{\parallel} = 1.08 \pm 0.06$ eV, $\Delta E_{\parallel} = 2.54 \pm 0.09$ eV FWHM and $\mu = 22.55 \pm 0.05$ eV. Even though the bottom of the positron well corresponds to 30.67 V (computed with SIMION), the mean parallel energy of the positrons is 22.55 eV, and the maximum parallel energy is smaller than 26 eV. Assuming the mean kinetic energy of the positrons in this well is 950 meV (this value was obtained using the same technique described in the previous section, in which one can estimate the mean kinetic energy knowing the rotating wall resonant frequency, and therefore the axial bounce frequency) then the positrons lost on average 9 eV between the second and the third stage.

An energy loss mechanism that can be envisioned is adiabatic cooling during the lowering of the second stage exit potential barrier. In a Penning-type trap the axial bounce is an adiabatic invariant,

$$J \sim v_{\parallel}\, w\,, \tag{5.10}$$

where w is the width of the potential well. In this situation the positrons can be cooled down if the well size is increased. However, this invariant is only conserved if the change in the well size is slower than the positrons' axial bounce frequency. For this

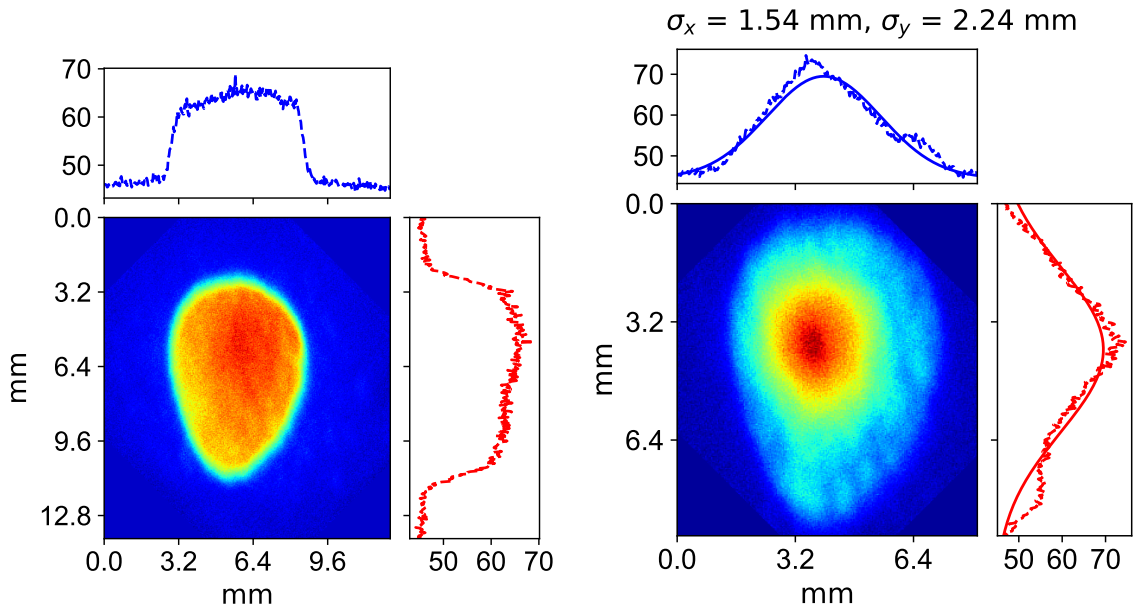

(a)

(b)

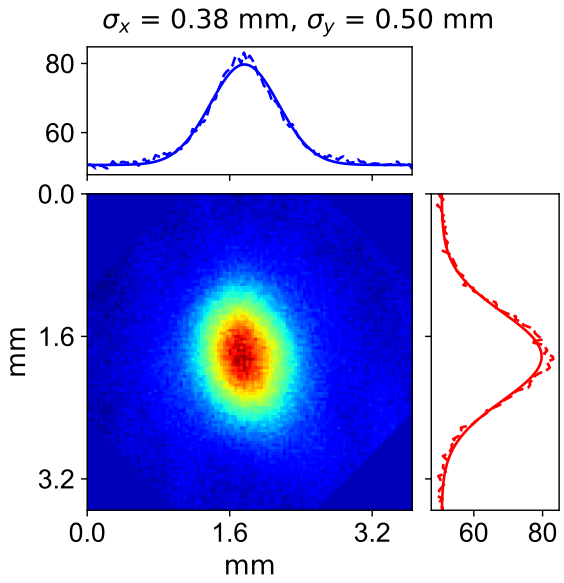

(c)

Figure 5.16: Image of positron cloud and respective intensity curve for three rotating wall frequencies. (a) $f_{\mathrm{RW}} = 8\,\mathrm{MHz}$, (b) $f_{\mathrm{RW}} = 7.15\,\mathrm{MHz}$ (c) $f_{\mathrm{RW}} = 7.34\,\mathrm{MHz}$ corresponding to maximum compression. The images were rotated by 45°, and the top and right plots correspond to the intensity curve of the x and y cross-section through the maximum of the 2d Gaussian fit. The σ_x and σ_y resulting from the fit are also shown. Note that the scales of the cloud images are different.

well, a scan of the rotating wall frequency revealed that the the resonant frequency is approximately 8.98 MHz, corresponding to an axial bounce frequency of the order of 8.9 MHz. This gives a time scale of the round trip inside the well, of ∼100 ns, while the positrons are ejected in less than 80 ns by a fast switch. One would then expect that the fast ejection would not influence the parallel energy of the positrons. In order to prove, or disprove, this hypothesis one could envision to vary the time scale of the positron ejection by controlling the fall rate of an amplifier, instead of using a switcher. For different ejection speeds, the integral of the energy distribution could be measured to establish a relationship between $\bar{E}_{\parallel}$ and the ejection time scale. If $\bar{E}_{\parallel}$ turns out to be constant, then one can safely assume that adiabatic cooling is not at play.

An alternative, and more realistic, explanation is that the positrons are decelerated by the last electrode of the second stage. When the exit barrier of the second stage is lowered, the positrons that were confined in the potential well pass through the end electrode, while it is being ramped down at 1.75 V/ns. This is the exact same principle of a decelerator (the opposite of an elevator). This hypothesis could be verified in a similar way as the previous one, i.e. by varying the fall speed of the barrier potential and determining the respective energy distribution. If this hypothesis is correct then one would observe a different energy loss, dependent on the fall rate. Care must be taken to avoid adiabatic cooling, meaning the end barrier potential should not be lowered in a longer time scale than the positrons bounce frequency.

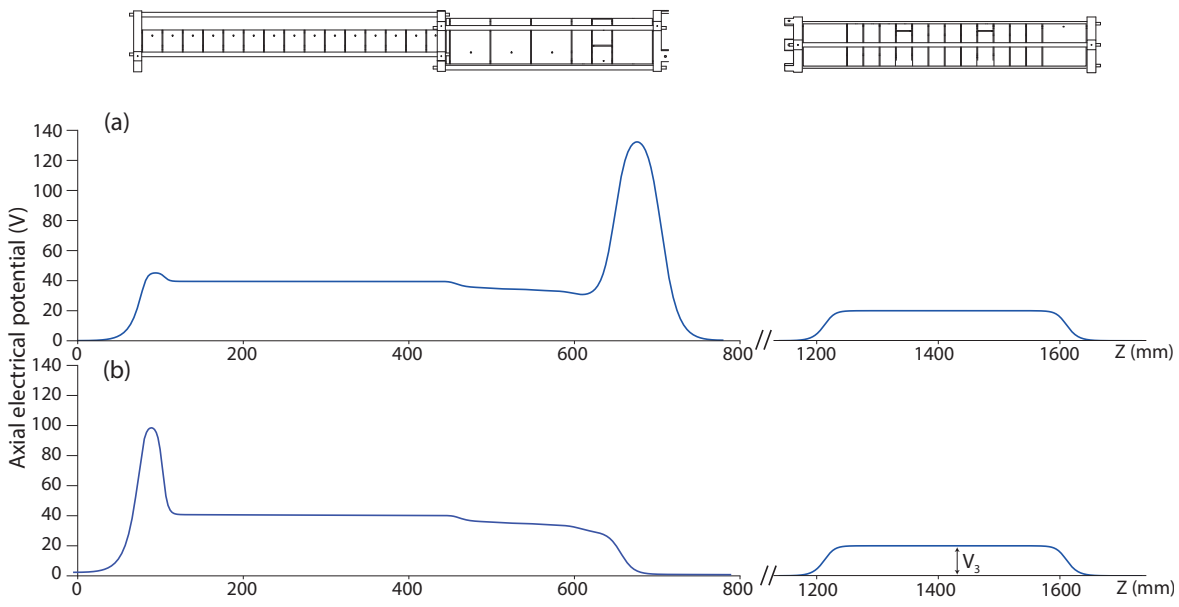

Figure 5.17: Configuration of the axial electrical potential during the measurement of the parallel energy distribution. The potential of the third stage, V_3, is varied to function as a retarding potential analyzer. Downstream of the third stage there is a MCP which was used as target. (a) The axial electrical potential during the trapping phase. (b) The axial electrical potential during the ejection phase.

A Monte Carlo simulation, similar to the one effectuated by Natisin [98], of the ejection protocol could provide a valuable insight to this problem. Given the potential well simulated with SIMION, one could simulate the positron spatial distribution in the well, as well as the velocities distribution in order to model the motion of the particles while the end barrier is lowered. This simulation could help in understanding how to better tailor the positron beam ejected out of the third stage, described at the end of the chapter.

The identical mean parallel energy observed when only N_2 is present and when SF_6 is added (8×10^{-6} mbar measured by the pressure gauge P10), but the rotating wall is on, suggests that the SF_6 gas is counteracting the rotating wall heating. Moreover, when the rotating wall is off, the cooling gas is cooling the positrons.

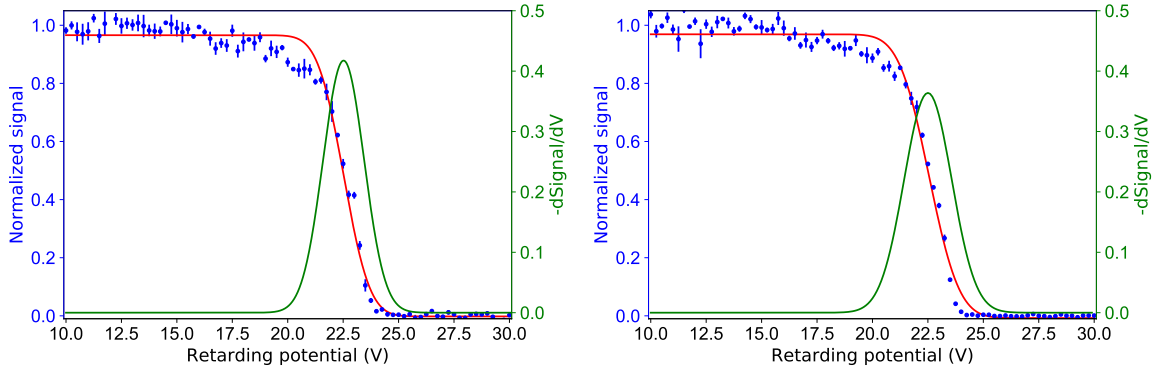

(a) (b)

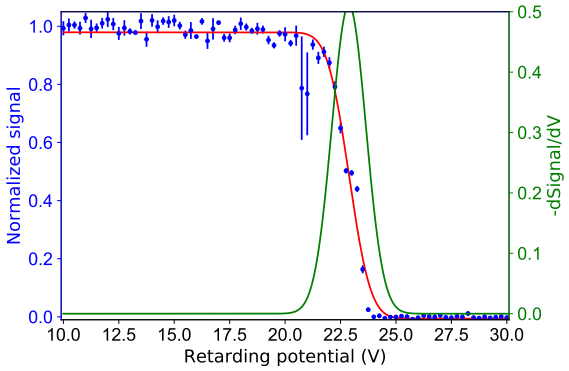

(c)

Figure 5.18: The integral of the positrons' parallel energy distribution 100 ms accumulation (•) fitted to the complementary error function (—), and the respective derivative (—). (a) Only N_2 was present. The fit yielded $\sigma_{\parallel} = 1.08 \pm 0.06$ eV, $\Delta E_{\parallel} = 2.54 \pm 0.09$ eV FWHM, $\mu = 22.55 \pm 0.05$ eV; (b) Both N_2 and SF_6 were present and the rotating wall was on ($f_{RW} = 8.98$ MHz, 0.3 V). The fit yielded $\sigma_{\parallel} = 1.07 \pm 0.06$ eV, $\Delta E_{\parallel} = 2.52 \pm 0.09$ eV FWHM, $\mu = 22.55 \pm 0.04$ eV; (c) Both N_2 and SF_6 were present and the rotating wall was off. The fit yielded $\sigma_{\parallel} = 0.77 \pm 0.06$ eV, $\Delta E_{\parallel} = 1.8 \pm 0.1$ eV FWHM, $\mu = 22.88 \pm 0.04$ eV.

5.2 Third stage accumulation

The third stage of the buffer gas trap was designed to be able to contain two separate potential wells, each with its respective rotating wall. For the experiments described here, two simple square wells were employed. While the first captures the positrons from the second stage, the second well accumulates them in a lower pressure region. The accumulation technique comprises four phases and is schematically represented in figure 5.19. In the first phase, the positrons trapped in the second stage are transfered to the first well of the third stage when the potential of the exit barrier is lowered. Once the positrons reach the third stage, the potential of its first electrode is raised, confining the positrons in the first square well. The rotating wall is then applied for a short time. Afterwards, the positrons are transfered to a second deeper well and the rotating wall is also applied. The procedure of capturing and transferring the positrons to the second well can be repeated multiples times. Once the accumulation phase finishes, the potential of the last electrode of the third stage is lowered by a fast switch, and the positrons escape from the trap. The third stage accumulation can be summarized in the following steps:

1. Transfer the positrons from the second stage to the third stage.
2. Axially compress the first well of the third stage.
3. Apply the rotating wall (RW2) in this well for T ms.
4. Transfer the positrons to the second well.
5. Apply the rotating wall (RW3).
6. Repeat steps 1 to 5 until the desired number of positrons is achieved.
7. Eject the positrons.

While the steps 2 to 5 are being executed, the first and second stage are continuously accumulating positrons to be ready for step 1. The rest of this section is dedicated to the study of the steps 1 to 7.

5.2.1 Third stage capture optimization

The capture of positrons by the third stage requires careful timing between the moment the positrons are expelled from the second stage, and the moment the potential barrier of the first well is raised. If this period is too short, there is a risk that some of the positrons, if not all, are reflected by the potential barrier of the first well when it is closing; if the period is too long the positrons are able to be reflected by the first well and go back to the second stage. Added to that, the switches responsible for lowering and raising these potentials have different speeds, thus the time between lowering and raising the potential barriers needs to be optimized, to maximize the number of captured positrons.

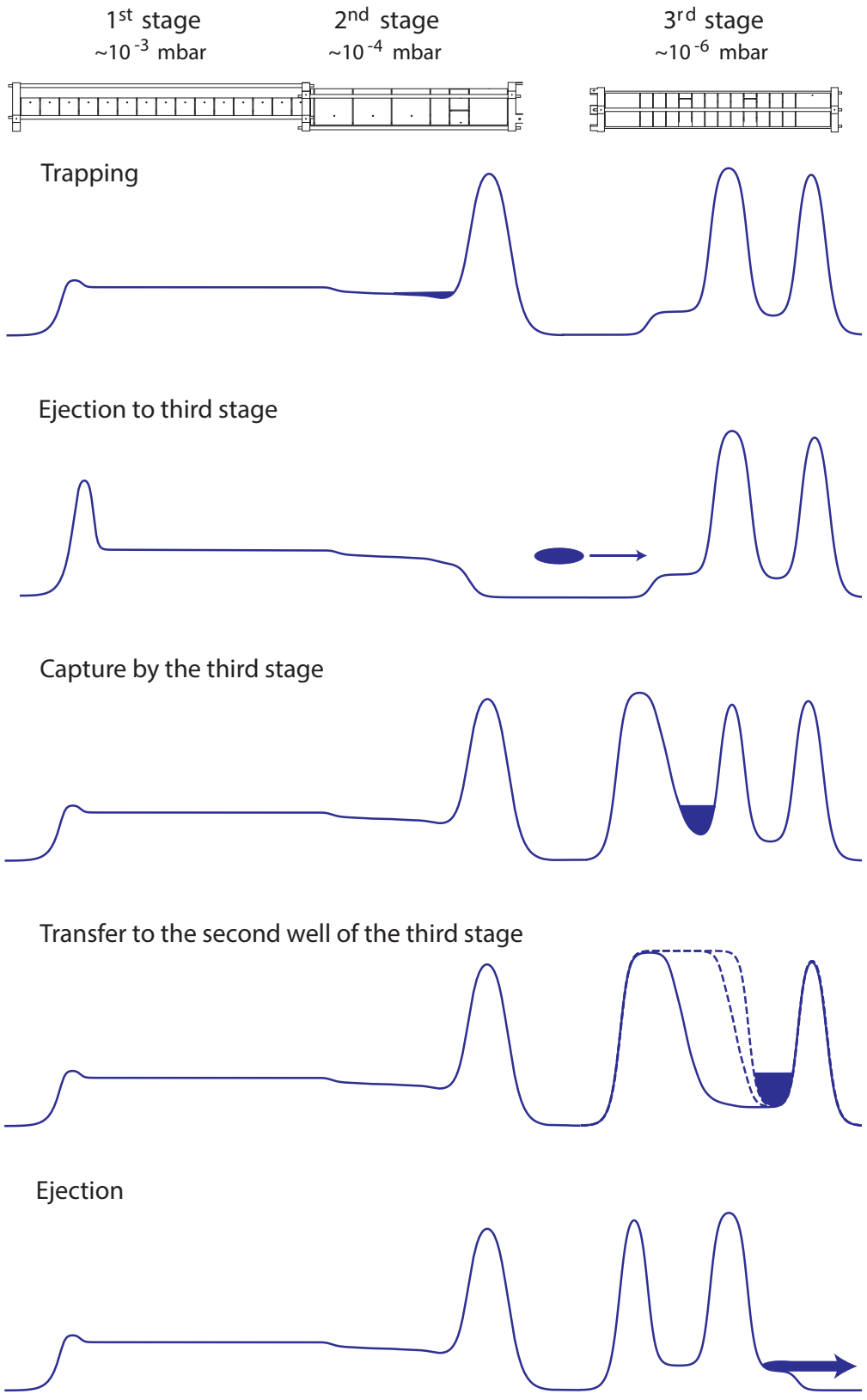

Figure 5.19: Schematic diagram of the axial electrical potential during the positron accumulation in the third stage.

The optimization protocol consists of trapping the positrons in the first and second stage for 100 ms, transfer them to the third stage, and then ejecting the positrons onto a target (the MCP) to measure the annihilation signal using a CsI detector. This protocol was repeated for different transfer times, i.e. the time between lowering the end barrier of the second stage and raising the barrier of the first well of the third stage. The result can be seen in figure 5.20, which shows the positron annihilation signal as a function of the transfer time. The signal was normalized to the signal obtained from trapping the positrons in the first and second stage during 100 ms. Four electrodes were used to form the first well of the third stage. The well depth was set to 19 V. The many peaks that can be observed as the transfer time increases, show that the positrons are able to reflect between the second stage and the the third stage. Figure 5.20b shows the integral of the peaks of figure 5.20a, revealing that 8.7% ± 0.2% of the positrons are lost for each round trip between the second and the third stage. The positron loss is most likely due to the magnetic field variation that increases the positron cloud radius while traveling through cross II, resulting in the collision of positrons with the walls of a pumping restriction that was located upstream the third stage. The radial transport due to the buffer and cooling gas can also be responsible for the observed loss, as well as positronium formation. A transfer time of 275 ns results in 90% capture efficiency.

The optimization procedure was repeated with five electrodes forming the first well [1]. The comparison between this measurement and the one corresponding to four electrodes is shown in figure 5.21. One can see that the curve corresponding to five electrodes is shifted to the right. This effect is due to the larger distance between the second stage and the end of the first well of the third stage, as it is formed by one extra electrode. For a 5 electrode well a transfer time of 325 ns results in 93% capture efficiency.

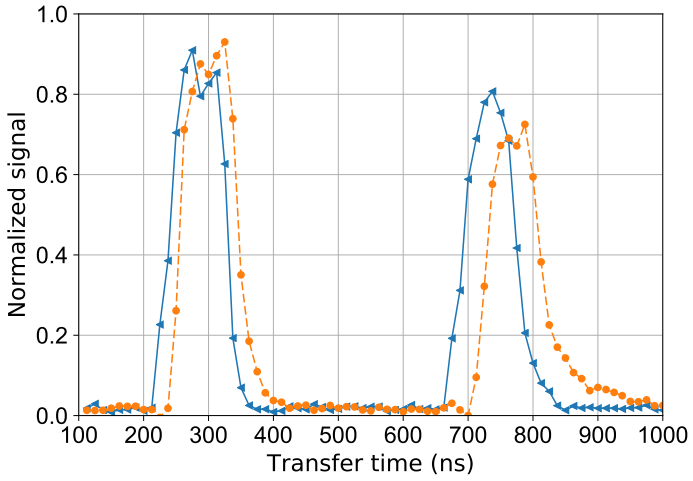

Figure 5.21: Transfer time between the first and the second well of the third stage for a well composed of (◀ —) 4 electrodes, and another composed of (● —) 5 electrodes. The positron annihilation signal measured by a CsI detector was normalized to the signal obtained from trapping the positrons in the first and second stage during 100 ms.

[1] 4 electrodes correspond to 7.39 cm and 5 electrodes to 9.2 cm.

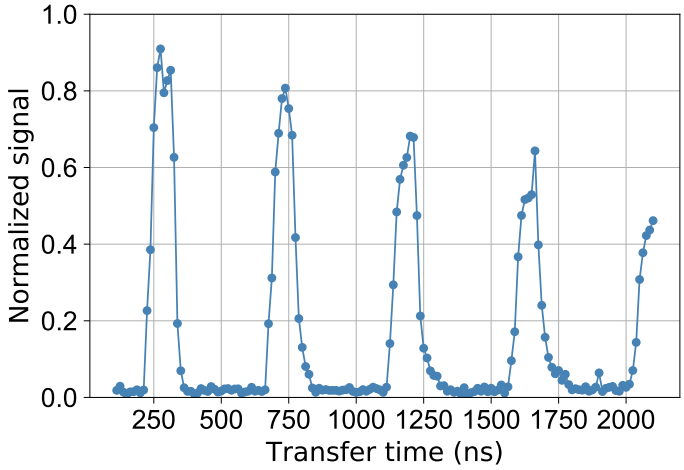

(a)

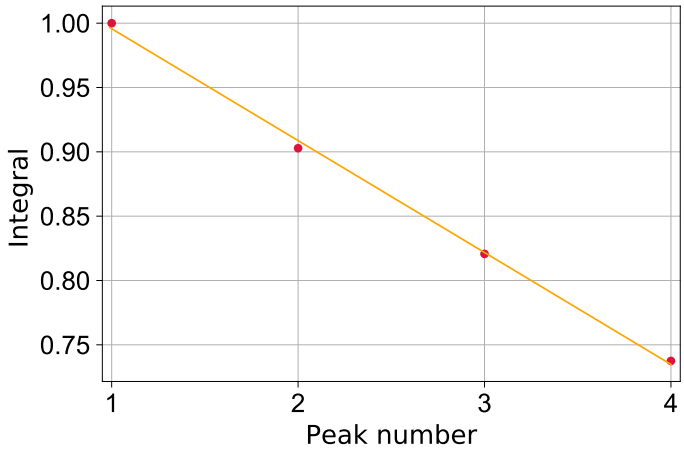

(b)

Figure 5.20: Optimization of the transfer time between the second and the third stage. Four electrodes were used to form the first well of the third stage, with a depth of 19 V. (a) Normalized CsI signal as a function of the transfer time. The positron annihilation signal measured by a CsI detector was normalized to the signal obtained from trapping the positrons in the first and second stage during 100 ms. The lines connecting the data points were drawn to help the eye. (b) The integral of the peaks of figure (a) showing the loss of positrons between the second and the third stage. A linear fit yielded a 8.7% $\pm$ 0.2% loss of positron for each round trip. The integral values were normalized to the integral of the first peak.

5.2.2 First well

Potential depth optimization

The potential depth of the first well of the third stage was optimized. The optimization protocol was identical to the one employed to optimize the positron capture, except that in this case the well depth was varied, and can be viewed in figure 5.22.

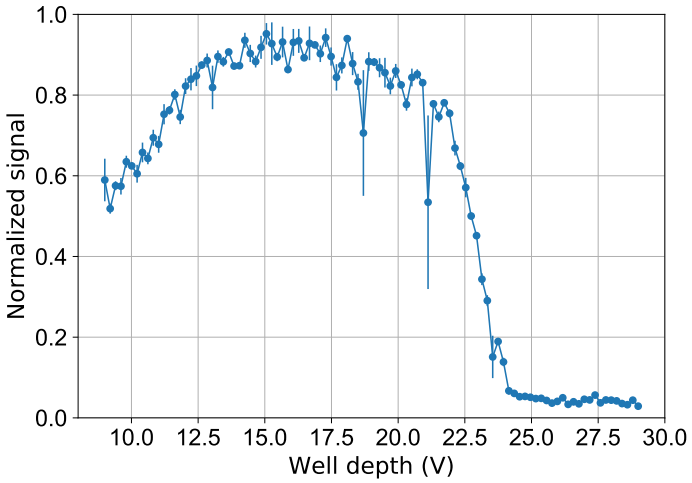

Figure 5.22: Optimization of the potential depth of the first well of the third stage. The positron annihilation signal measured by a CsI detector was normalized to the signal obtained from trapping the positrons in the first and second stage during 100 ms.

As it was shown by the energy distribution measurement, the positrons are not energetic enough to overcome a potential barrier of 24 V, thus the steep slope observed at around this potential depth. On the other hand, for low potential depths the particles are very energetic and the transfer time is too slow to capture all the positrons, hence the smaller signal. The well depth and the transfer time are coupled parameters so they should be optimized as a function of one another.

Cooling time optimization

Before being transfered to the second well of the third stage, the positrons are kept in the first well during a short time to cool down, while the rotating wall is applied. Figure 5.23 shows the result of the optimization of the time during which the rotating wall is applied, and reveals that after $\sim$ 50 ms the number of trapped positrons achieves a maximum limit. A scan of the rotating wall frequency revealed that the optimal frequency for this well is roughly 7.4 MHz and an amplitude of 1.5 V.

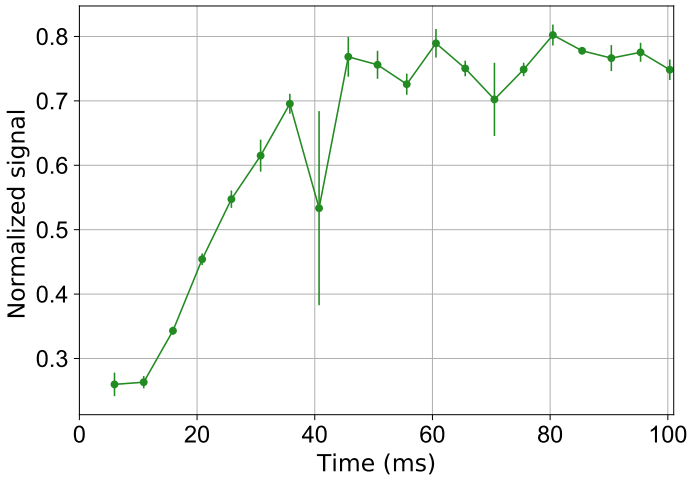

Figure 5.23: Optimization of the time during which the rotating wall is applied in the first well of the third stage. The positron annihilation signal measured by a CsI detector was normalized to the signal obtained from trapping the positrons in the first and second stage during 100 ms.

The transfer of positrons from the first well to the second well is done by first transforming the first well into a ramp (140 V to 19 V), and then by gradually increasing the potential of each electrode, comprising the first well, to 140 V. This has the effect of shortening the well from left to right, pushing the positrons to the second well. The transfer procedure is shown in figure 5.19. Measurements have shown that this protocol for transferring the positrons has an efficiency of 85% to 90%.

5.2.3 Second well

Lifetime

The main characteristic of the third stage is that the buffer and cooling gas pressure are significantly lower, to allow the longer confinement of positrons. The lifetime of the positrons is therefore a good indicator of the quality of the trap, specifically the vacuum, the potential well and the alignment of the electrodes with the magnetic field lines. To estimate the lifetime in the second well of the third stage, an accumulation curve was done, consisting of monitoring the number of positrons, given by the annihilation signal in the CsI detector, as a function of the number of stacks. Each stack corresponds to a 100 ms accumulation in the first and second stage, followed by capture and transfer to the second well of the third stage.

The measured lifetime was 2.16 ± 0.05 s, which is much shorter than the ∼16 s annihilation lifetime expected at this pressure [2]. To reduce the pressure in the third stage even further, a pumping restriction, consisted of a tube with 20 cm length and 1.6 cm diameter, was inserted immediately before the third stage. Another accumulation curve was performed, shown in figure 5.24, yielding a lifetime of 4.45 ± 0.09 s.

[2]The pressures were Cross II: 7.2×10^{-6} mbar for SF_6 and 3.2×10^{-5} mbar for N_2; Cross III: 2.6×10^{-7} mbar for SF_6 and 2.3×10^{-6} mbar for N_2.

In spite, of the addition of the pumping restriction, the lifetime did not improve as expected. The annihilation lifetime for the pressure[3] obtained with this pumping restriction should be approximately 86 s. It seems, therefore, that the amount of cooling and buffer gas pressure is not the dominant effect that causes the reduction of the positron lifetime. This result is highly consequential, since the number of positrons the third stage is able to confine is strongly limited by the small lifetime. Baking the trap should solve this problem if the quality of the vacuum is the major problem. If this does not help, then the solenoid and coils should again be carefully aligned with the electrode stack.

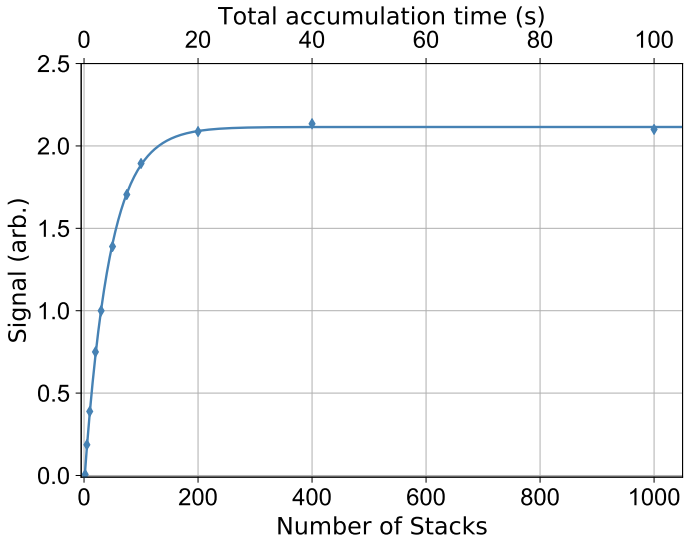

Figure 5.24: Third stage accumulation curve fitted to equation 5.2, yielding $R = 0.49 \pm 0.01$ arb./s and $\tau = 4.45 \pm 0.09$ s. The total accumulation time corresponds to the number of stacks multiplied by 100 ms, which corresponds to the accumulation time of each stack.

Rotating wall

The rotating wall frequency was optimized in the same way as the one in the second stage, i.e. the cloud radius and the number of trapped positrons were monitored while scanning the frequency. For each frequency the trapping phase lasted 100 ms and 10 stacks were accumulated in the third stage. Afterwards, the positrons were ejected into a MCP, and the phosphor screen image was registered by a CCD camera, while a CsI detector registered the annihilation signal. The image processing was identical to the second stage analysis. The results of the scan are shown in figure 5.25.

Unlike the single particle regime, in which compression is observed for frequencies close to the central frequency f_0, figure shows that compressions is achieved for a large range of frequencies. This behavior is akin to the one observed in the strong drive regime in non-neutral plasmas.

[3]The pressures with the pumping restriction were Cross II: 9.12×10^{-6} mbar for SF_6 and 5.32×10^{-5} mbar for N_2; Cross III: 5.64×10^{-8} mbar for SF_6 and 5.46×10^{-7} mbar for N_2.

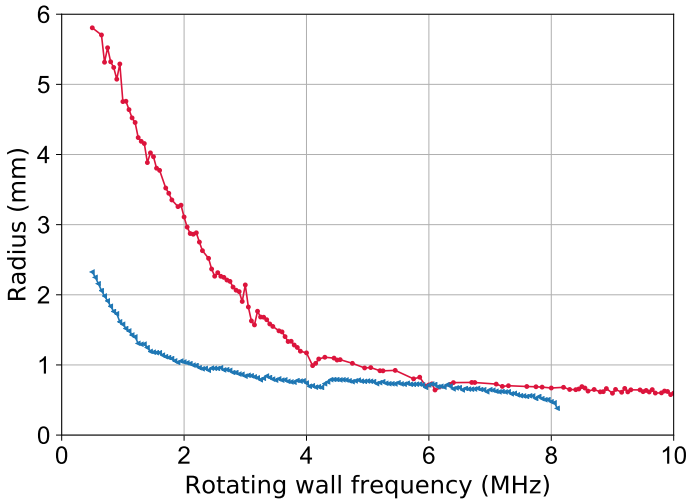

(a)

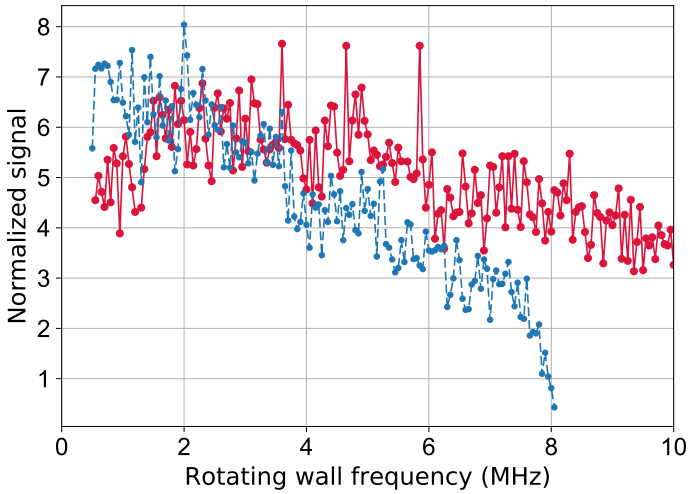

(b)

Figure 5.25: Rotating wall frequency scan for two well lengths: (- -) 5 electrode well and (—) 4 electrode well. The rotating wall amplitude applied was 10 V. (a) The positron cloud radius as a function of the rotating wall frequency. (b) Normalized CsI signal as a function of the rotating wall frequency. The positron annihilation signal measured by a CsI detector was normalized to the signal obtained from one positron pulse from the LINAC. The lines connecting the data points were drawn to help the eye.

However, a behavior characteristic of the single particle regime was also evident for low rotating wall amplitudes (0.15 V to 1 V) and frequencies close to 7.1 MHz. In the latter case, compression was not observed for rotating wall frequencies smaller than 6 MHz and larger than 8 MHz, while maximum compression was observed for 7.1 MHz. It appears that this positron cloud is in a transition regime between the single particle and the plasma regime.

Figure 5.25a shows what seems to be two distinct compression regimes. In the first one, corresponding to frequencies from 0 MHz to roughly 2 MHz for the 5 electrode case, and 0 MHz to 4 MHz in the 4 electrode case, the positron cloud radius drops quickly with increasing rotating wall frequency. In the second regime, corresponding to higher frequencies, the radius decreases slowly and linearly. The latter regime corresponds to a decrease of the amount of trapped positrons, observed in figure 5.25b, suggesting that large frequencies result in positron loss. It might be possible that this loss is due to heating provoked by the large rotating wall frequencies. To confirm this hypothesis, this measurement could be repeated for different cooling gas pressures. If the amount of cooling gas is indeed the factor influencing this behavior, then when the pressure is reduced, the annihilation signal should drop for lower rotating wall frequencies; while increasing the amount of gas would lead to a drop for higher frequencies. A disadvantage of this measurement is that the amount of coolings gas also affects the second stage. Thus, care must be taken to ensure that the beam formed in this stage is not affected. One could also envision to increase (decrease) the rotating wall amplitude, if the amount of gas is increased (decreased).

It would also be interesting to repeat this measurement for several rotating wall amplitudes, to see if a similar behavior also occurs. Indeed, the rotating wall amplitude applied in the described measurement is quite high and it is possible that the cooling gas was simply not enough. If what was observed is the strong drive regime, then significantly lowering the amplitude would disengage the strong drive and drastically reduce the compression.

A rotating wall amplitude scan is presented in figure 5.26 for rotating wall frequency 7.1 MHz. It reveals that when compression is achieved, the radius is independent of the amplitude. On the other hand, the amount of trapped positrons, proportional to the annihilation signal, and shown in figure 5.26b, decreases with increasing amplitude due to the fact that the cooling gas cannot keep up with the increasing rotating wall heating [99].

Figure 5.27a shows the positron cloud radius as a function of the number of stacks accumulated in the third stage. Figure 5.27b shows that the radius increases linearly with the number of positrons.

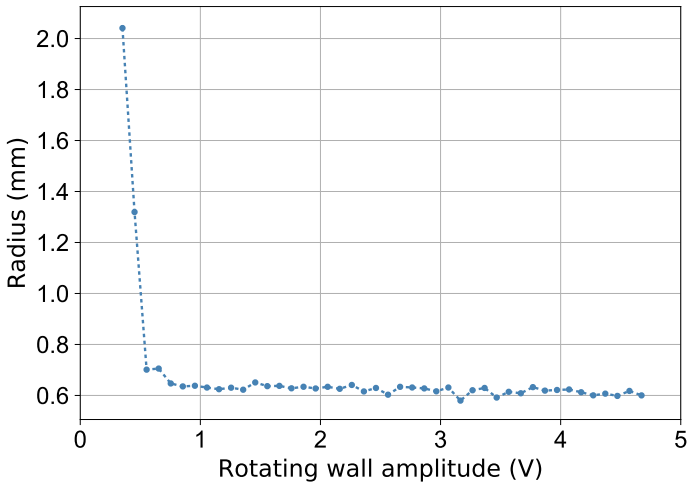

(a)

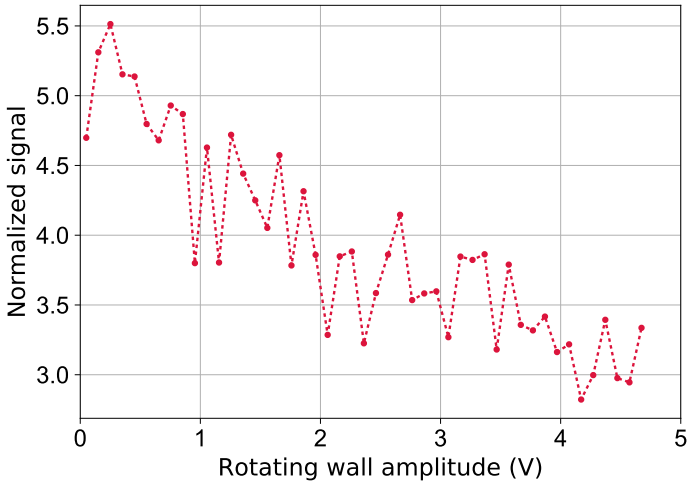

(b)

Figure 5.26: Rotating wall three amplitude scan for frequency 7.1 MHz. (a) Positron cloud radius and (b) Normalized CsI signal as a function of the rotating wall amplitude. The positron annihilation signal measured by a CsI detector was normalized to the signal obtained from one positron pulse from the LINAC.

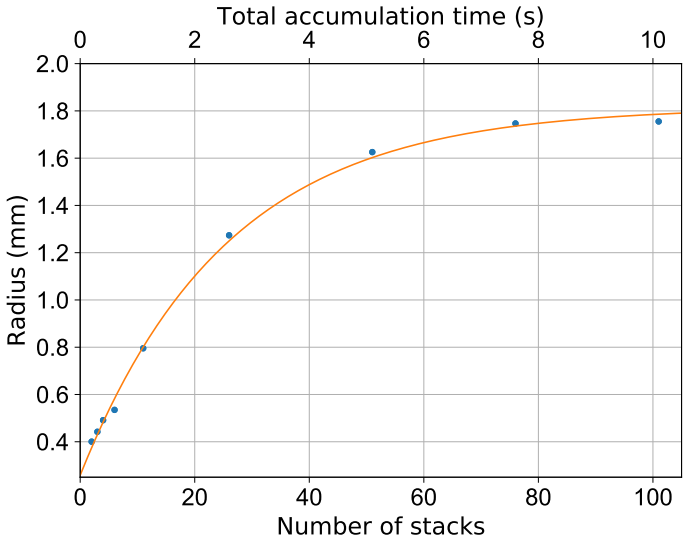

(a)

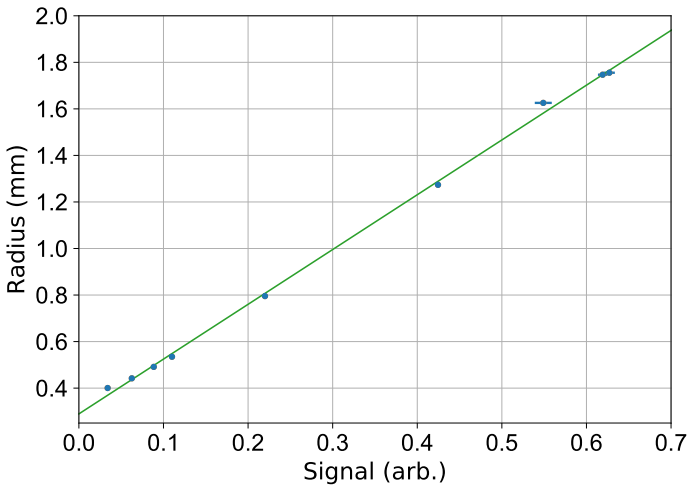

(b)

Figure 5.27: Positron cloud radius as a function of the number of (a) stacks and (b) number of positrons.

5.3 Characterization of the positron beam

In this section the positron beam formed by the third stage is characterized, including the time distribution and the radial profile. A small part is dedicated to the description of how the energy distribution of the beam can be ascertained.

5.3.1 Time distribution

The time distribution of the positron beam was measured by expelling the positrons from the third stage, by lowering the exit barrier with a fast switch. For this measurement a fast plastic detector with a time resolution of $\sim 7\,\mathrm{ns}$ was employed to measure the positron annihilation signal. Figure 5.28 shows the time distribution of the positron beam ejected from the third stage of the buffer gas trap. The data points were fitted to an exponentially modified Gaussian distribution that has the form

$$f\left(x;\mu,\sigma,\lambda\right) = \frac{\lambda}{2}\, e^{\frac{\lambda}{2}\left(2\mu+\lambda\sigma^2-2x\right)}\,\mathrm{erfc}\left(\frac{\mu+\lambda\sigma^2-x}{\sqrt{2}\sigma}\right) \tag{5.11}$$

to account for the exponential decay of the detector's scintillation. Erfc corresponds to the complementary error function. The fit yielded $\sigma = 1.91 \pm 0.04\,\mathrm{ns}$, $\Delta\mathrm{t} = 18.2\,\mathrm{ns}$ FWHM, $\tau = 1/\lambda = 18.3 \pm 0.2\,\mathrm{ns}$ and $\bar{\mathrm{t}} = 647.49 \pm 0.03\,\mathrm{ns}$. The full-width at half-maximum from the fit is overestimated, but by computing it directly from the data points one obtains $\Delta\mathrm{t} = 15\,\mathrm{ns}$ FWHM.

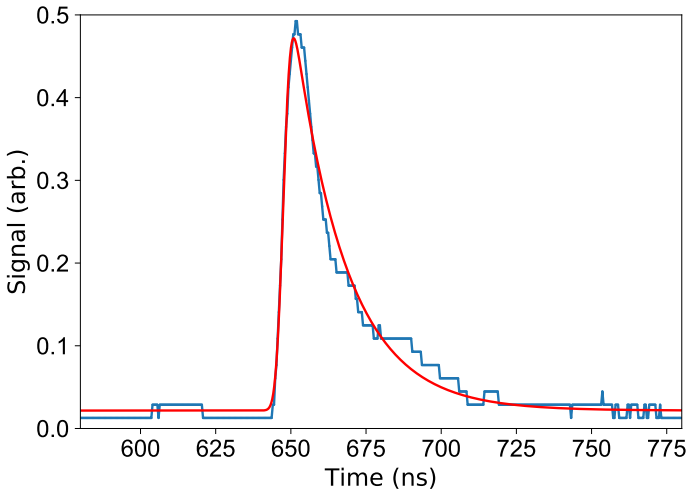

Figure 5.28: Temporal distribution of the positron beam ejected from the third stage of the buffer gas trap. (—) Data points and (—) exponentially modified Gaussian fit. The fit yielded $\sigma = 1.91 \pm 0.04\,\mathrm{ns}$,
$\Delta\mathrm{t} = 18.2\,\mathrm{ns}$ FWHM, $\tau = 18.3 \pm 0.2\,\mathrm{ns}$ and $\bar{\mathrm{t}} = 647.49 \pm 0.03\,\mathrm{ns}$.

In this measurement, the positrons annihilated in the valve that separates the buffer gas trap from the ANTION apparatus, i.e. $\sim$1.5 m from the exit barrier of the third stage. This means that due to the parallel energy spread of the positron beam, the

time spread is expected to vary with the propagation of the beam. It would be interesting to repeat this measurement with the positrons annihilating in the vacuum valve immediately in front of the third stage, to evaluate the variation of the time distribution.

5.3.2 Energy distribution

Unfortunately, the energy distribution of the positron beam was not measured during the course of this thesis due to time constraints. However, given that the MCP used in these experiments does not contain a grid, the distribution measurement could be realized by using the MCP as a RPA, i.e. by varying the front voltage, while keeping the other bias at ground. As was described before this measurement cannot be performed by ejecting the positrons with a switch as it decelerates the positrons. Instead, one could use an amplifier and control how slowly the exit barrier drops. In this case, adiabatic cooling of the positrons would be an issue, thus the measurement should be executed for several ejection speeds.

The before mentioned measurement refers to the parallel energy distribution. To obtain the mean perpendicular energy, the mean parallel energy can be measured for several magnetic field values, followed by the fit of the slope of [98]

$$\bar{E}_{\perp}(B) = -\frac{dE_{\parallel}}{dB}\,. \tag{5.12}$$

The total energy distribution can, in principle, be measured by significantly lowering the magnetic field of the RPA region. In this situation, the perpendicular energy is almost fully converted into parallel energy, allowing for the measurement of the total energy distribution.
A disadvantage of this technique is that the radial profile of the beam explodes for low magnetic fields, hence a large target would be required.

5.3.3 Radial profile

The radial profile of the positron beam ejected out of the second well of the third stage can be observed in figure 5.29. The positron beam corresponds to ten stacks of positrons, each corresponding to 100 ms accumulation in the first and second stage. The applied rotating wall settings were $f_{RW} = 7.1$ MHz and 0.75 V amplitude. The top and right plots correspond to the intensity curve of the x and y cross-section through the maximum of the 2d Gaussian fit. The σ_x and σ_y resulting from fit are also shown, giving a radius of 0.67 mm.

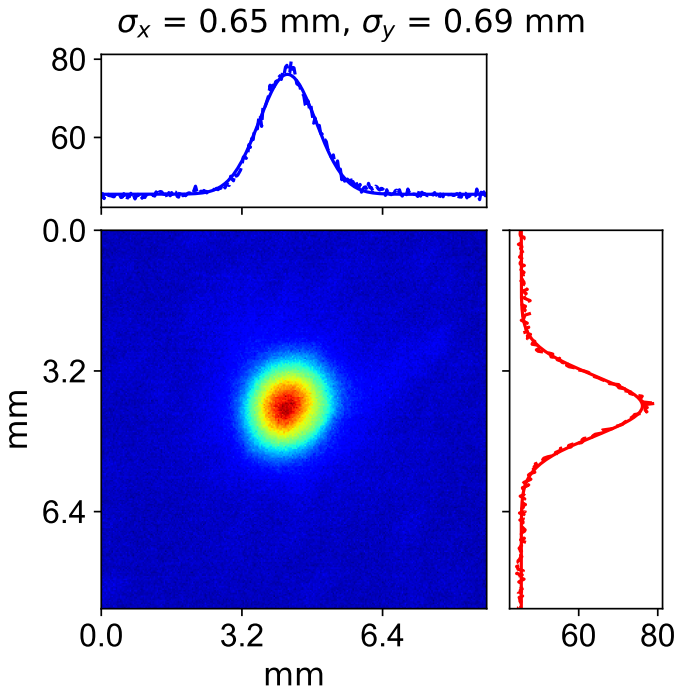

Figure 5.29: Image of the positron beam ejected out of the third stage. The applied rotating wall settings were $f_{\mathrm{RW}} = 7.1\,\mathrm{MHz}$ and 0.75 V amplitude. The top and right plots correspond to the intensity curve of the x and y cross-section through the maximum of the 2d Gaussian fit. The σ_x and σ_y resulting from the fit are also shown, giving a radius of 0.67 mm.

5.4 Conclusion and outlook

The main goal of the experiments described in this chapter was to commission the newly built trap and to have both stages operating as soon as possible, to be able to provide positrons to the ANTION experiment in order to measure the cross section of hydrogen production, while still at Saclay. The goal was achieved and a short, small-sized beam is routinely produced. The maximum number of trapped positrons in the first and second stage was $\sim 4.6\times10^4$, while the maximum number of trapped positrons in the third stage was $\sim 1.2\times10^5$ corresponding to 100 stacks, or a total accumulation time of 10 s. This values could not be reproduced at a later stage due the degradation of the positron flux supplied by the LINAC apparatus. The first and second stage are operating with $\sim$ 12% efficiency.

However, there is still plenty of work that needs to be done to ameliorate the trap performance. Although, the trapping efficiency of the first and second stage is similar to the one reported for the Swansea trap [100], these stages are not operating at optimum conditions. Moreover, the ability of the third stage to accumulate a large number of positrons is being hindered by the small lifetime. This problem should soon be solved by baking the trap if the vacuum conditions are at fault.

At first the buffer and cooling gas pressures, in the first and second stage, should be optimized while the rotating wall is applied. The magnetic field asymmetry observed

between the second and the third stage should be studied in detail. Furthermore, the rotating wall behavior in the third stage should be explored even further to understand if this is indeed the strong drive regime, or an intermediate regime between plasma and single particle.

Part III

The hydrogen cross section Challenge

6 Reaction cavity simulations

"Prediction is very difficult, especially about the future."
Niels Bohr

Contents

The measurement of the hydrogen production cross section relies on the precise determination of the number of ortho-positronium atoms available to interact with a proton pulse. For that reason, a Monte-Carlo simulation was created, and further developed with the help of BongHo Kim, with the goal of estimating the evolution of the ortho-positronium density with time, as well as the expected background from the positron and para-positronium decay. The effect of the type of coating of the cavity is also studied, as well as the effect of the angular distribution of the ortho-positronium atoms. Finally, a prediction of the number of hydrogen atoms produced for the Saclay measurement is made based on the theoretical cross sections.

6.1 The ANTION project

As discussed in section 2.1.1, the ANTION project aims to measure the production cross section of hydrogen and its negative ion, as well as the antimatter reactions that produce antihydrogen and antihydrogen positive ion. Given that the positron source at Saclay provides a smaller flux of positrons, only the first cross section measurement will be attempted before moving the apparatus to CERN. For that reason this chapter will only concern the H cross section.

The ANTION experiment includes the production of a dense positronium cloud (10^{10} Ps/cm^3 density) by implanting positrons on a mesoporous material. A cavity, as opposed to a target, allows for the positronium atoms to be reflected, confining them to a small volume. A proton beam enters the cavity through the side and combines with the positronium atoms to form hydrogen atoms. An electrostatic quadrupole then separates the remaining protons from the neutral hydrogen atoms. The latter follow the same trajectory as the incident protons.

In order to measure the H cross section three quantities should be known with precision: the ortho-positronium density, the number of protons and the number of hydrogen atoms produced. For that reason, the challenge of this experiment will be in setting up an efficient detection system that detects the few hydrogen atoms produced while also minimizing the background that contaminates the detection of the hydrogen atoms and the annihilation signal of the positronium. A microchannel plate detector was chosen to detect both the atoms and the ions because it allows a precise counting. A lead tungstate crystal coupled to a photomultiplier is a fast detector with a good time resolution. For that reason, it is more suited to distinguish the γ-ray photons resulting from positron and para-positronium decay, from ortho-positronium decay. Thus, this detector will be employed to detect the annihilation of the ortho-positronium. A Faraday cup will be used to monitor the current of the proton beam. A schematic drawing of the ANTION apparatus is shown in figure 6.1.

The reaction chamber where the reactions will take place is shown in figure 6.2. This chamber is immediately connected to the buffer gas trap. In the last cross of the trap, cross V, lies a buncher that is used to accelerate the positrons so that they escape the magnetic field and implant on the mesoporous material with 4 keV. Currently, the buncher is being used as an elevator, in which the potential of the electrodes composing the buncher is quickly switched from ground to 4 keV, by a fast transistor switch, when the full positron pulse is inside the buncher. Figure 6.3 shows the time distribution of the positron beam ejected out of the buffer gas trap and the positron pulse after being accelerated. The time spread of the positron pulse is expected to be shortened by the elevator.

After the buncher, the positrons are focused by a set of six Einzel lenses, with alternating potentials (ground - V - ground, etc.). At first a 32 mm diameter MCP will be placed at the center of the chamber, connected by a linear drive, in order to assist the focusing of the positron beam. Later, the MCP will be replaced by a linear drive containing two cavities: one coated with the mesoporous silica, and a second coated with aluminium. The latter will be used for background estimation tests. The vacuum tube containing the lenses is surrounded by an iron cage that shields the electrostatic lenses from the magnetic field of the buffer gas trap.

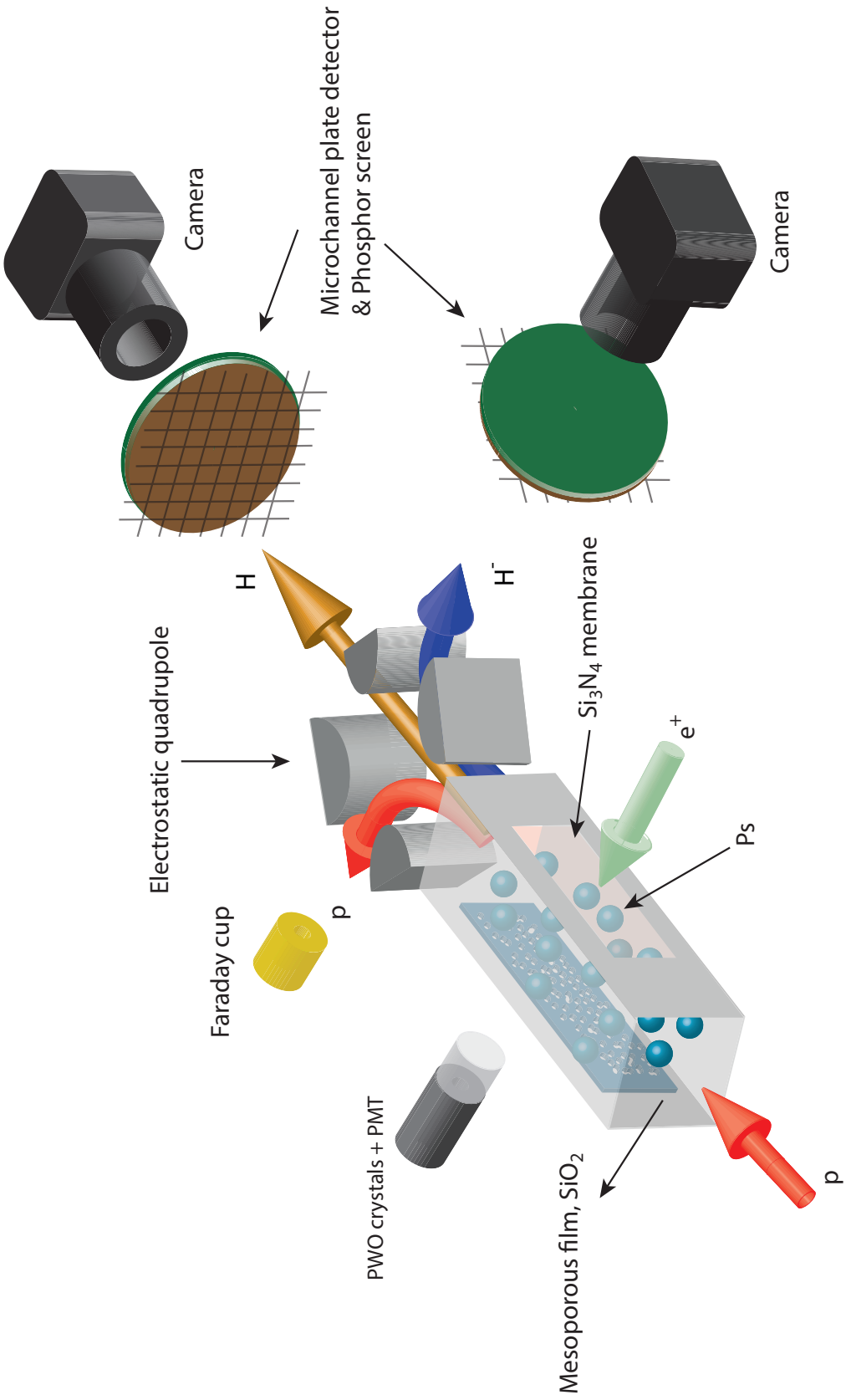

Figure 6.1: Schematic drawing of the ANTION apparatus.

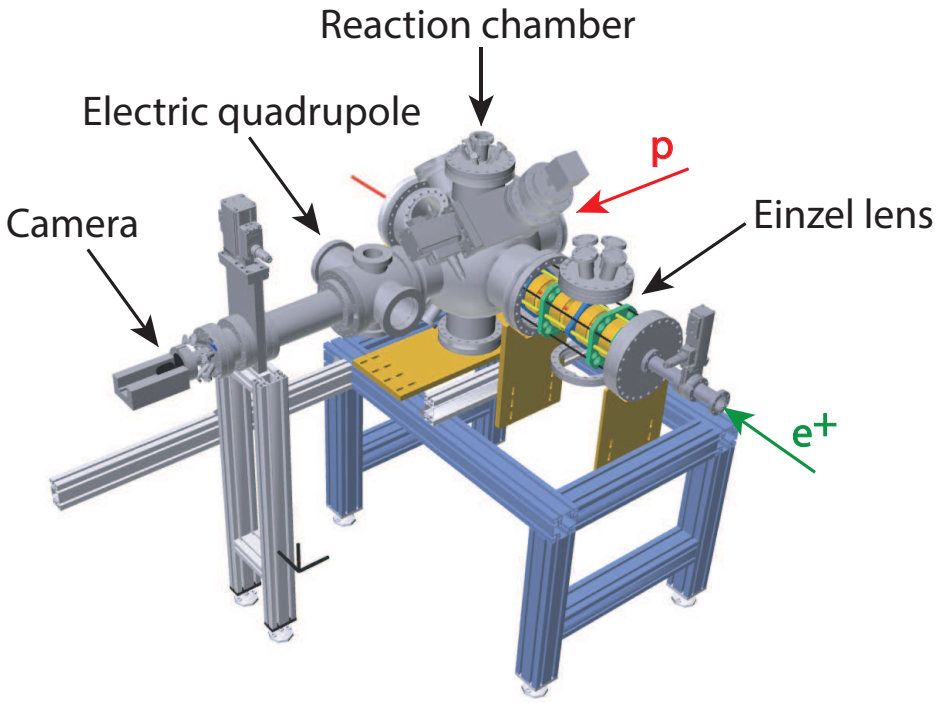

Figure 6.2: CAD drawing of the reaction chamber. The chamber is located downstream from the buffer gas trap. The positron beam is shown in green and the proton beam in red. The reaction cavity will be located inside the reaction chamber. The vacuum tube surrounding the Einzel lens was removed to show the lens system.

The proton beam line is connected to the right side of the reaction chamber. On the opposite side lies an electrostatic quadrupole that separates the protons from the neutral atoms and ions as follows: the protons will be deviated into a Faraday cup, which will measure the current; the hydrogen will continue straight, in the same direction as the original proton beam, until hitting on a microchannel plate detector; and the ions will be deviated to the side and hit another MCP. The reaction chamber is kept at low pressure (10^{-9} mbar) by a cryopump, however when the proton gun is activated, the pressure should increase to 10^{-8} mbar as other ions are also produced by the proton source.

The proton beam generated by a proton gun, consisted of a Penning-discharge ion source fed with gaseous hydrogen, is a continuous beam with of a few microamp current. However, to minimize the dark noise of the MCP the proton beam will be pulsed. This will be achieved by employing a beam chopper in which the beam is deflected across a narrow aperture resulting in a pulsed proton beam with time width in the range 100 ns to 1000 ns.

6.1.1 Reaction Cavity

The positronium target cavity to be used at Saclay has the form of a tube with a square cross section and dimensions 2×2×20 mm. Figure 6.4 shows two pictures of this cavity. The chosen shape has the purpose of confining the positronium atoms inside the small cavity, as they can reflect multiple times in the enclosing walls before annihilating.

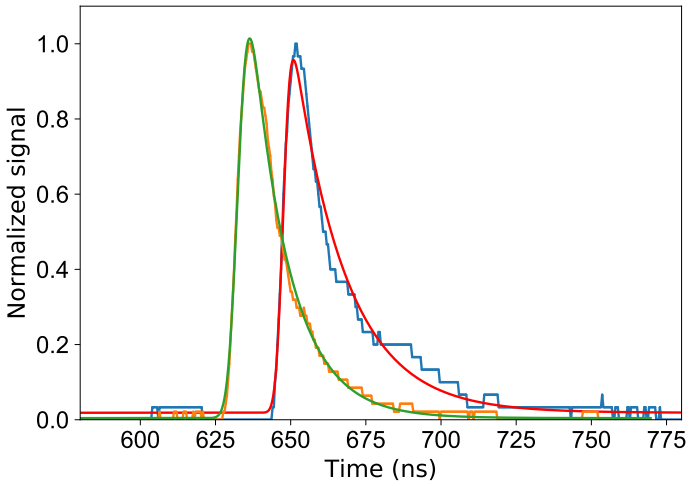

Figure 6.3: Time distribution of the positron beam ejected from the third stage of the buffer gas trap (—) and exponentially modified Gaussian fit (—). The fit yielded σ = 1.91 ± 0.04 ns, Δt = 18.2 ns FWHM, τ = 18.3 ± 0.2 ns and $\bar{t}$ = 647.49 ± 0.03 ns. Temporal distribution of the accelerated positron beam (—) and exponentially modified Gaussian fit (—) . The fit yielded σ = 2.61 ± 0.02 ns, Δt = 15.0 ns FWHM, τ = 12.54 ± 0.08 ns and $\bar{t}$ = 632.61 ± 0.02 ns.

The confinement is important as the (anti)hydrogen ion yield scales with the square of the ortho-positronium density. As described in Chapter 2, the (anti)hydrogen needs to decay into the ground state to greatly increase the $H^-/\bar{H}^+$ cross section.
The decay rate increases with the path length. Even though, at Saclay the goal is to produce only hydrogen, this cavity is a test bench for the cavity that will be used in the final measurements, thus the same geometry is employed but the length is longer by a factor of two.

The positrons enter the cavity through a Si_3N_4 window of 30 nm thickness and 2×10 mm size, held by a silicon frame of 5×14 mm and 200 μm thickness. While allowing the positrons to enter the cavity, this window reflects the positronium atoms, confining them inside the cavity. The protons enter through the 2×2 mm cavity side, and the atoms and ions exit through the other side. The cavity dimensions are a compromise between the positronium density and the capacity to focus the proton beam into the 4 mm^2 cell. On the back of the cavity lies the mesoporous SiO_2 target which consists of a mesoporous silica layer of 1.6 μm thickness on a silica substrate 500 μm thick. The top of the cavity is composed of a fused silica plate with high transmissivity for the $2p$ and $3d$ excitation lasers (243 nm and 410 nm respectively), and the bottom contains an aluminium mirror, to reflect the $3d$ excitation laser, coated with a 100 nm layer of silica to reflect positronium atoms. At Saclay, the laser will not be available, hence the previous mentioned constraints are not applicable. Therefore, the mirror and glass plates forming the top and bottom of the cavity could be replaced by two mesoporous silica targets, which could increase the positronium density.

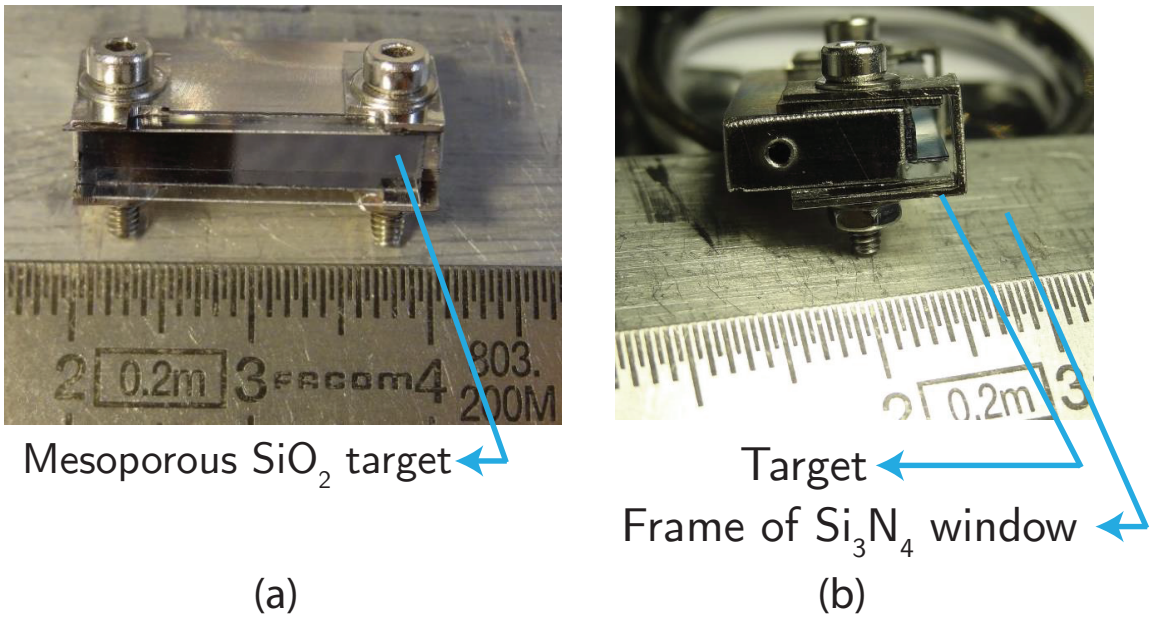

Figure 6.4: Pictures of the reaction cavity. (a) Front view: the mesoporous target is coating the back wall of the cavity. (b) Side view: the frame of the Si_3N_4 is visible.

Positronium emission from a porous material

The mesoporous SiO_2 target is responsible for the conversion of positrons into positronium atoms. It is therefore an essential part of the ANTION experiment.

Paulin and Ambrosino [101] first reported the observation of a long mean life, close to 142 ns, in the positron annihilation spectra of some powders such as SiO_2. It has also been shown that the implantation of keV positrons in silica containing a network of interconnected pores results in the emission of ortho-positronium.

When positrons with kiloelectronvolt energy are implanted in a material, they undergo different processes that include the formation of positronium. Since this subject is discussed in more detail in Chapter 7, only the positronium formation will be described here. According to the spur reaction model [102], upon implantation the positron thermalization results in an electron spur and corresponding positive ions. Mogensen in reference [102] defines spur as "group of reactive intermediates which are so close together that there is a significant probability of their reacting with each other before diffusing into the bulk medium". Positronium atoms can form by the combination of the positron with a spur electron. This reaction competes with the recombination of the electrons and the positive ions, and with the diffusion of electrons. In a porous material in which the pores are interconnected, the ortho-positronium is able to diffuse through the pores, reaching the material surface where it is emitted into the vacuum. The fraction of positronium atoms that are emitted from a porous film depends on the positron implantation depth and the structure of the pores in the material (size, interconnectivity, etc.). Before being emitted, the positronium atoms are able to cool to near thermal temperatures by interacting with the surface of the pores. The kinetic energy with which they are emitted is limited by the pore size, due to quantum mechanical confinement in the pores [103, 104].

In the pores, ortho-positronium can annihilate with an electron with an opposite spin and emit two γ-ray photons. This decay channel is denominated pick-off annihilation and contributes to the intrinsic decay of the ortho-positronium in vacuum, resulting in an increase in the effective decay rate.

The mesoporous film employed in this experiment is prepared via the sol-gel process described in [105, 106] and corresponds to the F sample studied in these references. It has been shown to emit positronium with a yield of $\sim$30% and 48 ± 5 meV energy [103].

Figure 6.5 shows two pictures of the SiO_2 mesoporous film in which the pore structure can be observed. These pictures were obtained with a scanning electron microscope (SEM).

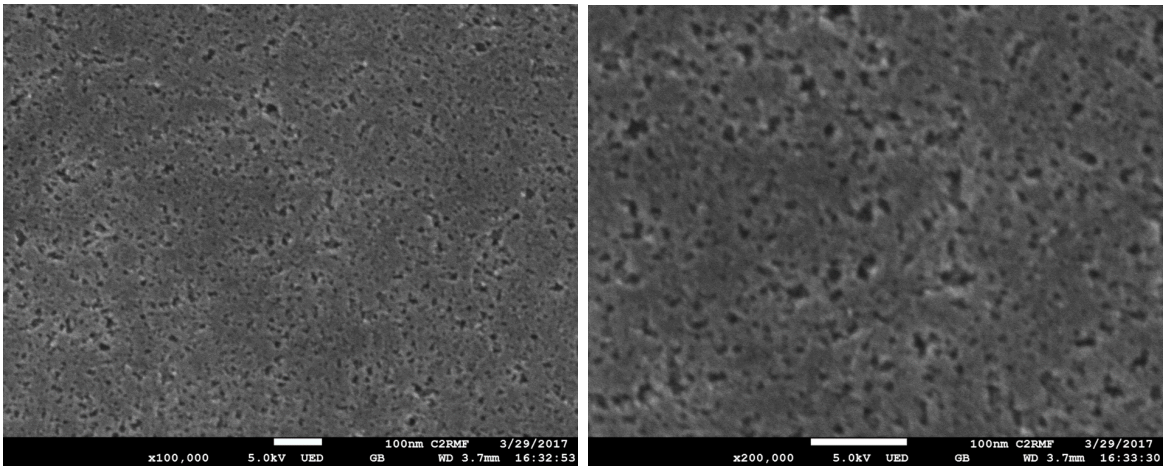

(a) (b)

Figure 6.5: Pictures of the SiO_2 mesoporous film obtained with a scanning electron microscope (SEM). The white bar represents the scale corresponding to 100 nm. The pore structure of the film can be observed. (a) 100 000 magnification (b) 200 000 magnification. Copyright C2RMF, P. Lehuédé.

6.1.2 Detection and diagnostics

The proton current will be measured with a Faraday cup. During the tuning of the beam focusing, its profile will be imaged with the aid of a phosphor screen in combination with a CCD camera.

The positronium annihilation signal will be monitored by a lead tungstate ($PbWO_4$) crystal detector optically coupled to a R329-02 Hamamatsu Photonics photomultiplier tube, which amplifies the scintillation signal. Its high density, $8.28\,g/cm^3$, and fast decay time of 6 ns makes it a fast response (~ 10 ns time resolution) and a good energy resolution detector [107], while the low light yield of $200\,\gamma$ per MeV is compensated by the photomultiplier. The crystal combined with the photomultiplier has a total efficiency of $\sim 80\%$. Photomultiplier tubes are sensitive to magnetic fields, hence the tube is covered by mu-metal. The photomultiplier signal is recorded by an oscilloscope with 500 MHz bandwidth and 2.5 GS/s. In order to place the detector as close as possible to the cavity, the detector was inserted into a cylindrical hollow flange that

extends into the center of the reaction chamber. The distance between the cavity and the detector is 10 cm.

The hydrogen atoms and ions with keV kinetic energy will be detected by a 2 layer *Photonis* MCP with 40 mm diameter, a gain of 10^7 and a maximum of 0.4 dark counts per second per cm^2, combined with a phosphor screen. It has been shown that the this type of detectors can detect hydrogen ions and atoms at keV energy, though the detection efficiency is strongly dependent on the particle's energy [108]. A low noise CCD camera, PCO.Pixelfly, will capture the photons emitted by the phosphor screen. Positive particles incident on the MCP will be rejected by a high transparency grid in front of the MCP held at positive voltage (1 kV). The negative particles (which are accelerated by the grid) will be rejected by the $\sim$-2 kV voltage applied to the front side of the MCP. To reduce the dark noise, the camera exposure time will be of the order of a few microseconds.

6.2 Simulation description

The simulations described in this chapter were performed using the GEANT4 toolkit [41], which simulates the interactions of particles in matter using the Monte Carlo method. The advantage of GEANT4 is that it incorporates the geometry and the materials of the experimental apparatus and detector, as well as the interaction models and differential cross sections of the simulated particles.

GEANT4 was originally developed for high energy physics, but nowadays low energy physics packages are also available. The PENELOPE (PENetration and Energy LOss of Positrons and Electrons) library includes low energy (few hundred eV to about 1 GeV) physics processes such as Compton scattering, photoelectric effect, e^--e^+ pair creation, bremsstrahlung, ionization and positron annihilation [109]. However, the GEANT4 package does not include the positronium atom and its associated physics. Hence, new physics libraries, based on previous work by Crivelli and Gendotti [110], were written to simulate the behavior of ortho-positronium and para-positronium production, including their annihilation and reflection on surface walls. Electric and magnetic fields were not considered since the first should not influence the behavior of the positronium atoms, and the latter should be very small at the location of the chamber.

6.2.1 Positron beam

The simulation was conceived at a time in which the positron beam parameters were not well defined. As such, the positron beam was assumed to be monoenergetic with energy 4 keV. In the simulation, the production of ortho-positronium is not dependent on the positron energy distribution, since the positron implantation in the SiO_2 and the positronium formation are not simulated. As a first approach, and for simplicity, a Gaussian time distribution was used, as well as a Gaussian spatial distribution with $\sigma_x = 1$ mm and $\sigma_y = 3$ mm (see figure 6.6) The spatial distribution was suggested by simulations of the positron focusing lenses. However, when these quantities are known experimentally, one can easily change them and redo the simulations. One million positrons were simulated.

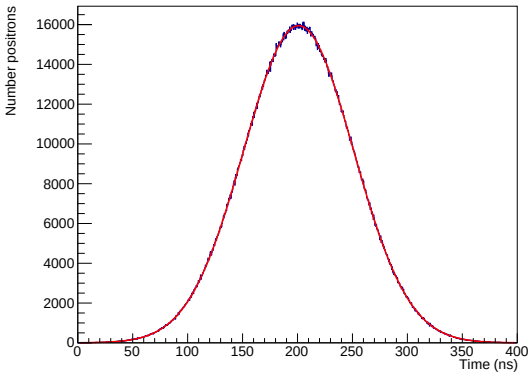

(a)

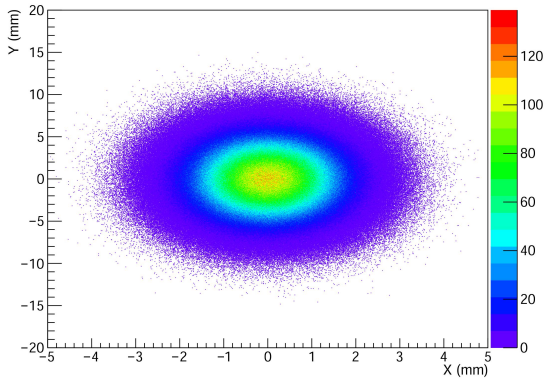

(b)

Figure 6.6: Generated positron beam with a Gaussian time distribution (a) and a Gaussian spatial distribution with $\sigma_x = 1\,\text{mm}$ and $\sigma_y = 3\,\text{mm}$ (b).

6.2.2 Positronium formation

In the simulation, it was considered that the fraction of ortho-positronium emitted into vacuum is 30%, in agreement with experimental observations [106]. When the positron beam hits the mesoporous silica target several processes can occur with different probabilities:

1. e^+-e^- annihilation (50% fraction).

2. e^+ backscattering (10% fraction [111]) - the original e^+ is eliminated and a e^+ with flat energy distribution between 10 and 100 eV is emitted isotropically.

3. ortho-positronium production (30% fraction) - an ortho-positronium atom is emitted to the vacuum with an isotropic or cosine angular distribution, and a Maxwel-Boltzman energy distribution with $\langle E \rangle = 50\,\text{meV}$ (see figure 6.7).

4. para-positronium production (10% fraction) - the para-positronium atom is not defined in the simulation, but two γ-ray photons with 511 keV energy are emitted back-to-back.

For simplicity, the pickoff process was not considered as its contribution to the background is assumed to be very small, though it can be easily implemented.

The physics of the positronium formation in a porous material was not implemented in this simulation as it is a complex process and, thus, difficult to simulate. Moreover, the underlying physics is not well known, thus a choice was made to rely on experimentally measured parameters. The positronium atom is created at the surface in the same position where the positron hit the target surface. The angular distribution of the ortho-positronium emitted from the silica surface as well as after being reflected in the cavity's walls is not well known. Therefore, in this simulation an isotropic or cosine distribution was implemented.

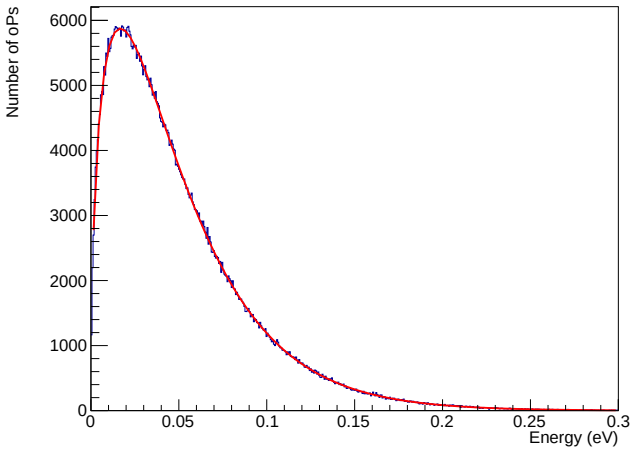

Figure 6.7: The ortho-positronium atoms are emitted with a Maxwell-Boltzmann energy distribution with mean longitudinal kinetic energy of $\langle E \rangle = 50\,\text{meV}$.

6.2.3 Positronium annihilation

Para-positronium

The para-positronium atom does not actually exist in the simulation. Instead, a simplification was made in which when a para-positronium is formed, two photons with 511 keV energy are emitted back-to-back, while taking into account the para-positronium lifetime (125 ps). The photons are emitted with an isotropic angular distribution.

Ortho-positronium

The ortho-positronium decay process was generated taking into account the decay matrix element, M_{if} [112]

$$\frac{1}{4}\sum_{polarization}|M_{if}| = 16\times(4\pi)^3 e^6\left[\left(\frac{m_e-\omega_1}{\omega_2\,\omega_3}\right)^2+\left(\frac{m_e-\omega_2}{\omega_1\,\omega_3}\right)^2+\left(\frac{m_e-\omega_3}{\omega_1\,\omega_2}\right)^2\right], \quad (6.1)$$

where ω_1, ω_2 and ω_3 are the frequencies of the three γ-ray photons, e and m_e are the electron charge and mass, respectively, with the convention $\hbar = c = 1$. The spectral distribution of the decay photons can be derived by integrating the differential cross section for the three-photon annihilation over $d\omega_3$ and $d\omega_2$,

$$d\bar{\sigma}_{3\gamma} = \frac{8e^6}{3vm^3} F(\omega_1)\, d\omega_1\,, \tag{6.2}$$

$$F(\omega_1) = \frac{\omega_1(m-\omega_1)}{(2m-\omega_1)^2} + \frac{2m-\omega_1}{\omega_1} + \left[\frac{2m(m-\omega_1)}{\omega_1^2} - \frac{2m(m-\omega_1)^2}{(2m-\omega_1)^3}\right] \ln\left(\frac{m-\omega_1}{m}\right). \tag{6.3}$$

The energy distribution of the simulated γ-ray photons resulting from the annihilation of ortho-positronium in vacuum can be observed in figure 6.8. The energy spectrum is continuous with an end point at 511 keV.

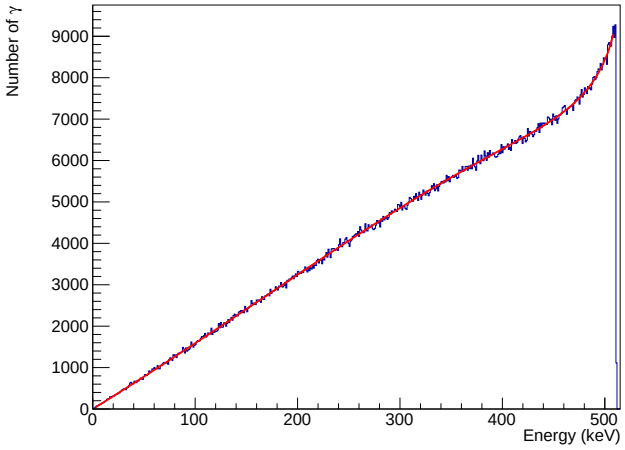

Figure 6.8: Energy distribution of simulated γ-ray photons resulting from the annihilation of ortho-positronium in vacuum.

The time distribution of the ortho-positronium decay can be observed in figure 6.9. An exponentially modified Gaussian fit yielded $\sigma_t = 50.0 \pm 0.2$ ns and $\tau = 141.2 \pm 0.3$ ns. The time spread corresponds to the time spread of the positron beam ($\sigma_t = 50$ ns in figure 6.6a) and the lifetime, τ, agrees with the ortho-positronium lifetime.

Implemented geometry

The geometry of the ANTION apparatus was included in the simulation with as much detail as possible, namely the stainless steel reaction chamber and respective flanges, the last focusing electrode before the reaction cavity and the lead tungstate detector. Particular attention was given to the geometry of the reaction cavity and to the distance between this and the detector. The cavity is composed of silica plates on top and

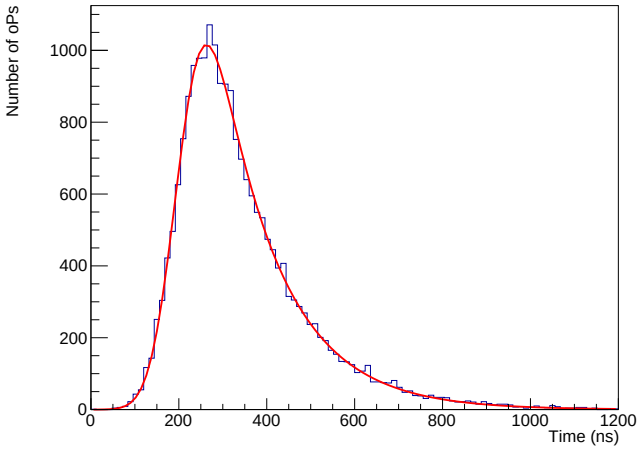

Figure 6.9: Simulated time distribution of ortho-positronium decay (—). The histogram was fitted to an exponentially modified Gaussian (—) yielding $\sigma_t = 50.0 \pm 0.2$ ns and $\tau = 141.4 \pm 0.4$ ns.

bottom, a mesoporous target on the back and a Si_3N_4 window. The implementation of a detailed geometry has the goal of rendering the simulation as realistic as possible, in order to account for the Compton scattering that may contribute to the background, as well as the effect of the cavity geometry on the positronium density.

Figure 6.10 shows the geometry of the ANTION apparatus implemented in the GEANT4 simulation. The spherical part of the chamber was removed to uncover the instruments located inside. The vacuum flanges of the reaction chamber are shown, as well as the last focusing electrode and the cavity holder. The detector is shown in purple and is inserted inside a flange (removed from the picture). A few particle tracks are visible: one positron arriving from the left is implanted on the mesoporous target, leading to the production of one ortho-positronium atom that undergoes a few reflections inside the cavity before decaying into three γ-ray photons.

Si_3N_4 window transparency

According to the simulation, 98% of the positrons with 4 keV energy are able to go through the 30 nm thick Si_3N_4 window. This result is consistent with Monte Carlo simulations performed by O'Rourke *et al.* in reference [113]. For 4 keV positrons they estimate an angle of peak positron emission of 13 to 14°. This angle is of interest because it influences the amount of positrons that imping on the mesoporous target instead of the silica walls. It could be, in principle, tested by letting a positron pulse through the window and measure the beam profile with a microchannel plate detector. The profile can then be compared to the original beam profile. Cooke *et al.* [114] measured the energy loss spectrum of positrons transmitted through a 30 nm thick Si_3N_4 window and reported that for an impact energy larger than 2 keV, the energy loss was around 100 eV to 200 eV.

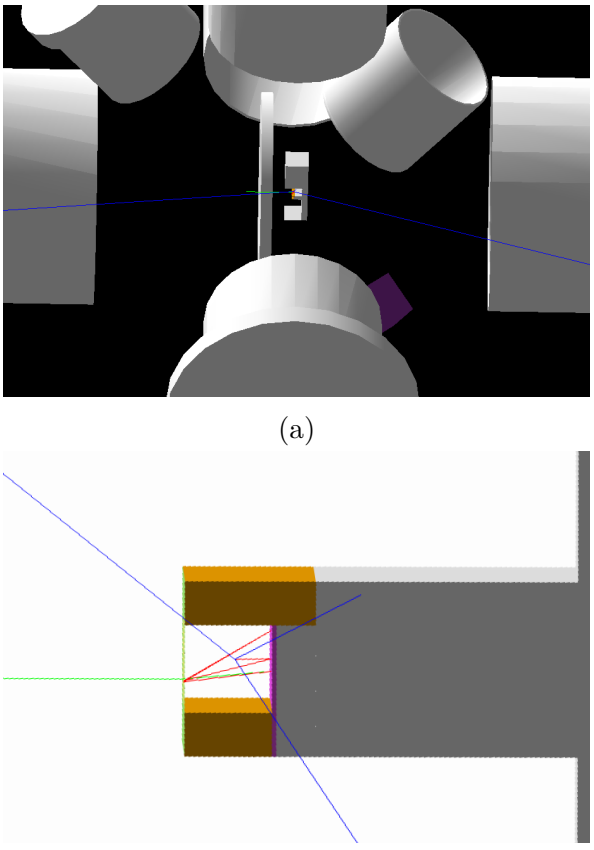

(a)

(b)

Figure 6.10: The geometry of the ANTION apparatus was implemented in GEANT4. (a) The vacuum flanges of the reaction chamber are shown, as well as the last focusing electrode and the cavity holder. The detector is shown in purple. The flange in which the detector is inserted was removed from this picture. (b) Detail of the cavity in which the reaction takes place. A few particle tracks are visible: one positron (green) arriving from the left is implanted on the mesoporous target (magenta), leading to the production of one ortho-positronium atom (red), which undergoes a few reflections inside the cavity before decaying into three γ-ray photons.

Simulation

A simulation starts by shooting the positron beam at the cavity. Most positrons propagate through the thin silicon nitride window and enter the cavity at an angle. Those that enter the cavity hit the walls and can either form positronium atoms, undergo backscattering or annihilate. The γ-ray photons resulting from the annihilation of the positrons or positronium can undergo several Compton scatterings before being detected by the lead tungstate scintillation detector. GEANT4 allows the tracking of each particle created during the simulation, and registers the deposited energy of the γ-ray in the detector. It is also able to distinguish the origin of each detected γ-ray, thus it is possible to distinguish the γ-ray photons resulting from each type of annihilation, and to know whether they underwent Compton scattering before being detected.

Parameters

The simulation parameters include the positron beam time and spatial distribution, the number of positrons and the cavity geometry. For the simulations described in this chapter, the cavity dimensions were fixed to 2 mm×2 mm×20 mm because it is the one foreseen for the measurements at Saclay. However, this geometry can and should be modified for the CERN measurements. First, because a more dense positronium cloud is required, and second because the laser will be employed, thus the cavity will have a mirror on the bottom.

For the Saclay measurements, there is a possibility of covering the top and bottom walls of the cavity with mesoporous film. Thus, the coating of the cavity is also a parameter that needs to be studied.

6.3 Results of the simulation

6.3.1 Hydrogen production

The first step of the ANTION project is to measure the hydrogen production cross section, at Saclay. It is therefore interesting to estimate the number of atoms one can produce given the physical characteristics of the positron and proton beam, as well as the evolution of the ortho-positronium density in the cavity.

A positron beam with 10^6 positrons incident on the reaction cavity was simulated. The proton beam was considered to have a current of 1 μA. The time distribution of the ortho-positronium density was evaluated by counting the number of ortho-positroniun atoms inside the cavity for each time step of 10 ns. Due to the absence of experimental input, a few assumptions were made in this calculation. The positron beam was assumed to have a Gaussian distribution with a mean of $\bar{t}_{t,e^+} = 200$ ns and a time spread of $\sigma_{t,e^+} = 10$ ns. This value is consistent with the expected time distribution once the positron beam is bunched.

Figure 6.11a shows the ortho-positronium density inside the cavity as a function of time. The simulation results were extrapolated to 10^8 e^+. It was also assumed that the proton beam was not well focused and that it had an homogeneous spatial distribution of 2 mm by 2 mm, corresponding to the section of the cavity. This assumption is realistic for the experiments at Saclay. The proton beam was assumed to be monoenergetic and its time distribution was taken as a Gaussian of $\sigma_{t,\mathrm{p}} = 100$ ns and its mean, $\bar{t}_{\mathrm{p}}$, coincides with the maximum of the positronium density distribution (220 ns). Even though this assumption increases the probability of proton-positronium collision, it is not unrealistic as in principle one could optimize the trigger delay between the positron and the proton beams. The proton beam contains a total number of protons of $\sim 10^7$. The time distribution of the proton beam is showed in figure 6.11b. It was also assumed that the protons only interact with the ortho-positronium atoms inside the cavity.

The number of hydrogen atoms produced per positron pulse was estimated according to the equation

$$N_{\mathrm{H}} = \int_{t_0}^{t} n_{\mathrm{oPs}}(t) N_{\mathrm{p}}(t)\, v_{\mathrm{p}}\, \sigma\left(oPs_{1\mathrm{s}}, H_{n_h,l_h}\right)\, dt\,, \tag{6.4}$$

where $n_{\mathrm{oPs}}(t)$ corresponds to the ortho-positronium density distribution with time (plotted in figure 6.11a), $N_{\mathrm{p}}(t)$ is the proton time distribution (plotted in figure 6.11b), v_{p} is the proton velocity and $\sigma\left(oPs_{1\mathrm{s}}, H_{n_h,l_h}\right)$ is the cross section for the production of hydrogen (up to H($4f$)) for a given proton impact energy.

Figure 6.11c shows the cross sections computed using the Coulomb-Born Approximation (CBA) [36] and the two-center convergent close-coupling (CCC) method [39]. The estimated number of hydrogen atoms produced per positron pulse as a function of the proton beam impact energy is presented in figure 6.11d. For the CBA method, the maximum number of hydrogen atoms produced per positron pulse is 2.7 for a proton impact energy of $\sim 6\,\mathrm{keV}$, while according to the CCC method, a maximum of 1.6 hydrogen atoms could be produced for a proton impact energy of $\sim 10\,\mathrm{keV}$.

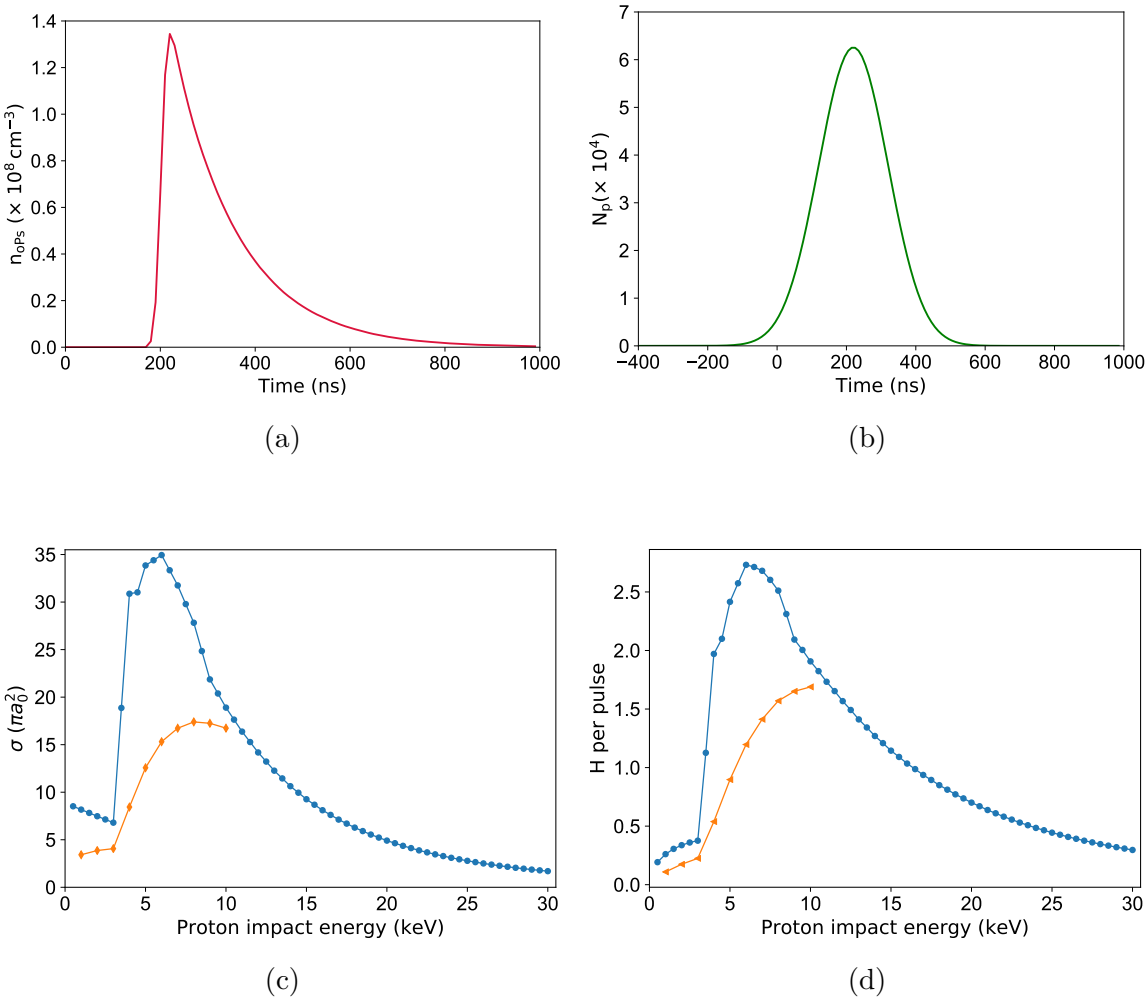

Figure 6.11: (a) Ortho-positronium density distribution with time inside the cavity. (b) Proton beam time distribution.(c) Cross section of hydrogen production according to the CBA method (—) (sum from H($1s$) to H($4f$)) and (—) CCC method. (d) Number of hydrogen atoms produced per pulse for the cross sections showed in (c).

6.3.2 Ortho-positronium density distribution in the cavity

The positronium excitation $3d$ laser will not be used in the experiments performed at Saclay, thus it is possible to have the top and the bottom walls of the cavity coated with a mesoporous silica film. This can in principle increase the positronium density as the positrons that enter the cavity with an angular spread may contribute to the positronium production, if they are implanted in the top or bottom plates forming the cavity. Indeed, with the three walls of the cavity coated with the mesoporous film, 19% of the positrons form ortho-positronium, while for the original setup with plain silica on top and bottom of the cavity, only 11% of the positrons composing the positron beam are able to produce ortho-positronium.

According to the simulations, the number of ortho-positronium confined inside the cavity is 57% larger if all the walls are coated with mesoporous silica, than with two walls coated with normal silica. This is an important finding as it indicates that for proton impact energies higher than 6 keV it might be more advantageous to coat the entire cavity with mesoporous film. However, further study is required to understand the low production rate in the case of the silica coated walls.

6.3.3 Angular distribution

The angular distribution of the emission of positronium from the mesoporous target surface is not well known, as well as the angular distribution of the reflected positronium atoms in the cavity's walls. An isotropic angular distribution should imply that a larger fraction of ortho-positronium atoms are able to escape the cavity. For that reason simulations were made to evaluate the impact of the positronium angular distribution on the positronium density, by comparing the fraction of ortho-positronium that decays inside the cavity for isotropic and cosine distributions.

Table 6.1 shows a comparison of the percentage of ortho-positronium atoms that decay inside the cavity for isotropic and cosine angular distribution, as well as mesoporous film covering the top and bottom of the cavity versus glass. In the simulations in which the positronium atoms are emitted with an isotropic angular distribution, the reflection in the cavity walls was also assumed to be isotropic. The same is true for the cosine distribution simulations. Indeed, an isotropic angular distribution leads to a higher fraction of positronium that escape the cavity (11% versus 3% for cosine distribution), however since the cavity is very long this effect is small. Yet, a smaller cavity with 10 mm length will be used for the CERN measurements, which will lead to an increase in the fraction of ortho-positronium atoms that are able to escape.

An indirect way of estimating the fraction, and perhaps the angular distribution, would be to use a smaller cavity, e.g. 10 mm long, which would lead to an increase of the number of positrons able to escape the cavity (27% for isotropic angular distribution and 11% for cosine angular distribution). One could envision the insertion of one tungsten block between the cavity and the detector, in order to block the annihilation signal originated from the ortho-positronium decay inside the cavity. By comparing the decay signal with and without the tungsten block, one could in principle infer the angular distribution of the emitted positronium from the amount of ortho-positronium that decayed outside the cavity. A similar idea has been implemented by Khaw *et*

Table 6.1: Comparison of the percentage of ortho-positronium atoms that decay inside the cavity for isotropic and cosine angular distribution, as well as mesoporous film coating the top and bottom of the cavity versus glass.

Angular distribution	Mesoporous SiO_2	Glass
Isotropic	89%	89%
Cosine	97%	97%

al. [115] in determining the reflection process of muonium atoms, inside two SiO_2 confining surfaces. Their results indicate that the reflection process is well described by a cosine angular distribution.

Figure 6.12 shows two view planes (side and top view) of the spatial distribution of the ortho-positronium annihilation point, in the case of isotropic and cosine angular distribution, with mesoporous film coating the top and bottom of the cavity. One can observe that for the cosine distribution (figures 6.12a and 6.12c) the positronium atoms are distributed in the cavity more uniformly than for the isotropic distribution (figures 6.12b and 6.12d). In the latter case, figure 6.12b shows a larger concentration of atoms in the corners of the cavity, while in the center the concentration is smaller than for the cosine distribution. Figure 6.12d shows a larger number of positronium atoms outside the cavity, as expected for the isotropic distribution.

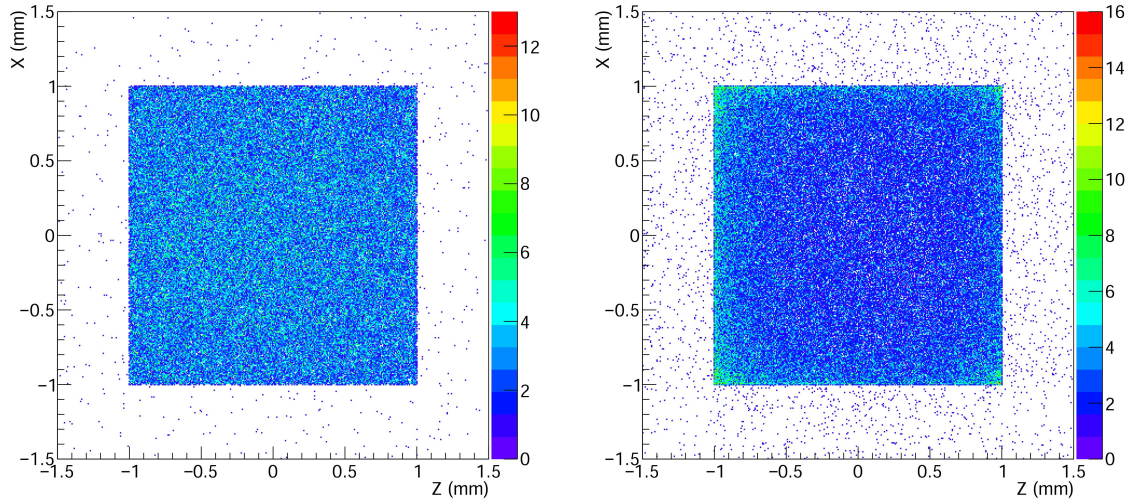

(a)

(b)

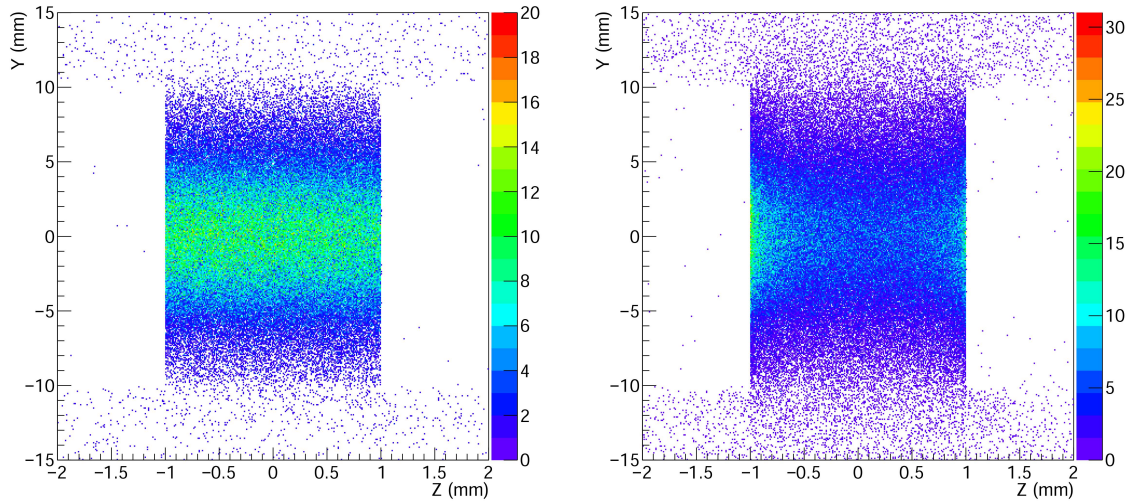

(c)

(d)

Figure 6.12: Spatial distribution of the ortho-positronium annihilation point. The mesoporous film was coating the top and the bottom of the cavity. (a) Side view, xz-plane. Cosine angular distribution. (b) Side view, xz-plane. Isotropic angular distribution. (c) Top view, yz-plane. Cosine angular distribution. (d) Top view, yz-plane. Isotropic angular distribution. The positron pulse enters the cavity from the right side.

6.4 Background estimation

This section is dedicated to the study of the background signal that contaminates the positronium annihilation signal measured by the lead tungstate detector. The simulated cavity geometry is 2 mm×2 mm×20 mm with glass on top and bottom.

The ortho-positronium decay in vacuum produces predominantly three annihilation γ-ray photons with a broad energy distribution (0-511 keV), as opposed to the two 511 keV γ-ray decay in the case of e^+ and para-positronium . Moreover, there is a dependence of the detector acceptance on the number of photons produced in the two types of decays. This is due to the fact that the solid angle covered by the detector is smaller than 4π, thus the probability to detect one photon in a 3γ decay is larger than in a 2γ decay. In addition, the different γ-ray energy of the two decay types result in different contributions of the Compton scattering of the photons with the materials such as the vacuum chamber, the focusing electrodes, the light shielding around the detector and the detector itself. As both the number of γ-rays emitted in an annihilation event and their energy distribution are different, the detection efficiency of the 3γ decay is different from that of the 2γ events.

The γ-ray photons produced by the annihilation of positrons with electrons, of para-positronium and ortho-positronium was simulated. The positron beam was assumed to have a Gaussian distribution with a time spread of $\sigma_{t,e^+} = 10$ ns and a mean of $\bar{t}_e^+ = 200$ ns, shown in figure 6.11a. Figure 6.13a shows the deposited energy in the detector as a function of time, while in figure 6.13b one can distinguish the annihilation background contribution to the signal (without the Compton scattering background) from the ortho-positronium decay signal. The deposited energy in the detector was computed by multiplying the number of events, detected by the lead tungstate detector, by the mean energy deposited in the detector by 3 γ-ray photons ($\sim$ 306 keV) and 2 γ-ray photons ($\sim$ 411 keV). The γ-ray photons from Compton scattering from the reaction chamber and focusing electrode were excluded.

Figure 6.15 shows a histogram (in black) of the deposited energy spectrum including the Compton scattered γ-ray photons. The blue curve corresponds to the deposited energy but the γ-rays that underwent Compton scattering with the reaction chamber and focusing electrode were rejected. Finally, the red curve shows only the deposited energy of the γ-ray photons that underwent Compton scattering with the chamber and focusing electrode. The two γ-ray photon decay is responsible for the peak at 511 keV, while the γ-rays that undergo Compton scattering deposit energy from 0 to the Compton edge at 341 keV. Figure 6.16 shows the energy deposited in the detector by the γ-ray photons originated from the 3γ decay.

While the energy deposited rejecting the Compton scattering with the chamber and the focusing electrode is realistic because the geometry of the target and target holder is accurate, the fraction of Compton scattered γ-ray photons with the chamber is less reliable since there are many elements missing from this geometry. As a consequence, the shape of the distribution is realistic but the fraction is underestimated.

To estimate the Compton fraction, a low intensity positron annihilation signal (one γ-ray is detected per trigger) will be measured by the lead tungstate detector, in the same experimental apparatus, so that the Compton signal can be distinguished by the

energy deposited in the detector.

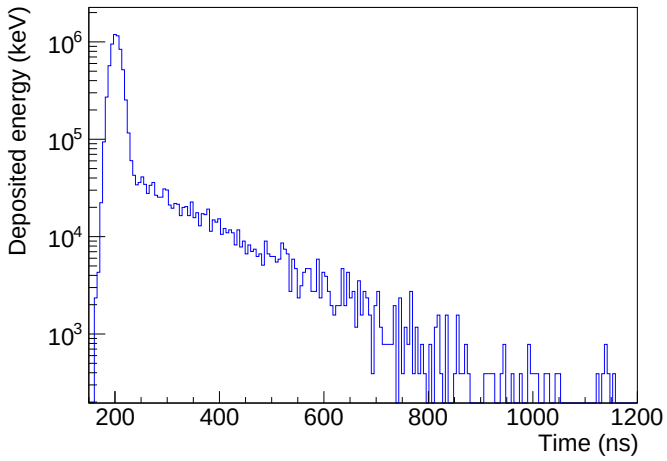

(a)

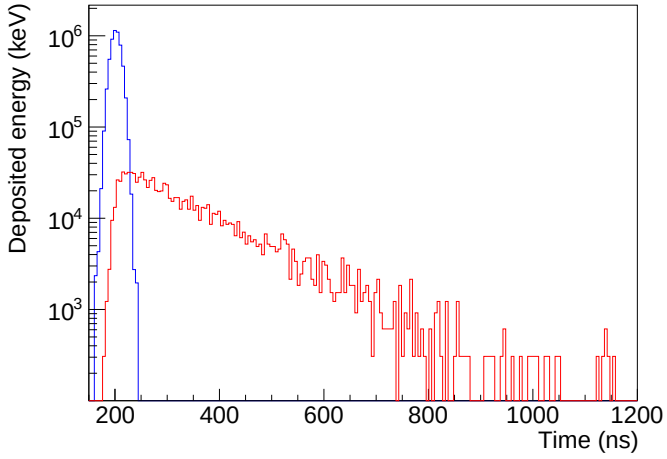

(b)

Figure 6.13: Simulated deposited energy in the detector as a function of time. (a) Total deposited energy as a function of time. (b) Background (—) and ortho-positronium (—) deposited energy as a function of time.

Figure 6.14 shows the simulated deposited energy in the detector as a function of time for the γ-ray photons generated by the annihilation of the positrons with electrons and the annihilation of para-positronium atoms. As expected the shape of the curve conserves the Gaussian profile of the incident positron beam with $\sigma = 10\,\text{ns}$.

From the measurement of the ortho-positronium annihilation with the lead tungstate detector, one can estimate the number of ortho-positronium atoms formed upon the impact of the positron pulse with the target.

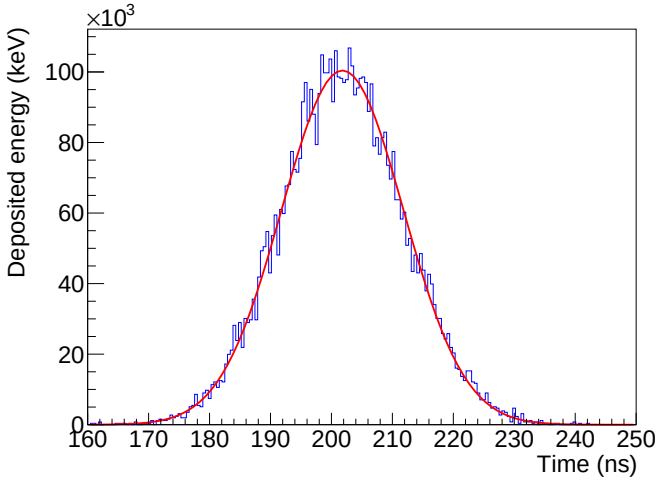

Figure 6.14: Simulated deposited energy in the detector as a function of time for the annihilation background signal. The Gaussian fit yielded $\bar{t} = 201.8\,\text{ns}$ and $\sigma_t = 10\,\text{ns}$.

The total number of ortho-positronium atoms produced is related to the annihilation signal by

$$\text{Number of oPs} = E_{\text{dep}_{\text{measured}}}(t > 250\,ns) \times \frac{E_{\text{dep}_{\text{oPs}}}}{E_{\text{dep}}(t > 250\,ns)} \times \frac{1}{\varepsilon} \times (1 - f_{\text{Compton}})\ . \tag{6.5}$$

where $E_{\text{dep}_{\text{measured}}}(t > 250\,ns)$ is the integral of the signal measured by the detector, in which the values t<250 ns were excluded. This exclusion corresponds to 5 σ_t of the incident positron beam. The selection of the integration region aims to minimize the background component of the signal. $E_{\text{dep}_{\text{oPs}}}$ corresponds to the integral of the deposited energy by the γ-ray photons originated from the decay of ortho-positronium (red curve in figure 6.13b). $E_{\text{dep}}(t > 250\,ns)$ is the integral of the tail of the total deposited energy (figure 6.13a), including γ-ray photons originated from the decay of positrons, para-positronium and ortho-positronium. The integration region is the same as the one used to compute $E_{\text{dep}_{\text{measured}}}(t > 250\,ns)$. f_{Compton} is a correction due to the γ-ray photons that undergo Compton scattering. This correction should be obtained experimentally, as was discussed previously. Finally, ε corresponds to the total detection efficiency.

The total detection efficiency includes the detector efficiency ($\varepsilon_{\text{eff}} = 83 \pm 4\%$ for 511 keV photons, measured experimentally) and acceptance ($\varepsilon_a = 2.7$ % obtained from the simulation)

$$\varepsilon = \varepsilon_{\text{eff}} \times \varepsilon_a \ \sim\ 2\%\,. \tag{6.6}$$

From the simulation it is possible to estimate the fraction

$$\frac{E_{\text{dep}_{\text{oPs}}}}{E_{\text{dep}}(t > 250\,ns)} = 2.3\,. \tag{6.7}$$

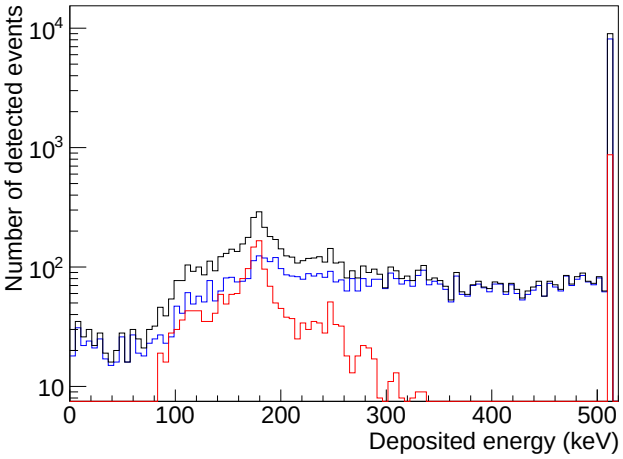

Figure 6.15: Deposited energy spectrum including Compton scattering (—). Same but rejecting Compton scattering with the chamber and the focusing electrode (—). Only Compton scattering with the chamber and the focusing electrode (—). The events corresponding to when no energy was deposited in the detector were subtracted from the first bin.

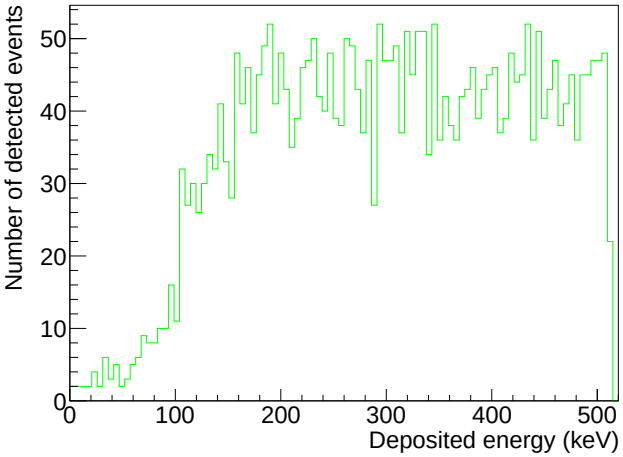

Figure 6.16: Deposited energy spectrum of γ-ray photons resulting from the annihilation of ortho-positronium. Compton scattering is not included.

6.5 Conclusion and outlook

The simulations described in this chapter had the purpose of estimating the positronium density in the cavity as well as the background associated with the positron and para-positronium decay, in order to assist with the cross section measurement of hydrogen.

Using the values of the hydrogen production cross section as a function of the proton impact energy, it was possible to estimate the number of hydrogen atoms produced, giving 2.7 hydrogen atoms for a proton impact energy of $\sim 6\,\text{keV}$ according to the CBA model and 1.6 hydrogen atoms for a proton impact energy of $\sim 10\,\text{keV}$ according to the CCC, for a pulse with 10^8 positrons. This study should be repeated once the physical parameters of the positron and proton beam are better known, so that a more realistic estimation can be done.

The simulations indicate that for the measurements performed without the excitation of the ortho-positronium atoms, if the top and bottom of the cavity are coated with a mesoporous film then the number of ortho-positronium atoms confined inside the cavity can be increased by as much as 57%.

There is a large parameter space whose study could be of interest in order to increase the production rate of hydrogen. This includes the optimization of the cavity geometry, the delay between the positron beam and the proton beam, the time distribution of the positron and proton beam, as well as their spatial distributions. The study and optimization of these parameters should be conducted when the positron and proton beam parameters are known.

It would be useful if Comini's simulation [116] would be incorporated into this GEANT4 simulation, in order to include the excitation of the positronium atoms. This would involve the introduction of the interaction between the ortho-positronium atoms and the excitation laser. This task is complex since it would imply the creation of routines that include the optical Bloch equations that describe the evolution of the positronium excited states population. It would also be interesting to simulate the interaction of the proton beam with the positronium atoms, including the hydrogen and hydrogen ion production cross sections. Obviously, an equivalent study must be conducted for antiprotons, with the antihydrogen and antihydrogen ion cross sections. In the latter case, the study of the antiproton annihilation background would be highly important.

Part IV

reDiscovery of a positron moderator

7 Study of a positron moderator

"Extraordinary claims require extraordinary evidence."
Carl Sagan

Contents

In this chapter, a description is given of the studies conducted to determine the moderation efficiency, the positron work function, the moderated positron energy distribution and the diffusion length of a commercially available epitaxial layer of silicon carbide. This study can be of interest to slow positron physics experiments by improving the brightness of positron beams, and in particular to GBAR, by potentially increasing the number of trapped positrons in an accumulator. The chapter concludes with two possible applications of this moderator.

Before describing the experiments and results, a brief introduction to the physics of positron moderation is provided.

7.1 Positron moderation

Monoenergetic positron beams are used in several fields such as atomic physics, condensed matter physics, material sciences and plasma physics (see [117] for a comprehensive review of the subject). These beams can originate from radioactive or pair creation source. The resulting positrons have a wide energy distribution up to a few MeV and are moderated to a few eV by either a negative work function material for positrons or a solid rare gas. Annealed tungsten is commonly used as a positron moderator due to its high density, easy handling and its relatively low cost. For this moderator, typical moderation efficiencies are of the order of 10^{-3} [118]. Nonetheless, higher moderation efficiencies can be obtained by condensing a solid rare gas on the radioactive source capsule. Wu *et al.* [119] reported a moderation efficiency as high as 1% for a solid neon moderator. While tungsten requires careful annealing to high temperatures, solid rare gas moderators demand good growth conditions under low pressure conditions and a cryostat, and regular regrowth is necessary. Moreover, the energy distribution of the positrons moderated by solid neon is not as narrow as metallic moderators, due to incomplete positron thermalization.

Incident keV positrons on a solid surface can undergo different interactions with matter as summarized in figure 7.1. Upon impact the positrons can backscatter into the vacuum (1), capture an electron and form positronium (2), or (3) produce secondary electrons. Implanted positrons thermalize before undergoing diffusion through the solid until they either annihilate in a delocalized (free) state (4), become trapped in a defect (5) or diffuse to the surface where they can be emitted into the vacuum, if the material has a negative work function for positrons (6).

The work function, Φ^+, is defined as the minimum energy necessary to remove a positron from the bulk of a material to the vacuum [120],

$$\Phi^+ = -\mu^+ - \Delta\,, \tag{7.1}$$

where μ^+ is the positron chemical potential of the material and Δ represents the surface dipole barrier caused by the tail of the electron distribution into the vacuum. Δ is negative for positrons and is responsible for small or even negative Φ^+. The positron chemical potential includes the repulsion from ion cores and the attraction to the electrons. In negative work function materials, incident keV positrons that reach the surface after diffusion, are re-emitted into the vacuum with a kinetic energy corresponding to the thermally spread work function [121].

Upon implantation in solid, the positrons thermalize in less than 10 ps. In metals, the energy loss is due to electronic ionization and excitation, while in a semiconductor, such as silicon carbide, the thermalization mechanism is akin to metals except in the low energy regime. The existing band gap prevents the electron-hole excitation or ionization (proportional to the band gap), if the positron energy is smaller than the band gap energy. At this stage phonon scattering is the only thermalization mechanism at play. This mechanism is ineffective as the phonon energies are small, hence a fraction of epithermal (non-thermal) positrons can be expected. This phenomenon is responsible for the epithermal positrons observed in solid neon.

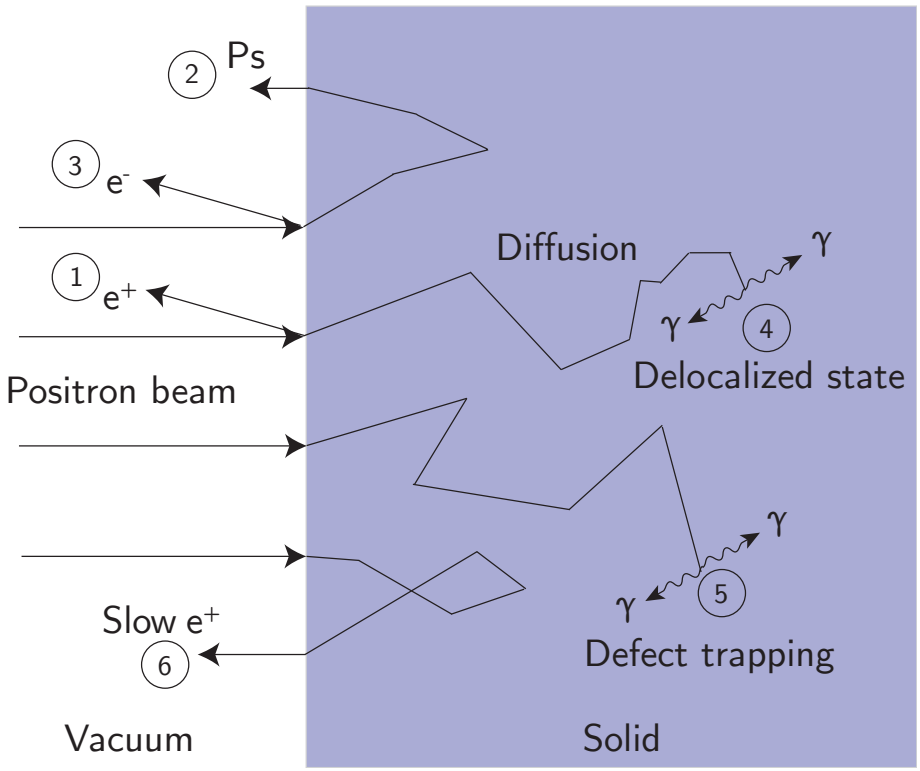

Figure 7.1: Schematic diagram of some of the processes that occur when positrons interact with matter. Upon impact the positrons can be backscattered (1), form positronium (2) or produce secondary electrons (3). Implanted positrons thermalize before undergoing diffusion through the solid until they either annihilate in a delocalized state (4), become trapped in a defect (5) or diffuse to the surface where they can be emitted into the vacuum, if the material has a negative work function for positrons (6).

7.2 Silicon carbide

It has been long established that n-type silicon carbide is an efficient moderator material [122], although its low density ($3.211\,\mathrm{g\,cm^{-3}}$) makes it unsuitable to be used as a primary moderator. Silicon carbide is a wide-band-gap semiconductor (~ 3 eV) and has a negative positron work function, making it a promising positron secondary moderator (moderator employed after a first high density moderator such as tungsten, for example). That added to the high breakdown voltage ensures a good candidate for a field-assisted (FA) moderator [123]. In this type of moderator, the material is subjected to an electric field that provides an additional drift contribution to the implanted positrons, hence increasing the number of positrons reaching the surface, and so increasing the moderation efficiency. Added to these remarkable qualities, a SiC remoderator is easier to maintain than a neon moderator, as it does not require very low pressures, cryocooling and regular regeneration, nor annealing like tungsten. Unlike these two moderators, in which the moderation efficiency is gradually reduced, the efficiency of SiC is expected to be constant.

Previous work by Suzuki et al. [124] suggests that an epitaxially grown n-type 6H-SiC film (deposition of a crystalline overlay on a crystalline substrate) with a low carrier

density is a good candidate for a secondary moderator. Herein, a secondary moderator is referred to as a remoderator. Other studies [125, 126] on as grown SiC wafers have shown the potential of this material but revealed a lower remoderation efficiency in comparison to the epitaxially grown wafers. Positrons in epitaxial silicon carbide have a long lifetime, 182 ps for a 6H-SiC sample [127], when compared to the thermalization process that is in the order of a few picoseconds [128]. Due the reduced concentration of positron traps, the annihilation probability is smaller and the positrons have a long diffusion length. The average distance traveled by the positron during its lifetime is of the order of a few hundred nanometers [129]. The long diffusion length and the negative work function allow the positrons implanted deep in the material, to be emitted to the vacuum.

It has been shown that a p-type SiC layer has an apparent short diffusion length ($\sim$ 10-19 nm [124]), therefore it is not a good moderator candidate. Ling *et al.* [126] suggested that this might be due to an electric field generated by band bending, which may inhibit the positrons to reach the surface by pushing them into the sample.

The physical and chemical stability of SiC, however, has made crystal growth of SiC extremely difficult. Nonetheless, large (10 cm) good quality epitaxial wafers are readily available today with very low carrier concentration and defect density due to improvements in layer growth technology and defect control [130].

7.3 Experimental setup

The experiments described here were realized using the positron beam facility described in Chapter 3. A positron pulse stretcher transforms the 2.5 μs pulses generated by the LINAC into short positron pulses of $\sim$ 100 ns FWHM. The stretcher is composed of a low field Penning-Malmberg trap with three electrodes. The second electrode is 4 m long, in order to accommodate the entire slow positron pulse. The other two electrodes open and close the trap, synchronized with the LINAC pulses.

Downstream of the 80 G beam line, the positron beam is accelerated into a 30 cm tube, kept at a negative bias V_{tube}, and subsequently hits a 4H-SiC epitaxial layer held at a bias V_{sample}. The experimental apparatus is immersed in a magnetic field of 80 G. The γ-ray photons that resulted from the annihilation of the positrons were detected using a plastic scintillator combined with a XP2020 photomultiplier. The signal acquisition was done by means of a National Instruments PXIe 5160 digitizer. Figure 7.2 shows a schematic diagram and a picture of the experimental setup.

The epitaxial layer was grown on a n-doped 4H-SiC (0001) substrate by chemical vapor deposition, and is nitrogen n-doped with a carrier density smaller than 10^{15} cm^{-3} and 5.5 μm thick, 16-28 mΩcm resistivity and 3.211 gcm^{-3} density. The wafer was purchased from Norstel [131]. The epitaxial layer was not subjected to any form of surface treatment, it was used as received.

All measurements reported in the next section were performed on the epitaxial layer and on the SiC substrate (backside of the 4H-SiC wafer) for comparison.

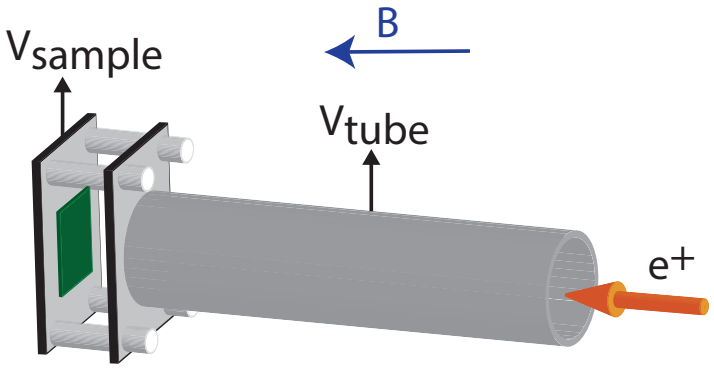

(a)

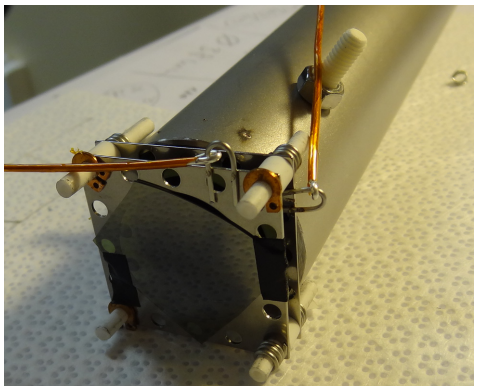

(b)

Figure 7.2: (a) Schematic diagram of the experimental setup. Positrons are accelerated onto the 4H-SiC target by applying the bias V_{sample} to a 30 cm long tube. (b) A picture of the experimental setup. One electrode was removed so that the 4H-SiC sample can be observed.

7.4 Results and discussion

A positron that is injected into a negative work function material with keV energy can reach thermal equilibrium and diffuse to the surface, where it is emitted with a minimum kinetic energy equal to the magnitude of the positron work function Φ^+ of the material [132]. Since 4H-SiC has a negative work function, $\Phi^+ \sim$-2 eV [125] [126], one expects that some of the incident positrons are re-emitted from the surface. These emerge from the sample surface with a longitudinal kinetic energy E_z (parallel to the magnetic field). They can only re-enter the tube if they overcome the potential difference between the tube and the sample, ΔV, plus the contact potential Φ_c - electrostatic potential that exists between samples of two dissimilar electrically conductive materials. The minimum energy the positrons require to overcome ΔV and Φ_c can be written as

$$E_{\text{pass}} = e\left(\Delta V + \Phi_c\right) . \tag{7.2}$$

Then if $E_z \geq E_{\text{pass}}$ the positrons can re-enter the tube but if $E_z \leq E_{\text{pass}}$ they return and

annihilate in the sample resulting in γ-rays detected by the scintillator. This means that if their energy is high enough to overcome ΔV, then they can execute several round trips between the sample and the end of the tube, while a fraction of positrons is annihilated at the target in each trip, until all positrons are annihilated. The result of this process can be observed in figure 7.3 for both the epitaxial layer and the substrate. In this measurement, V_{sample} was set to -2000 V and V_{tube} was varied. Figure 7.3 also shows that the time it takes the positrons to do a round trip increases with increasing ΔV, as well as the broadening of the time distribution.

Figure 7.4 shows the photomultiplier annihilation signal when positrons are implanted in the epitaxial layer and when the voltage difference between the tube and the sample (ΔV) is -11.6 V and 8.6 V. The positron re-emission yield is defined here as the fraction of the incident positron beam that was remoderated: Yield $= 1 - \frac{A_1}{A}$, where A_1 is the integrated area of the first positron annihilation peak when remoderation occurred; and A the integrated area of the total annihilation peak (i.e when ΔV = 8.6 V all positrons return to the surface and are annihilated).

7.4.1 Work function

In order to measure the work function, the sample potential was set to -2000 V, the tube voltage was varied from -1990.5 V to 2010.6 V and the re-emission yield was measured as a function of the voltage difference between the tube and the sample (ΔV). The result is plotted in figure 7.5a, together with the complementary error function fitted to the data points.

The positron work function Φ^+ can be derived by computing the difference between the bias for which all the remoderated positrons emerge from the sample and are not repelled by the tube (V_0, which implies $E_{\text{pass}} = 0$ in equation 7.4), and the bias corresponding to the point of steepest descent of figure 7.5a (peak of the re-emitted positron energy distribution figure 7.5b) E_{Peak} [132]:

$$\Phi^+ = e\,(V_0 - V_{\text{Peak}})\ . \tag{7.3}$$

V_0 was estimated by fitting a straight line through the data points in the initial constant region of the re-emission yield (figure 7.5a) and noting the ΔV above which the count rate starts to decrease by more than 1% [125]. This criteria yielded V_0 = -1.35 $\pm$ 0.01 V for the epitaxial layer and V_0 = -1.53 $\pm$ 0.01 V for the substrate.

The re-emitted positron energy distribution can then be determined from the fit and is plotted in figure 7.5b. V_{Peak} corresponds to the mean of the Gaussian curve and has the values $V_{\text{Peak}} = 0.78 \pm 0.03$ V for the epitaxial layer and $V_{\text{Peak}} = 1.12 \pm 0.06$ V for the substrate. Accordingly, the work function is Φ^+ = -2.13 $\pm$ 0.03 eV for the epitaxial layer and Φ^+ = -2.65 $\pm$ 0.06 eV for the substrate, in agreement with the results of [125] and [126].

7.4.2 Energy distribution

The energy spread of the re-emitted positrons is shown in figure 7.5b giving $\sigma = 0.91 \pm 0.04$ eV for the epitaxial layer and $\sigma = 1.1 \pm 0.1$ eV for the substrate.

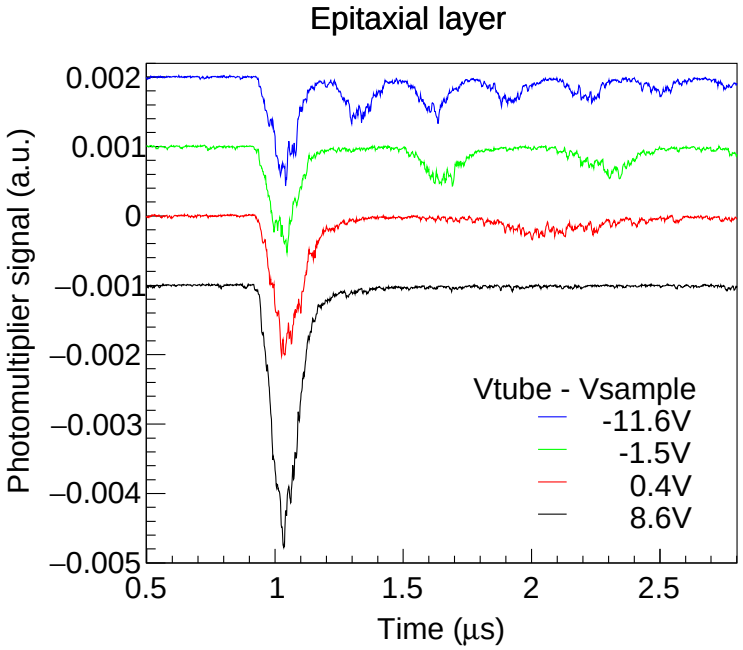

(a)

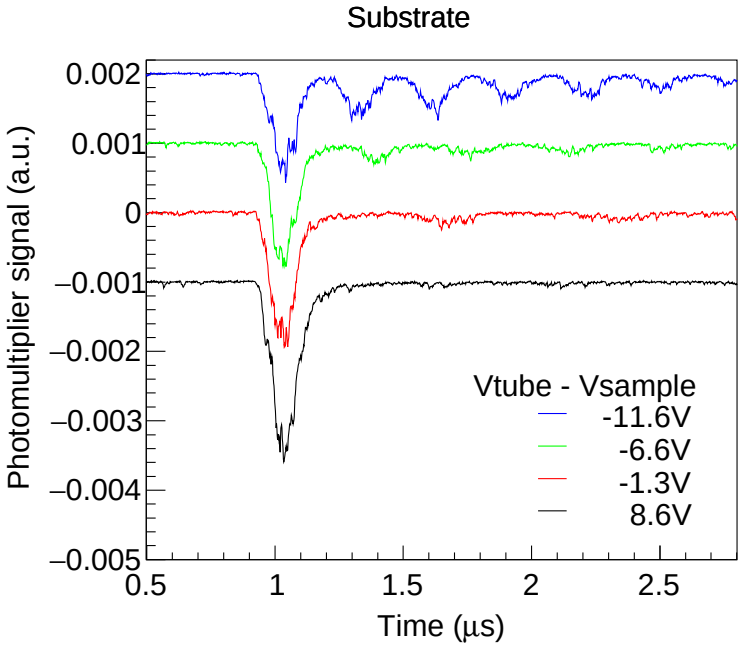

(b)

Figure 7.3: Signal obtained from the photomultiplier upon implanting positrons in the epitaxial layer (a), and substrate (b) for different voltages V_{tube}. The energy of the incident positrons is 2 keV. The curves were shifted vertically for clarity.

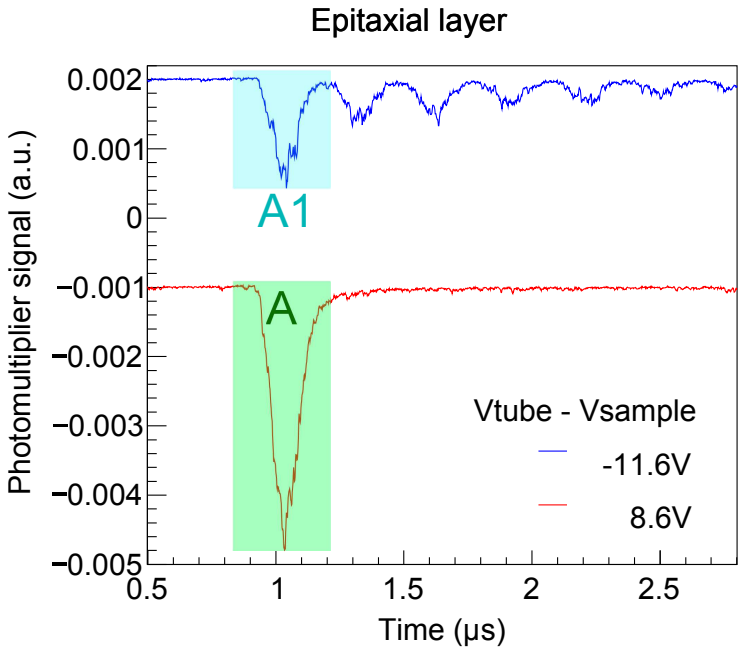

Figure 7.4: The positron re-emission yield is defined as the fraction of the incident positron beam that was remoderated. A_1 is the integrated area of the first positron annihilation peak, when remoderation occurred, and A the integrated area of the total annihilation peak.

The energy distributions of the re-emitted positrons also show that it drops more sharply for the epitaxial layer than for the substrate.

The contribution of the epithermal positrons was computed by integrating the spectra above the negative work function emission energy, figure 7.5b and dividing it by the total integral [133]. An epithermal fraction of 7.5% and 8.4% was obtained for the epitaxial layer and substrate, respectively, for a 2 keV positron beam. This result is considerably lower than the $\sim$20% fraction that Nangia *et al.* [125] reported for a non epitaxial 6H-SiC sample with a small diffusion length of 80 nm.

7.4.3 Positron re-emission yield and diffusion length

Figure 7.6 shows the positron re-emission yield as a function of the incoming beam energy for the epitaxial layer and substrate. The fraction of positrons that reach the surface, and are remitted rather than forming positronium or becoming trapped in a surface state, Y_0 is 69% for the epitaxial layer and 65% for the substrate. Moreover, figure 7.6 shows that there is a higher yield for a larger positron energy range for the epitaxial layer, which can be an advantage for large energy spread beams.

As previously mentioned, a low defect concentration, corresponding to a long positron lifetime, allows positrons to thermalize and eventually reach the solid surface were they can be emitted to the vacuum. The lifetime is related to the distance the positron can travel before being annihilated, this distance is called the diffusion length. The diffusion length, L_+, in a defect-free material is defined as a function of the positron lifetime, τ_b, and the diffusion constant, D_+:

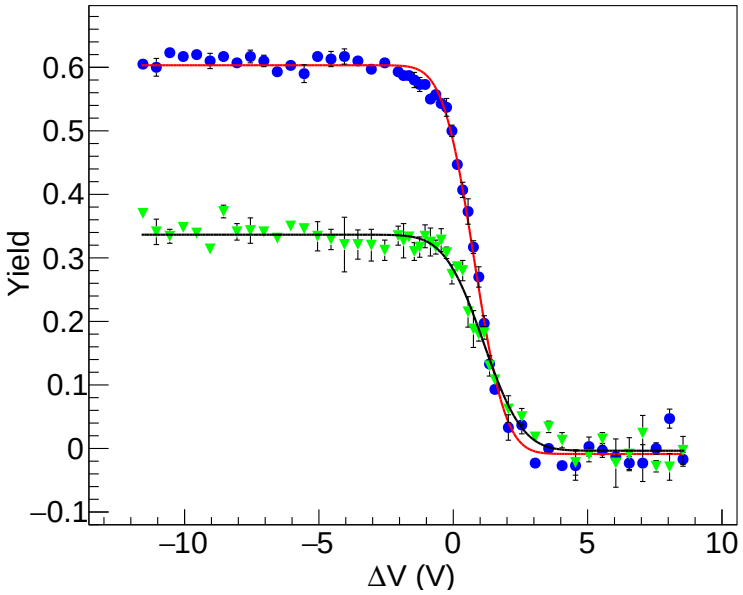

(a)

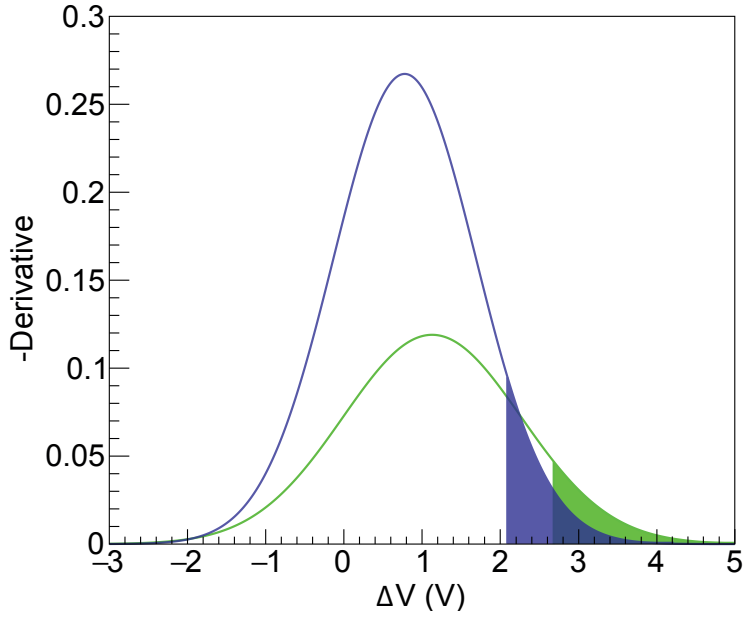

(b)

Figure 7.5: (a) Positron re-emission yield as a function of the voltage difference between the tube and the SiC sample (ΔV) for (•) the epitaxial layer and (▼) the substrate. The data points were fitted to an error function. (b) Energy distribution of the emitted positrons obtained from the fit shown in (a) for the epitaxial layer (—) and the substrate (—). The fraction of epithermal positrons of the epitaxial layer and substrate is represented by the shaded area corresponding to 7.5% and 8.4%, respectively.

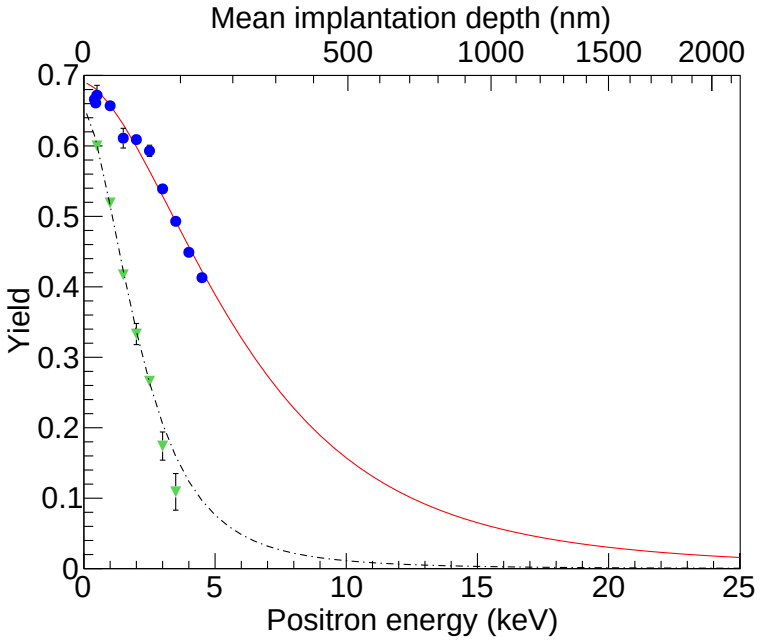

Figure 7.6: Positron re-emission yield as a function of the beam energy for the (•) epitaxial layer and (▼) substrate. The curves were fitted using VEPFIT [134] giving a diffusion length of $L_{\text{eff}} = 267 \pm 39$ nm for the epitaxial layer (—) and $L_{\text{eff}} = 51.4 \pm 0.8$ nm for the substrate (- · -).

$$L_+ = \sqrt{\tau_{\text{b}} D_+}\,. \tag{7.4}$$

To estimate the positron diffusion length in the epitaxial layer and in the substrate, the curves in figure 7.6 were fitted using the program VEPFIT [134]. This program calculates the implantation profile, $P(E_{e^+}, z)$, as a function of the penetration depth z and implanted positron energy. The stopping profile for positron thermalization in the range 1-50 keV incident energy was shown by Valkealahti *et al.* [135] to obey the implantation form originally suggested by Makhov for electrons [136]:

$$P(z) = \frac{m z^{m-1}}{z_0^m} \exp\left(-\left[\frac{z}{z_0}\right]^m\right), \tag{7.5}$$

where m is a dimensionless parameter (for the Gaussian implantation profile $m = 2$ [120]) and z_0 is related to the mean penetration depth $\bar{z}$ by

$$z_0 = \frac{\bar{z}}{\Gamma\left[(1/m) + 1\right]}, \tag{7.6}$$

where Γ is the gamma function. The mean penetration depth depends on the incident positron energy E as

$$\bar{z} = \frac{A}{\rho} E^r, \tag{7.7}$$

in which $\rho = 3.217\,\text{g/cm}^3$ is the density of the target, while $r = 1.6$ and $A = 4\,\mu\text{g/cm}^2\text{keV}^{-r}$ are values empirically found in reference [137].

For the epitaxial layer a diffusion length of $L_{eff} = 267 \pm 39\,nm$ was obtained and $L_{eff} = 51.4 \pm 0.8\,nm$ for the substrate. The smaller diffusion length of the substrate indicates a higher amount of defects that trap the positrons.

The presence of defects that may be formed during the growth of the sample, can affect the diffusion length by increasing the positron trapping rate, $\kappa(\mathbf{r})$, hence increasing the effective annihilation rate [138]

$$\lambda_{\text{eff}} = 1/\tau_{\text{b}} + \kappa(\boldsymbol{r}), \tag{7.8}$$

and consequently the effective positron diffusion constant via

$$D_{+}^{\text{eff}} = L_{+}^{2}\lambda_{\text{eff}}\,. \tag{7.9}$$

Electric fields can also influence the effective diffusion length L_{eff}, either by increasing it or decreasing it depending on their direction. The effective diffusion length is then given by

$$L_{\text{eff}} = \frac{1}{\sqrt{\frac{\lambda_{\text{eff}}}{D_{+}} + \left(\frac{eE_{\text{drift}}}{2k_{\text{B}}T}\right)^{2}} - \frac{e|E_{\text{drift}}|}{2k_{\text{B}}T}}\,, \tag{7.10}$$

where E_{drift} is the electric field strength. Since the effective diffusion length is dependent on the electric field, it is possible that the obtained diffusion length is over or underestimated as electric fields were not taken into account. In the case of this low-doped epitaxial layer the conductance is very small, thus an electric field is probably present. The diffusion length is, therefore, not a very reliable parameter in semiconductors, however it is still useful to compare with other measurements.

7.4.4 Doppler broadening spectroscopy

To further characterize the sample and investigate its diffusion length, the silicon carbide wafer was studied using a Doppler Broadening Spectrometer (DBS), at the slow positron beam facility at CEMHTI of the CNRS of Orléans. The DBS technique consists of implanting positrons in a solid, and measuring the annihilation spectrum using, in this case, a solid-state (liquid nitrogen cooled germanium) detector with a high energy resolution (<1.3 keV at 511 keV). It takes advantage of the fact that the momentum of a thermalized positron is significantly smaller than that of most of the electrons in a solid, and that the energy and momentum is conserved in the annihilation of a positron with an electron. From this, the defect distribution in a material can be estimated as the core electrons have a higher momentum than the valence electrons.

The implanted positron annihilates with an electron into two γ-rays with 511 keV energy, which are emitted in opposite directions. The momentum component p_z in the photon's propagation direction, z, leads to a Doppler shift, ΔE, of the annihilation energy approximately equal to [138]

$$\Delta E = p_z c/2\,. \tag{7.11}$$

If a positron annihilates with a valence electron, which has a low momentum, then the momentum of the pair e^{+}-e^{-} is small and the shift, $\pm\Delta E$, of the annihilation γ-ray is

also small. In that way, the γ-ray has an energy close to 511 keV and will contribute to the center of the Doppler spectrum. On the other hand, if a positron annihilates with a core electron, which has a larger momentum, then the Doppler shift, $\pm\Delta E$, will be larger and will contribute to the tail of the spectrum, broadening the Doppler spectrum.

Two parameters are commonly used to characterize the profile: the S ("Shape") parameter is defined as the area of the central low-momentum part of the spectrum, divided by the area below the whole curve after background subtraction; and the W ("Wing") parameter corresponds to the high-momentum region of the curve's tail which originates from large energy deviations due to the core electrons. A positron is repelled by the atomic nuclei, therefore it annihilates predominantly with valence electrons contributing to the center of the Doppler profile. For the same reason an open volume defect, e.g. a missing atom, can trap a positron. In this region of lower core electron density, positrons annihilate more often with valence electrons resulting in a sharpening of the Doppler curve and an increase of the S parameter [117]. The typical spectrum of a defect free material and a material containing open volume defects can be observed in figure 7.7.

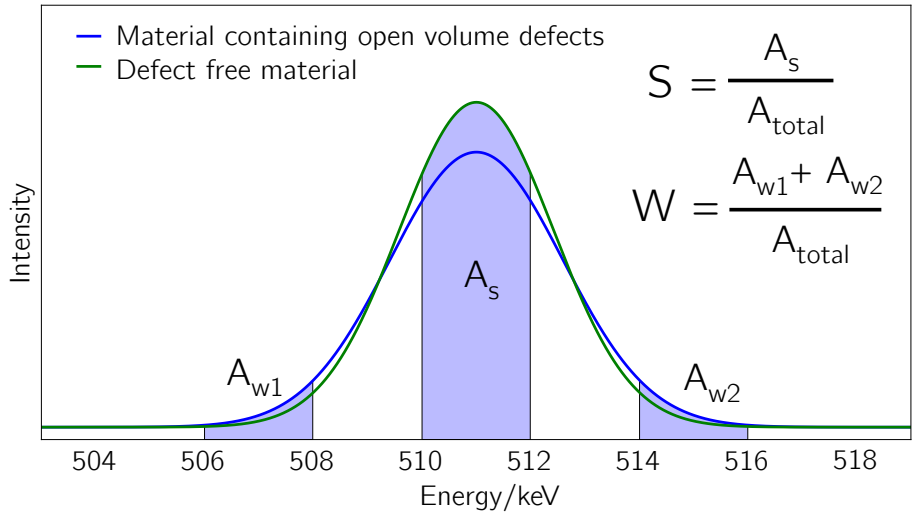

Figure 7.7: Typical spectrum of a defect free material (—) and a material containing open volume defects (—). Two parameters are useful to characterize the spectrum profile: the S ("Shape") parameter is defined as the area of the central low-momentum part of the spectrum, divided by the area below the whole curve after background subtraction; and the W ("Wing") parameter corresponds to the high-momentum region of the curve's tail.

Figure 7.8 and 7.9 show the results of this technique applied to the SiC wafer. The S and W parameters of the epitaxial layer in figures 7.8a and 7.8b, as well as the S-W map in figure 7.9, suggest two different behaviors before and after approximately 2.4 keV positron energy, corresponding to $\sim$50 nm mean implantation depth. To account for that, the data was fitted using the VEPFIT program assuming two different layers with the same density but different diffusion lengths. For the first layer, with 50 nm

thickness, the measured diffusion length is short $L_{eff} = 6.6 \pm 0.3$ nm, while for the second layer the diffusion length is much longer $L_{eff} = 250 \pm 10$ nm, as is expected. The substrate diffusion length is $L_{eff} = 38.0 \pm 0.5$ nm. The epitaxial layer values are consistent with the ones computed previously in this chapter, yet the same cannot be said for the substrate diffusion length. However, one can notice in figure 7.6 that the substrate fit overestimates the diffusion length. Anwand *et al.* [129] reported a diffusion length of $L_+ = 321 \pm 15$ nm for a 6H-SiC epitaxial layer, and $L_+ = 58 \pm 3$ nm for a crystalline 6H-SiC, while Suzuki *et al.* reported $L_+ = 276 \pm 7$ nm for a n-doped 6H-SiC epitaxial layer.

Figure 7.9 shows the S-W map of the epitaxial layer and substrate. For the first case, three annihilations states are observed: surface state, an interface and the bulk. The substrate map shows one surface state and the sample bulk. One can notice that the annihilation characteristics are different for the epitaxy and substrate, and in particular the bulk of the epitaxial layer does not correspond to the bulk of the substrate. The behavior of the S-W map is similar to the one observed on a 6H-SiC epitaxy by Linez *et al.* [139], below the ~ 50 nm layer. Surprisingly, it seems that the 4H-SiC epitaxy contains a larger number of open volume defects than the substrate (larger S parameter).

In the case of the substrate, from 5 keV henceforth the S and W parameters are constant, hence at this point the positron diffusion is negligible and S and W correspond to the crystalline lattice.

The epitaxial layer shows a higher S parameter than the substrate layer. During the chemical vapor deposition of the epitaxial layer, the growth rate is of the order of several μm/hour. According to the producer of the wafer, when the growth is completed the process of stopping the deposition lasts a few seconds. During this period the stoichiometric ratio is perturbed, introducing defects in the grown layer. Temperature and pressure variations can also contribute to the alteration of the properties of the deposited material. Given this, it is possible that a layer with altered properties was grown on top of the epitaxial layer. This layer can, in principle, correspond to the observed 50 nm layer with a saturated vacancy signal.

Further studies can be performed on the sample to characterize the defect structure of the epitaxial layer, however such efforts are beyond the scope of this thesis.

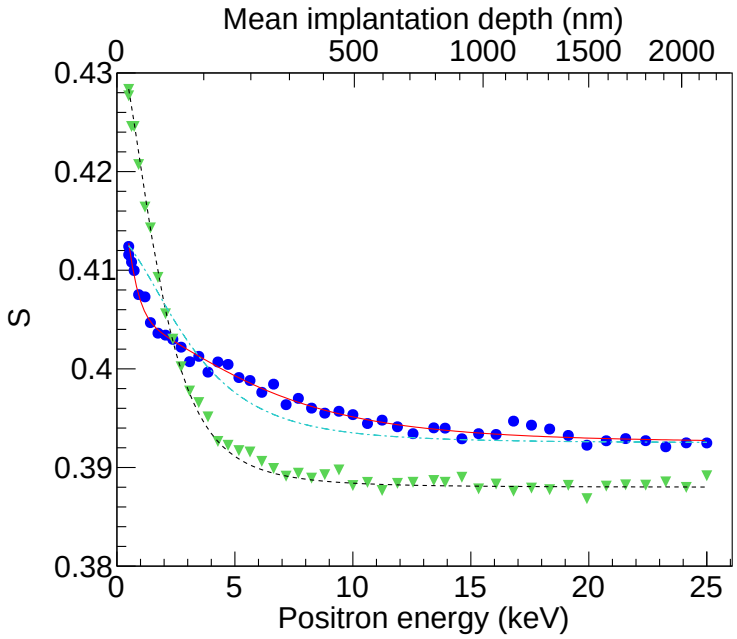

(a)

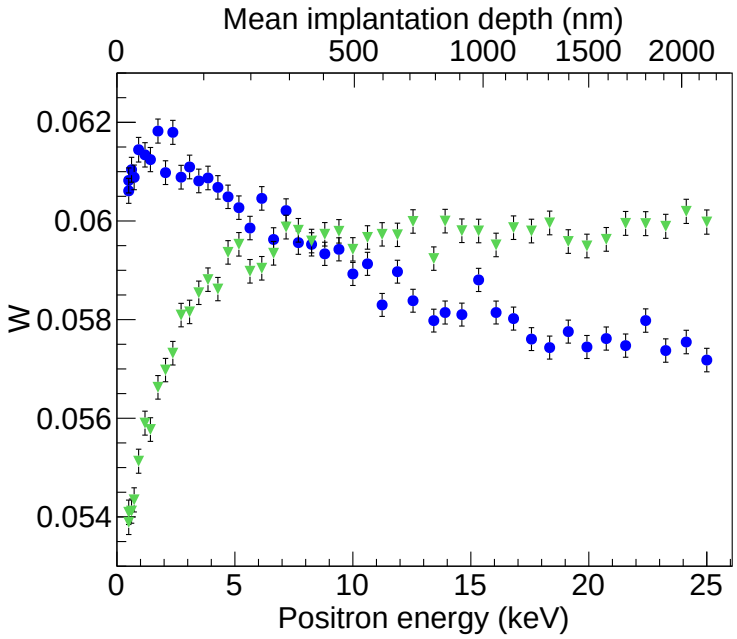

(b)

Figure 7.8: (a) S parameter as a function of the beam energy for the (●) epitaxial layer and the (▼) substrate. The curves were fitted using VEPFIT [134] resulting in a diffusion length of $L_{\text{eff}} = 6.6 \pm 0.3\,\text{nm}$ for the first epitaxial layer, while for the second layer the diffusion length is $L_{\text{eff}} = 250 \pm 10\,\text{nm}$ (—). The substrate diffusion length is $L_{\text{eff}} = 38.0 \pm 0.5\,\text{nm}$ (- -). A curve (- · -) corresponding to a fit of the epitaxial data points but assuming only one layer is present. (b) W parameter as a function of the beam energy for the (▼) epitaxial layer and (▼) substrate.

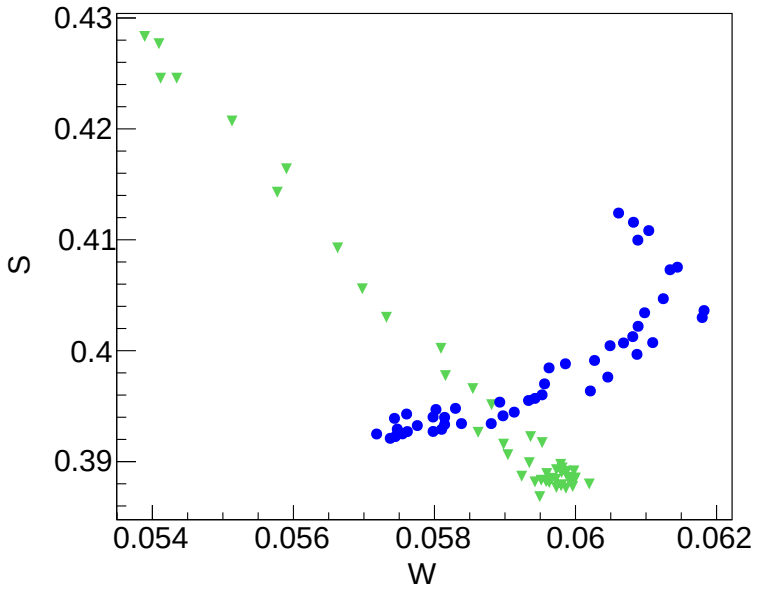

Figure 7.9: S-W map of the (●) epitaxial layer and (▼) substrate.

7.5 Applications of a 4H-SiC remoderator

Although the kinetic energy distribution of the remoderated positrons is significantly broader than that of the best single crystal metal moderators, high efficiency and easy handling makes SiC an attractive alternative in many cases where significant improvement is needed in brightness, but narrow energy distribution is not essential. Such cases are when brightness enhancement is required after a positron buncher with large amplitude or positron ejection from an accumulator with a deep potential well.

Given the present technology, an epitaxial SiC remoderator can only function in a reflection geometry. However, one could envision an electromagnetic transport system that guides the incoming positrons to the remoderator surface, and redirects the remoderated positrons around the remoderator, to deliver them to the next apparatus along the same axis. Such a system could be composed of an electrostatic mirror (electrode biased well above the remoderator potential) that reflects the remoderated positrons, and two sets of E×B plates (charged particle deflectors that work in magnetic transport) that guide the beam around the remoderator holder.

Oshima et al. [140] have proposed a conceptual scheme of positron cooling and accumulation in a 5 T Penning-Malmberg trap, using a combination of a high density electron plasma and an ion cloud. In their apparatus a tungsten single crystal is positioned inside the trap to remoderate the positrons produced by a ^{22}Na source [141]. Afterwards, the remoderated positrons interact with the preloaded electron plasma and through Coulomb interaction lose their energy and become trapped. The remoderator consists of a tungsten W(100) disc with 9 mm diameter and 0.5 mm thickness, and is fixed to a rotating support between the electrodes. Figure 7.10 shows two pictures of the trap electrode system with the moderator support. Before the ejection of the positrons out of the trap, the support is rotated and a 15 mm hole allows the passage

of the positrons.

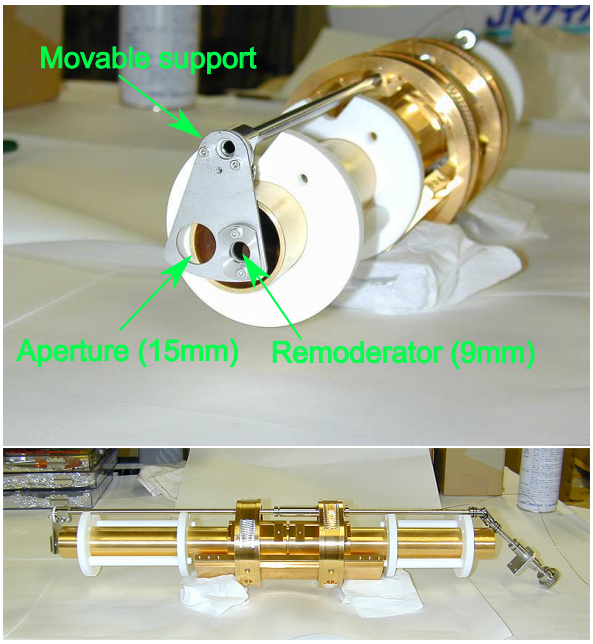

Figure 7.10: One stack of electrodes of the 5 T Penning-Malmberg is shown. The remoderator support is located between two stacks of electrodes and allows the insertion of a remoderator with 9 mm diameter. In order to eject the positrons out of the trap, the support can be moved so that the positrons can pass through a 15 mm aperture.

Since the 4H-SiC epitaxy does not require any maintenance in comparison to tungsten and is much more efficient in the 0-10 keV range, one could use a n-doped 4H-SiC epitaxial wafer in the place of tungsten. Further studies of this accumulation technique with SiC would be very interesting in order to validate its feasibility. If proven successful, it could be extremely useful to the positron trapping community for its technical simplicity. One should also evaluate the remoderation efficiency of the 4H-SiC epitaxial layer in cryogenic conditions, as it is the case of many trap systems.

7.6 Conclusion

In this chapter a commercially available n-type 4H-SiC epitaxial layer was studied with the prospect of using it as an efficient positron remoderator. A remoderation efficiency higher than 65% was obtained for 1 keV implanted positrons. The measured work function $\Phi^+ = -2.13 \pm 0.03$ eV is in good agreement with the one found in references [125, 126]. The positrons are re-emitted from the epitaxial layer with an energy spread of 0.91 ± 0.04 eV (σ). Two independent measurements showed a long diffusion length of ~ 250 nm for the epitaxial layer in agreement with measurements done by other groups.

The results reported in this chapter indicate that the epitaxially grown layer is a superior secondary moderator than its substrate counterpart. Being easily available and requiring minimal maintenance makes the epitaxial 4H-SiC an attractive solution for

positron moderation, facilitating the construction of laboratory-based positron beams with higher beam intensity and brightness.

Two applications of the SiC remoderator were discussed. The first includes an electromagnetic transport system that conserves the direction of propagation of the positron beam. This apparatus has been assembled and could, in principle, be tested in the positron beam line at Saclay. The second application could easily be tested since the 5 T Penning-Malmberg trap is currently being used by the GBAR collaboration.

Part V

Conclusion

Conclusion

"No book can ever be finished. While working on it we learn just enough to find it immature the moment we turn away from it."
Karl Popper

Summary

The GBAR experiment relies on the production of antihydrogen positive ions to achieve its goal of measuring the gravitational acceleration of antimatter at rest. The ANTION project, included in the GBAR enterprise, is responsible for the production of these antimatter ions. Moreover, it also aims to measure the cross section of antihydrogen production throughout the collision of antiprotons and positronium atoms, as well as the matter cross sections of hydrogen and the hydrogen negative ion. These experiments imply the formation of a very dense positronium cloud, thus a large amount of positrons will be implanted on a positron/positronium converter material.

This thesis reported the construction of a three stage buffer gas trap with the goal of trapping and accumulating positrons for the ANTION project. The combination of the Penning-type trap with a LINAC source constitutes an unique experimental setup. The trap was commissioned and optimized, and is now fully operational. Trapping protocols were studied and the effect of the buffer and cooling gases on the positron trapping rate and lifetime was assessed. The rotating wall technique was successfully applied in three distinct wells to mitigate the radial transport of the positrons due to the presence of gas, and also to compress the positron clouds. The frequency scan of the rotating wall in the second well of the third stage revealed a hint of a transitory regime between the single particle and the plasma regime. Further study should be undertaken to fully understand the observed behavior.

A GEANT4 simulation was developed to evaluate the time and spatial evolution of the ortho-positronium atoms in the reaction cavity, where the $p+Ps \rightarrow H+e^+$ reaction will take place. The simulations had the purpose of estimating the positronium density in the cavity, as well as the background associated with the positron and para-positronium decay, in order to assist with the cross section measurement of hydrogen.

Using the theoretically computed cross sections for the hydrogen production as a function of the proton impact energy, it was possible to estimate the number of hydrogen atoms produced for a pulse with 10^8 positrons and a microamp proton beam. For the experiments to be realized at Saclay, it was estimated that 2.7 hydrogen atoms

are produced for proton impact energy of $\sim 6\,\mathrm{keV}$, according to the Coulomb-Born Approximation model, and 1.6 hydrogen atoms for a proton impact energy of $\sim 10\,\mathrm{keV}$, according to the two-center convergent close-coupling method.

It was demonstrated that the angular distribution of the ortho-positronium, an unknown parameter, has a strong influence on the fraction of ortho-positronium that is able to escape the cavity, leading to an effective density loss. Furthermore, the simulations suggest that the production of ortho-positronium can be significantly improved if the top and bottom walls of the cavity are coated with mesoporous silica. This result is interesting for the experiments to be performed at Saclay, without the laser excitation of ortho-positronium.

In parallel to the work with the trap and the simulation, the positron moderation efficiency of a commercially available 4H-SiC epitaxial layer was studied. A 65% moderation efficiency was observed for 1 keV implanted positrons. This result can be of interest to slow positron physics experiments by improving the brightness of positron beams, and in particular to GBAR because it can help the increase of the number of trapped positrons in an accumulator.

Outlook

Both the buffer gas trap and the ANTION apparatus will move to CERN to be integrated with the GBAR experimental setup. In what concerns the trap, this will imply a re-optimization of the potentials of the electrodes, since a different positron energy distribution is expected given that the beam line is different. Further work is still required to improve the slow control and data acquisition systems, in order to achieve a higher degree of remote operation, necessary to perform experiments in the Antiproton Decelerator hall. Moreover, there is still a fair amount of optimization work to significantly increase the trapping efficiency, namely the tuning of the buffer and cooling gas pressures. More importantly, effort should be made to discover the cause of the limited lifetime of the third stage, which is hampering the accumulation of a larger quantity of positrons.

The developed simulation requires the determination of many experimental parameters to reduce the parameter space and render it more realistic. Some of these parameters include the positron and proton beam time and spatial distributions, that should be soon made available. In addition, the collaboration would benefit if the simulation could be made more complete by integrating the positronium excitation, as well was the (anti)hydrogen and anti-ions production according to the respective cross sections.

At CERN, it would be worthwhile to the GBAR experiment, and to the positron physics community, to insert the silicon carbide wafer in the remoderator holder of the 5 T Penning-Malmberg trap, in order to assess the feasibility of this remoderation technique. However, the positron beam would have to be bunched, so that the full beam is able to fit inside the trap.

Bibliography

[1] Dirac P. A. M. *The Quantum Theory of the Electron* Proceedings of the Royal Society of London A: Mathematical, Physical and Engineering Sciences **117** 610–624 (1928).

[2] Dirac P. A. M. *The Quantum Theory of the Electron. Part II* Proceedings of the Royal Society of London A: Mathematical, Physical and Engineering Sciences **118** 351–361 (1928).

[3] Dirac P. A. M. *Quantised Singularities in the Electromagnetic Field* Proceedings of the Royal Society of London A: Mathematical, Physical and Engineering Sciences **133** 60–72 (1931).

[4] Anderson C. D. *The Apparent Existence of Easily Deflectable Positives* Science **76** 238–239 (1932).

[5] Anderson C. D. *The Positive Electron* Physical Review **43** 491–494 (1933).

[6] Chamberlain O., Segrè E., Wiegand C. and Ypsilantis T. *Observation of Antiprotons* Physical Review **100** 947–950 (1955).

[7] Baur G. *et al. Production of antihydrogen* Physics Letters B **368** 251–258 (1996).

[8] Kostelecký V. A. and Vargas A. J. *Lorentz and C P T tests with hydrogen, antihydrogen, and related systems* Physical Review D **92** 056002 (2015).

[9] Maury S. *The Antiproton Decelerator: AD* Hyperfine Interactions **109** 43–52 (1997).

[10] Gabrielse G., Roach T. and Estrada J. K. (ATRAP Collaboration) *Proposal presented to the SPSLC: The production and study of cold antihydrogen* Tech. Rep. CERN-SPSC-97-8. SPSC-P-306 CERN Geneva (1997).

[11] Azuma T., Bakos J. S. and Bluhme H. (ASACUSA Collaboration) *Atomic spectroscopy and collisions using slow antiprotons* Tech. Rep. CERN-SPSC-97-19. SPSC-P-307 CERN Geneva (1997).

[12] Hangst J. S. and Bowe P. *The ALPHA Collaboration Antihydrogen Laser PHysics Apparatus* Tech. Rep. SPSC-I-228. CERN-SPSC-2004-026 CERN Geneva (2004).

[13] Ulmer S., Yamazaki Y., Blaum K., Quint W. and Walz J. *Direct High-Precision Measurement of the g-Factor of a Single Antiproton Stored in a Cryogenic Penning Trap* Tech. Rep. CERN-SPSC-2012-019. SPSC-I-241 CERN Geneva (2012).

[14] Drobychev G. Y. *et al. Proposal for the AEGIS experiment at the CERN antiproton decelerator (Antimatter Experiment: Gravity, Interferometry, Spectroscopy)* Tech. Rep. SPSC-P-334. CERN-SPSC-2007-017 CERN Geneva (2007).

[15] Chardin G. *et al.* (GBAR Collaboration) *Proposal to measure the Gravitational Behaviour of Antihydrogen at Rest* Tech. Rep. CERN-SPSC-2011-029. SPSC-P-342 CERN Geneva (2011).

[16] Amoretti M. *et al. Production and detection of cold antihydrogen atoms* Nature **419** 456–459 (2002).

[17] Gabrielse G., Bowden N. S., Oxley P., Speck A., Storry C. H., Tan J. N., Wessels M., Grzonka D., Oelert W., Schepers G., Sefzick T., Walz J., Pittner H., Hänsch T. W., Hessels E. A. and Hessels E. A. *Background-free observation of cold antihydrogen with field-ionization analysis of its states* Physical Review Letters **89** 213401 (2002).

[18] The ALPHA Collaboration *Confinement of antihydrogen for 1000 seconds* Nature Physics **7** 558–564 (2011).

[19] Ahmadi M. *et al. Observation of the 1S-2S transition in trapped antihydrogen* Nature **541** 506–510 (2017).

[20] Ulmer S., Smorra C., Mooser A., Franke K., Nagahama H., Schneider G., Higuchi T., Van Gorp S., Blaum K., Matsuda Y., Quint W., Walz J. and Yamazaki Y. *High-precision comparison of the antiproton-to-proton charge-to-mass ratio.* Nature **524** 196–9 (2015).

[21] Deutsch M. *Evidence for the formation of positronium in gases* Physical Review **82** 455–456 (1951).

[22] Nieto M. M. and Goldman T. *The arguments against "antigravity" and the gravitational acceleration of antimatter* Physics Reports **205** 221–281 (1991).

[23] Darling T. W., Rossi F., Opat G. I. and Moorhead G. F. *The fall of charged particles under gravity: A study of experimental problems* Reviews of Modern Physics **64** 237–257 (1992).

[24] Kramida A. *A critical compilation of experimental data on spectral lines and energy levels of hydrogen, deuterium, and tritium* Atomic Data and Nuclear Data Tables **96** 586–644 (2010).

[25] Cassidy D. B. and Hogan S. D. *Atom control and gravity measurements using Rydberg positronium* International Journal of Modern Physics: Conference Series **30** 1460259 (2014).

[26] Crivelli P., Cooke D. A. and Friedreich S. *Experimental considerations for testing antimatter antigravity using positronium 1S-2S spectroscopy* International Journal of Modern Physics: Conference Series **30** 1460257 (2014).

[27] Kaplan D. M., Fischbach E., Kirch K., Mancini D. C., Phillips J. D., Phillips T. J., Reasenberg R. D., Roberts T. J. and Terry J. *Antimatter gravity with muonium* (*Preprint* arXiv:1601.07222v2[physics.ins-det]) (2016).

[28] Phillips W. D., Rolston S. L., Lett P. D., McIlrath T., Vansteenkiste N. and Westbrook C. I. *Laser manipulation and cooling of (anti)hydrogen* Hyperfine Interactions **76** 265–272 (1993).

[29] Walz J. and Hänsch T. W. *A Proposal to Measure Antimatter Gravity Using Ultracold Antihydrogen Atoms* General Relativity and Gravitation **36** 561–570 (2004).

[30] Humberston J. W., Charlton M., Jacobson F. M. and Deutch B. I. *On antihydrogen formation in collisions of antiprotons with positronium* Journal of Physics B: Atomic and Molecular Physics **20** L25–L29 (1987).

[31] Mohamed T., Mohri A. and Yamazaki Y. *Comparison of non-neutral electron plasma confinement in harmonic and rectangular potentials in a very dense regime* Physics of Plasmas **20** 012502 (2013).

[32] Dupré P. *Piégeage de positons dans un piège de Penning Malmberg, en vue de leur accumulation avec un faisceau pulsé* Ph.D. thesis Université Pierre et Marie Curie - Paris 6 (2011).

[33] Grandemange P. *Piégeage et accumulation de positons issus d'un faisceau pulsé produit par un accélérateur pour l'étude de l'interaction gravitationnelle de l'antimatiére* Ph.D. thesis Université Paris-Sud (2002).

[34] *Extra Low ENergy Antiproton (ELENA) ring and its Transfer Lines - Design Report* Tech. rep. CERN (2014).

[35] Herfurth F., Dilling J., Kellerbauer A., Bollen G., Henry S., Kluge H.-J., Lamour E., Lunney D., Moore R., Scheidenberger C., Schwarz S., Sikler G. and Szerypo J. *A linear radiofrequency ion trap for accumulation, bunching, and emittance improvement of radioactive ion beams* Nuclear Instruments and Methods in Physics Research Section A: Accelerators, Spectrometers, Detectors and Associated Equipment **469** 254–275 (2001).

[36] Comini P. *Study of the antihydrogen atom and ion formation in the collisions antiproton-positronium* Ph.D. thesis Univeristé Pierre et Marie Curie (2014).

[37] Comini P. and Hervieux P.-A. $\bar{H}^+$ *ion production from collisions between antiprotons and excited positronium: cross sections calculations in the framework of the GBAR experiment* New Journal of Physics **15** 095022 (2013).

[38] Kadyrov A., Rawlins C., Stelbovics A., Bray I. and Charlton M. *Antihydrogen Formation via Antiproton Scattering with Excited Positronium* Physical Review Letters **114** 183201 (2015).

[39] Rawlins C. M., Kadyrov A. S., Stelbovics A. T., Bray I. and Charlton M. *Calculation of antihydrogen formation via antiproton scattering with excited positronium* Physical Review A **93** 012709 (2016).

[40] Merrison J. P., Bluhme H., Chevallier J., Deutch B. I., Hvelplund P., Jørgensen L. V., Knudsen H., Poulsen M. R. and Charlton M. *Hydrogen Formation by Proton Impact on Positronium* Physics Review Letters **78** 2728–2731 (1997).

[41] Agostinelli S. *et al. Geant4 a simulation toolkit* Nuclear Instruments and Methods in Physics Research Section A: Accelerators, Spectrometers, Detectors and Associated Equipment **506** 250–303 (2003).

[42] Procureur S., Dupré R. and Aune S. *Genetic multiplexing and first results with a 50×50cm^2 Micromegas* Nuclear Instruments and Methods in Physics Research Section A: Accelerators, Spectrometers, Detectors and Associated Equipment **729** 888–894 (2013).

[43] Charlton M., Kadyrov A. S. and Bray I. *Heating due to momentum transfer in low-energy positronium-antiproton scattering* Physical Review A **94** 032701 (2016).

[44] Monroe C., Meekhof D. M., King B. E., Jefferts S. R., Itano W. M., Wineland D. J. and Gould P. *Resolved-Sideband Raman Cooling of a Bound Atom to the 3D Zero-Point Energy* Physical Review Letters **75** 4011–4014 (1995).

[45] Hilico L., Karr J.-P., Douillet A., Indelicato P., Wolf S. and Schmidt Kaler F. *Preparing single ultra-cold antihydrogen atoms for free-fall in GBAR* International Journal of Modern Physics: Conference Series **30** 1460269 (2013).

[46] Fitzakerley D. W., George M. C., Hessels E. A., Skinner T. D. G., Storry C. H., Weel M., Gabrielse G., Hamley C. D., Jones N., Marable K., Tardiff E., Grzonka D., Oelert W. and Zielinski M. *Electron-cooled accumulation of 4×10^9 positrons for production and storage of antihydrogen atoms* Journal of Physics B: Atomic, Molecular and Optical Physics **49** 064001 (2016).

[47] Sillitoe N., Karr J.-P., Heinrich J., Louvradoux T., Douillet A. and Hilico L. $\bar{H}^+$ *Sympathetic Cooling Simulations with a Variable Time Step* (*Preprint* `arXiv:1705.03347v2[physics.comp-ph]`) (2017).

[48] The ALPHA Collaboration and Charman A. E. *Description and first application of a new technique to measure the gravitational mass of antihydrogen.* Nature communications **4** (2013).

[49] Hangst J. S. *Addendum to the ALPHA Proposal; The ALPHA-g Apparatus* Tech. Rep. CERN-SPSC-2016-031. SPSC-P-325-ADD-1 CERN (2016).

[50] Andresen G. B. *et al. Trapped antihydrogen* Nature 4011–4014 (2010).

[51] Capra A., Amaudruz P.-A., Bishop D., Fujiwara M. C., Freeman S., Gill D., Grant M., Henderson R., Kurchaninov L., Lu P., Menary S., Olchanski K. and Retiere F. *Design of a Radial TPC for Antihydrogen Gravity Measurement with ALPHA-g* (*Preprint* arXiv:1609.06656v1[physics.ins-det]) (2016).

[52] Kellerbauer A. *et al. Proposed antimatter gravity measurement with an antihydrogen beam* Nuclear Instruments and Methods in Physics Research Section B: Beam Interactions with Materials and Atoms **266** 351–356 (2008).

[53] Kimura M. *et al. Development of nuclear emulsions with 1μm spatial resolution for the AEgIS experiment* Nuclear Instruments and Methods in Physics Research Section A: Accelerators, Spectrometers, Detectors and Associated Equipment **732** 325–329 (2013).

[54] Brusa R. S. *et al. The AEgIS experiment at CERN: measuring antihydrogen free-fall in earth's gravitational field to test WEP with antimatter* Journal of Physics: Conference Series **791** 012014 (2017).

[55] Hugenschmidt C. *Positron sources and positron beams* In: Dupasquier A., Mills A. P. and Brusa R. S., *Proceedings of the International School of Physics "Enrico Fermi": Physics with many positrons* volume 174 pp. 399–417 IOS Press ISBN 978-1-60750-646-1 (2010).

[56] Rey J.-M., Coulloux G., Debu P., Dzitko H., Hardy P., Liszkay L., Lotrus P., Muranaka T., Noel C., Pérez P., Pierret O., Ruiz N. and Sacquin Y. *Status of the Linac based positron source at Saclay* Journal of Physics: Conference Series **443** 012077 (2013).

[57] Chen F. F. *Introduction to Plasma Physics and Controlled Fusion* 3rd edition (Springer International Publishing) ISBN 978-3-319-22308-7 (2016).

[58] Pedersen T. S. *The Guiding Center Approximation* In: Knoop M., Madsen N. and Thompson R. C., *Trapped Charged Particles* pp. 55–80 World Scientific Publishing Europe Ltd. ISBN 978-1-78634-011-5 (2016).

[59] Ruiz N. *Étude et réalisation d'un faisceau de positons lents* Ph.D. thesis Université Pierre et Marie Curie - Paris 6 (2011).

[60] Sueoka O., Makochekanwa C. and Miyamoto S. *Reemission intensity and energy spectrum measurements of slow positron beams for various moderators* Japanese Journal of Applied Physics, Part 1: Regular Papers and Short Notes and Review Papers **42** 5799–5806 (2003).

[61] Chen D. M., Lynn K. G., Pareja R. and Nielsen B. *Measurement of positron reemission from thin single-crystal W(100) films* Physical Review B **31** 4123–4130 (1985).

[62] Dehmelt H. *Radiofrequency Spectroscopy of Stored Ions I: Storage* Advances in Atomic and Molecular Physics **3** 53–72 (1968).

[63] Mukherjee M., Beck D., Blaum K., Bollen G., Dilling J., George S., Herfurth F., Herlert A., Kellerbauer A., Kluge H. J., Schwarz S., Schweikhard L. and Yazidjian C. *ISOLTRAP: An on-line Penning trap for mass spectrometry on short-lived nuclides* The European Physical Journal A **35** 1–29 (2008).

[64] Farnham D. L., Van Dyck R. S. and Schwinberg P. B. *Determination of the electron's atomic mass and the proton/electron mass ratio via penning trap mass spectroscopy* Physical Review Letters **75** 3598–3601 (1995).

[65] Hanneke D., Fogwell S. and Gabrielse G. *New Measurement of the Electron Magnetic Moment and the Fine Structure Constant* Physical Review Letters **100** 120801 (2008).

[66] Malmberg J. H. and Degrassie J. S. *Properties of Nonneutral Plasma* Physical Review Letters **35** 577–580 (1975).

[67] Gabrielse G., Haarsma L. and Rolston S. L. *Open-endcap Penning traps for high precision experiments* International Journal of Mass Spectrometry and Ion Processes **88** 319–332 (1989).

[68] Estrada J. K. *Cold Trapped Positrons and Progress to Cold Antihydrogen* Ph.D. thesis Massachusetts Institute of Technology (2002).

[69] Surko C. M., Leventhal M. and Passner A. *Positron Plasma in the Laboratory* Physical Review Letters **62** 901–904 (1989).

[70] Murphy T. J. and Surko C. M. *Positron trapping in an electrostatic well by inelastic collisions with nitrogen molecules* Physical Review A **46** 5696–5705 (1992).

[71] Greaves R. G. and Surko C. M. *Positron trapping and the creation of high-quality trap-based positron beams* Nuclear Instruments and Methods in Physics Research, Section B: Beam Interactions with Materials and Atoms **192** 90–96 (2002).

[72] Marler J. P. and Surko C. M. *Positron-impact ionization, positronium formation, and electronic excitation cross sections for diatomic molecules* Physical Review A **72** 062713 (2005).

[73] Surko C. M. *Accumulation, Storage and manipulation of large numbers of positrons in traps I. - The Basics* In: Dupasquier A., Mills A. P. and Brusa R. S., *Proceedings of the International School of Physics "Enrico Fermi": Physics with many positrons* pp. 511–543 IOS Press ISBN 978-1-60750-646-1 (2010).

[74] van der Werf D. P., Isaac C. A., Baker C. J., Mortensen T., Kerrigan S. J. and Charlton M. *The behaviour of positron clouds in the single-particle regime under the influence of rotating wall electric fields* New Journal of Physics **14** 075022 (2012).

[75] Gould R. W. *Wave Angular Momentum in Nonneutral Plasmas* AIP Conference Proceedings **498** 170–175 (1999).

[76] Danielson J. R. and Surko C. M. *Radial compression and torque-balanced steady states of single-component plasmas in Penning-Malmberg traps* Physics of Plasmas **13** 055706 (2006).

[77] Natisin M. R., Danielson J. R. and Surko C. M. *Positron cooling by vibrational and rotational excitation of molecular gases* Journal of Physics B: Atomic, Molecular and Optical Physics **47** 225209 (2014).

[78] Huang X.-P., Anderegg F., Hollmann E. M., Driscoll C. F. and O'Neil T. M. *Steady-State Confinement of Non-neutral Plasmas by Rotating Electric Fields* Physical Review Letters **78** 875–878 (1997).

[79] Anderegg F., Hollmann E. M. and Driscoll C. F. *Rotating Field Confinement of Pure Electron Plasmas Using Trivelpiece-Gould Modes* Physical Review Letters **81** 4875–4878 (1998).

[80] Greaves R. G. and Surko C. M. *Inward Transport and Compression of a Positron Plasma by a Rotating Electric Field* Physical Review Letters **85** 1883–1886 (2000).

[81] Prasad S. A. and O'Neil T. M. *Waves in a cold pure electron plasma of finite length* Physics of Fluids **26** 665–672 (1983).

[82] Danielson J. R. and Surko C. M. *Torque-Balanced High-Density Steady States of Single-Component Plasmas* Physical Review Letters **94** 035001 (2005).

[83] Cassidy D. B., Deng S. H. M., Greaves R. G. and Mills A. P. *Accumulator for the production of intense positron pulses* Review of Scientific Instruments **77** 073106 (2006).

[84] Greaves R. G. and Moxom J. M. *Compression of trapped positrons in a single particle regime by a rotating electric field* Physics of Plasmas **15** 072304 (2008).

[85] Isaac C. A., Baker C. J., Mortensen T., van der Werf D. P. and Charlton M. *Compression of Positron Clouds in the Independent Particle Regime* Physical Review Letters **107** 033201 (2011).

[86] Isaac C. A. *Motional sideband excitation using rotating electric fields* Physical Review A **87** 043415 (2013).

[87] Deller A. *Positron Accumulation and Laser Excitation of the Positronium Atom* Ph.D. thesis Swansea University (2013).

[88] Clarke J., van der Werf D. P., Griffiths B., Beddows D. C. S., Charlton M., Telle H. H. and Watkeys P. R. *Design and operation of a two-stage positron accumulator* Review of Scientific Instruments **77** 063302 (2006).

[89] Madsen N. *Trap configurations in ALPHA* unpublished (2012).

[90] Camp J. B., Darling T. W. and Brown R. E. *Macroscopic variations of surface potentials of conductors* Journal of Applied Physics **69** 7126–7129 (1991).

[91] Varian, Inc.Vacuum Technologies *Training Vacuum and Leak Detection.*

[92] Isaac A. C. *Axialisation of Particles in a Penning-type Trap by the Application of a Rotating Dipole Electric Field and its Application to Positron Accumulation* Ph.D. thesis Swansea University (2010).

[93] de Haas J. T. M. and Dorenbos P. *Advances in Yield Calibration of Scintillators* IEEE Transactions on Nuclear Science **55** 1086–1092 (2008).

[94] Ladislas Wiza J. *Microchannel plate detectors* Nuclear Instruments and Methods **162** 587–601 (1979).

[95] Natisin M. R., Danielson J. R. and Surko C. M. *Formation of buffer-gas-trap based positron beams* Physics of Plasmas **22** 033501 (2015).

[96] Deller A., Mortensen T., Isaac C. A., P van der Werf D. and Charlton M. *Radially selective inward transport of positrons in a Penning-Malmberg trap* New Journal of Physics **16** 073028 (2014).

[97] Dubin D. H. E. *Plasmas in Penning Traps* In: Knoop M., Madsen N. and Thompson R. C., *Trapped Charged Particles* World Scientific Publishing Europe Ltd. ISBN 978-1-78634-011-5 (2016).

[98] Natisin M. R. *Trap-based beam formation mechanisms and the development of an ultra-high-energy-resolution cryogenic positron beam* Ph.D. thesis University of California, San Diego (2016).

[99] Greaves R. G. and Surko C. M. *Radial compression and inward transport of positron plasmas using a rotating electric field* Physics of Plasmas **8** 1879–1885 (2001).

[100] Baker C. personal communication (2017).

[101] Paulin R. and Ambrosino G. *Annihilation libre de l'ortho-positonium formé dans certaines poudres de grande surface spécifique* Journal de Physique **29** 263–270 (1968).

[102] Mogensen O. E. *Spur reaction model of positronium formation* The Journal of Chemical Physics **60** 998–1004 (1974).

[103] Crivelli P., Gendotti U., Rubbia A., Liszkay L., Perez P. and Corbel C. *Measurement of the orthopositronium confinement energy in mesoporous thin films* Physical Review A **81** 052703 (2010).

[104] Mariazzi S., Salemi A. and Brusa R. S. *Positronium cooling into nanopores and nanochannels by phonon scattering* Physical Review B **78** 085428 (2008).

[105] Liszkay L., Corbel C., Perez P., Desgardin P., Barthe M. F., Ohdaira T., Suzuki R., Crivelli P., Gendotti U., Rubbia a., Etienne M. and Walcarius A. *Positronium reemission yield from mesostructured silica films* Applied Physics Letters **92** 1–4 (2008).

[106] Liszkay L., Barthe M.-F., Corbel C., Crivelli P., Desgardin P., Etienne M., Ohdaira T., Perez P., Suzuki R., Valtchev V. and Walcarius A. *Orthopositronium annihilation and emission in mesostructured thin silica and silicalite-1 films* Applied Surface Science **255** 187–190 (2008).

[107] Annenkov A., Korzhik M. and Lecoq P. *Lead tungstate scintillation material* Nuclear Instruments and Methods in Physics Research Section A: Accelerators, Spectrometers, Detectors and Associated Equipment **490** 30–50 (2002).

[108] Peko B. and Stephen T. *Absolute detection efficiencies of low energy H, H^-, H^+, H_2^+ and H_3^+ incident on a multichannel plate detector* Nuclear Instruments and Methods in Physics Research Section B: Beam Interactions with Materials and Atoms **171** 597–604 (2000).

[109] Salvat F., Fernandez-Varea J. M. and Sempau J. *Penelope-2006: A code system for Monte Carlo simulation of electron and photon transport - workshop proceedings, Barcelona, Spain, 4-7 July 2006* (Nuclear Energy Agency, Organisation for Economic Co-operation and Development) ISBN 9264023011 (2006).

[110] Crivelli P., Gendotti U., Rubbia a., Liszkay L. and Perez P. *Optimization of Positron Lifetime Spectrometer Using Monte-Carlo Simulation of the Detectors* Materials Science Forum **607** 251–253 (2009).

[111] Makinen J., Palko S., Martikainen J. and Hautojarvi P. *Positron backscattering probabilities from solid surfaces at 2-30 keV* Journal of Physics: Condensed Matter **4** L503–L508 (1992).

[112] Berestetskii V., Lifshitz E. and Pitaevskii L. *A Course of Theoretical Physics* volume 4 Relativistic Quantum Theory Part 1 (Pergamon Press) ISBN 9780080160252 (1971).

[113] O'Rourke B. E., Zhou W., Oshima N., Ito K. and Suzuki R. *Monte Carlo simulations of the extraction of slow positrons into gas through thin SiN windows* Journal of Physics: Conference Series **443** 012069 (2013).

[114] Cooke D. A., Crivelli P., Alnis J., Antognini A., Brown B., Friedreich S., Gabard A., Haensch T. W., Kirch K., Rubbia A. and Vrankovic V. *Observation of positronium annihilation in the 2S state: towards a new measurement of the 1S-2S transition frequency* (*Preprint* `arXiv:1503.05755v1[physics.atom-ph]`) (2015).

[115] Khaw K. S., Antognini A., Prokscha T., Kirch K., Liszkay L., Salman Z. and Crivelli P. *Spatial confinement of muonium atoms* Physical Review A **94** 022716 (2016).

[116] Comini P., Hervieux P.-A. and Biraben F. *$\bar{H}^+$ production from collisions between positronium and keV antiprotons for GBAR* Hyperfine Interactions **228** 159–165 (2014).

[117] Coleman P. *Positron Beams and Their Applications* (World Scientific Publishing Europe Ltd.) ISBN 978-981-02-3394-5 (2000).

[118] Dale J. M., Hulett L. D. and Pendyala S. *Low energy positrons from metal surfaces* Surface and Interface Analysis **2** 199–203 (1980).

[119] Wu Y. C., Chen Y. Q., Wu S. L., Chen Z. Q., Wang S. J. and Greaves R. G. *High moderation efficiency positron beamline* Physica Status Solidi (C) **4** 4032–4035 (2007).

[120] Schultz P. J. and Lynn K. G. *Interaction of positron beams with surfaces, thin films, and interfaces* Reviews of Modern Physics **60** 701–779 (1988).

[121] Fischer D. A., Lynn K. G. and Gidley D. W. *High-resolution angle-resolved positron reemission spectra from metal surfaces* Physical Review B **33** 4479 (1986).

[122] Stormer J., Goodyear A., Anwand W., Brauer G., Coleman P. G. and Triftshauser W. *Silicon carbide: a new positron moderator* Journal of Physics: Condensed Matter **8** L89–L94 (1996).

[123] Beling C. D., Simpson R. I., Charlton M., Jacobsen F. M., Griffith T. C., Moriarty P. and Fung S. *A field-assisted moderator for low-energy positron beams* Applied Physics A Solids and Surfaces **42** 111–116 (1987).

[124] Suzuki R., Ohdaira T., Uedono A., Cho Y. K., Yoshida S., Ishida Y., Ohshima T., Itoh H., Chiwaki M., Mikado T., Yamazaki T. and Tanigawa S. *Investigation of positron moderator materials for electron-linac-based slow positron beamlines* Japanese Journal of Applied Physics, Part 1: Regular Papers and Short Notes and Review Papers **37** 4636–4643 (1998).

[125] Nangia A., Kim J. H., Weiss A. H. and Brauer G. *Experimental determination of positron-related surface characteristics of 6H-SiC* Journal of Applied Physics **91** 2818–2826 (2002).

[126] Ling C. C., Weng H. M., Beling C. D. and Fung S. *Experimental investigation of slow-positron emission from 4H-SiC and 6H-SiC surfaces* Journal of Physics: Condensed Matter **14** 6373–6381 (2002).

[127] Britton D., Barthe M.-F., Corbel C., Desgardin P., Egger W., Sperr P., Kögel G. and Triftshäuser W. *Shallow traps and positron dynamics in epitaxial silicon carbide* Applied Surface Science **194** 122–126 (2002).

[128] Tuomisto F. and Makkonen I. *Defect identification in semiconductors with positron annihilation: Experiment and theory* Reviews of Modern Physics **85** 1583–1631 (2013).

[129] Anwand W., Brauer G., Wirth H., Skorupa W. and Coleman P. *The influence of substrate temperature on the evolution of ion implantation-induced defects in epitaxial 6H-SiC* Applied Surface Science **194** 127–130 (2002).

[130] Dhanaraj G., Raghothamachar B. and Dudley M. *Growth and Characterization of Silicon Carbide Crystals* In: Dhanaraj, G. and Byrappa, K. and Prasad, V. and Dudley, M., *Springer Handbook of Crystal Growth,* pp. 797–820 Springer-Verlag Berlin Heidelberg (2010).

[131] *Manufacturer of silicon carbide wafers, Norstel* http://www.norstel.com/

[132] Jibaly M., Weiss A., Koymen A. R., Mehl D., Stiborek L. and Lei C. *Measurement of the positron work functions of polycrystalline Fe, Mo, Ni, Pt, Ti, and V* Physical Review B **44** 12166 (1991).

[133] *Surface science with positrons* In: Coleman P., *Positron Beams and Their Applications* Chapter: 5, pp. 129–189 World Scientific Publishing Europe Ltd. ISBN 981-02-3394-9 (2000).

[134] Veen A. V., Schut H., Vries J. D., Hakvoort R. A. and Ijpma M. R. *Analysis of positron profiling data by means of "VEPFIT"* AIP Conference Proceedings **218** 171–199 (1991).

[135] Valkealahti S. and Nieminen R. M. *Monte Carlo Calculations of keV Electron and Positron Slowing Down in Solids. II* Applied Physics A Solids and Surfaces **35** 51–59 (1984).

[136] Makhov A. F. *The Penetration of Electrons Into Solids: I. The Intensity of an Electron Beam, Transverse Paths of Electrons* Soviet Physics-Solid State **2** 1934–1941 (1961).

[137] Vehanen A., Saarinen K., Hautojarvi P. and Huomo H. *Profiling multilayer structures with monoenergetic positrons* Physical Review B **35** 4606–4610 (1987).

[138] Krause-Rehberg R. and Leipner H. S. *Positron Annihilation in Semiconductors: Defect studies* (Springer-Verlag Berlin Heidelberg) ISBN 978-3-540-64371-5 (1999).

[139] Linez F., Gilabert E., Debelle A., Desgardin P. and Barthe M.-F. *Helium interaction with vacancy-type defects created in silicon carbide single crystal* Journal of Nuclear Materials **436** 150–157 (2013).

[140] Oshima N., Kojima T. M., Niigaki M., Mohri A., Komaki K. and Yamazaki Y. *New scheme for positron accumulation in ultrahigh vacuum* Physical Review Letters **93** 1–4 (2004).

[141] Oshima N., Kojima T. M., Niigaki M., Mohri A., Komaki K., Iwai Y. and Yamazaki Y. *Development of a cold HCI source for ultra-slow collisions* Nuclear Instruments and Methods in Physics Research, Section B: Beam Interactions with Materials and Atoms **205** 178–182 (2003).

université PARIS-SACLAY | ÉCOLE DOCTORALE PHENIICS

Titre: Développement d'une piège à "buffer gas" pour le confinement de positrons et l'étude de la production de positronium dans l'expérience GBAR

Mots clés: *Positons, piège à "buffer gas", Positronium, Hydrogène*

Résumé: L'expérience GBAR repose sur la production d'ions antihydrogène positifs dans le but de mesurer l'accélération gravitationnelle à laquelle est soumise l'antimatière au repos. Le projet ANTION, sous-projet de GBAR, a pour but la production de ces ions d'antimatière. Il vise également à mesurer la section efficace de production d'antihydrogène dans les collisions d'antiprotons sur des atomes de positronium, ainsi que les sections efficaces correspondantes avec la matière, de production d'hydrogène et de l'ion hydrogène négatif. Ces expériences reposent sur la formation d'un nuage très dense de positronium, et nécessitent donc une grande quantité de positons qui seront implantés sur un matériau convertisseur de positons en positronium.

Cette thèse décrit la construction d'un piège à "buffer gas" à trois étages, destiné à piéger et accumuler des positons pour le projet ANTION. L'association d'un piège de Penning avec une source basée sur un Linac constitue un montage expérimental unique. Le piège a été construit et optimisé, et est maintenant pleinement opérationnel. Les protocoles de piégeage ont été étudiés et les effets du gaz tampon et du gaz de refroidissement sur le taux de piégeage et la durée de vie des positons ont été quantifiés.

Afin de faciliter la mesure de la section efficace de production de l'hydrogène, une simulation avec GEANT4 a été mise au point. Elle décrit l'évolution temporelle et spatiale des atomes d'ortho-positronium dans la cavité où aura lieu la production d'hydrogène. On estime que 2.7 atomes d'hydrogène sont produits pour des proton de 6 keV d'énergie incidente, en utilisant les sections efficaces calculées avec le modèle "Coulomb-Born Approximation", et 1.6 atomes d'hydrogène pour des protons de 10 keV, si l'on utilise la méthode "two-center convergent close-coupling". Les simulations permettent également d'estimer le bruit de fond associé aux positons et à l'annihilation du para-positronium. Cette étude amène a proposer une modification permettant d'augmenter le nombre d'atomes de positronium dans la cavité.

En parallèle, une étude a porté sur l'efficacité de modération de positons d'une couche épitaxiale de carbure de silicium 4H-SiC. Une efficacité de modération de 65% a été mesurée pour des positons implantés avec une énergie de l'ordre du kiloélectronvolt. Ce résultat intéresse les expériences de physique utilisant des positons lents, car il permet d'améliorer la luminosité de faisceaux de positons; dans le cas de GBAR cela permettrait d'augmenter l'efficacité de piégeage des positons.

Université Paris-Saclay
Espace Technologique / Immeuble Discovery
Route de l'Orme aux Merisiers RD 128 / 91190 Saint-Aubin, France

université PARIS-SACLAY | ÉCOLE DOCTORALE PHENIICS

Title: Development of a buffer gas trap for the confinement of positrons and study of positronium production in the GBAR experiment

Key words: *Positrons, Buffer gas trap, Positronium, Hydrogen*

Abstract: The GBAR experiment relies on the production of antihydrogen positive ions to achieve its goal of measuring the gravitational acceleration of antimatter at rest. The ANTION project, included in the GBAR enterprise, is responsible for the production of these antimatter ions. Moreover, it also aims to measure the cross section of antihydrogen production throughout the collision of antiprotons and positronium atoms, as well as the matter cross sections of hydrogen and the hydrogen negative ion. These experiments imply the formation of a very dense positronium cloud, thus a large amount of positrons will be implanted on a positron/positronium converter material.

This thesis reports the construction of a three stage buffer gas trap with the goal of trapping and accumulating positrons for the ANTION project. The combination of the Penning-type trap with a LINAC source constitutes a unique experimental setup. The trap was commissioned and optimized and is now fully operational. Trapping protocols were studied and the effect of the buffer and cooling gases on the positron trapping rate and lifetime was assessed.

In order to assist the cross section measurement of hydrogen, a GEANT4 simulation was developed. It evaluates the time and spatial evolution of the ortho-positronium atoms in a cavity, where hydrogen production will take place. It was estimated that 2.7 hydrogen atoms are produced for proton impact energy of ~ 6 keV, according to the cross sections computed with the Coulomb-Born Approximation model, and 1.6 hydrogen atoms for a proton impact energy of ~ 10 keV, according to the two-center convergent close-coupling method. The simulations also allow the estimation of the background associated with the positron and para-positronium decay. In addition, a suggestion is proposed to increase the number of positronium atoms in the cavity.

In parallel, the positron moderation efficiency of a commercially available 4H-SiC epitaxial layer was studied. A 65% moderation efficiency was observed for kiloelectronvolt implanted positrons. This result can be of interest to slow positron physics experiments by improving the brightness of positron beams, and in particular to GBAR as it can potentially increase the efficiency of positron trapping.

Université Paris-Saclay
Espace Technologique / Immeuble Discovery
Route de l'Orme aux Merisiers RD 128 / 91190 Saint-Aubin, France